STUDY OF ALD FILMS FOR IMPROVING THE STABILITY AND RELIABILITY OF ELECTRONIC DEVICES IN HARSH ENVIRONMENTS

A Dissertation
Presented to
The Academic Faculty

by

Ankit Kumar Singh

In Partial Fulfillment
of the Requirements for the Degree
Doctor of Philosophy in the
Department of Materials Science & Engineering

Georgia Institute of Technology
May 2018

STUDY OF ALD FILMS FOR IMPROVING THE STABILITY AND RELIABILITY OF ELECTRONIC DEVICES IN HARSH ENVIRONMENTS

Approved by:

Dr. Samuel Graham, Advisor
School of Mechanical Engineering/
School of Materials Science &
Engineering
Georgia Institute of Technology

Dr. Preet M. Singh
School of Materials Science &
Engineering
Georgia Institute of Technology

Dr. Mark Losego
School of Materials Science &
Engineering
Georgia Institute of Technology

Dr. Elsa Reichmanis
School of Chemical & Biomolecular
Engineering
Georgia Institute of Technology

Dr. Maysam Ghovanloo
School of Electrical and Computer
Engineering
Georgia Institute of Technology

Date Approved: March 19, 2018

To my Parents

ACKNOWLEDGEMENTS

I would like to express my gratitude to my supervisor Prof. Samuel Graham for his suggestions and support throughout this research. His experience, critical thinking and suggestions helped me significantly throughout my research and were essential for the completion of this thesis in a timely and very successful manner.

I would like to thank my committee members, Prof. Preet M. Singh, Prof. Mark Losego, Prof. Elsa Reichmanis and Prof. Maysam Ghovanloo for their advice and evaluation of this work. I would like to thank my group members for their help and support on numerous occasions during my studies: Kyungjin Kim, Dr. Minseok Ha, Dr. Darshan Pahinkar, Georges Pavlidis, Luke Yates, Samuel Kim, Waylon Puckett, Dr. Hyungchul Kim, Dr. Anuradha Bulusu, Katarina Adstedt and Kartavya Agarwal.

I would like to give special thanks to Prof. Preet M. Singh for providing the facilities for conducting EIS experiments and also for having fruitful discussions. I would like to express my gratitude to Prof. Bernard Kippelen and Dr. Canek Feuntes-Hernandez for their advice. I would also like to thank Cheng-Yin Wang, Wen-Fang Chou and Xiaojia Jia for preparing countless number of Ca samples for my work.

Finally, I would like to express my deepest gratitude to my Mother, Father and Brother for their continuous support and motivation.

TABLE OF CONTENTS

ACKNOWLEDGEMENTS **iv**

LIST OF TABLES **viii**

LIST OF FIGURES **ix**

LIST OF SYMBOLS AND ABBREVIATIONS **xvi**

SUMMARY **xx**

CHAPTER 1. Introduction **1**
1.1 Overview and Motivation **1**
1.2 Objectives of Dissertation **4**

CHAPTER 2. Literature review **8**
2.1 Introduction **8**
2.2 Atomic layer deposition **8**
2.3 Barrier film technology **14**
2.3.1 Permeation through a barrier film 15
2.3.2 Barrier film architectures 18
2.4 Mechanical Issues with ALD barrier films **23**
2.5 Corrosion **28**
2.5.1 Corrosion of ALD Barriers in Moisture and Ionic Solutions 28
2.5.2 ALD Barriers For Biological Environments 30
2.6 Integration with Photovoltaic Devices **33**
2.6.1 Degradation in Perovskite cells due to atmospheric gases 34
2.6.2 Encapsulation of Perovskite cells 35

CHAPTER 3. Experimental methods **37**
3.1 Introduction **37**
3.2 Optical Ca corrosion test **37**
3.2.1 Preparation and scanning of Ca substrates 40
3.2.2 Determination of permeation rates through the barrier films 41
3.3 ZnO photoluminescence test to determine ALD corrosion **49**
3.4 Electrochemical impedance spectroscopy to determine the corrosion of ALD barriers **52**
3.4.1 EIS setup 53
3.4.2 Comparison of positions in EIS cell 55
3.4.3 Impedance measurement and equivalent circuits 56
3.5 Residual Stress Measurement **59**
3.6 Efficiency measurement of perovskite solar cells **60**

CHAPTER 4. Towards Particle Defect Tolerant Ultrabarrier Films **62**
4.1 Introduction **62**
4.2 Experimental methods and modeling **63**

4.2.1 Thin-film deposition 63
4.2.2 Ca corrosion test 64
4.2.3 In situ optical microscopy tensile tests 65
4.2.4 Driving force for crack propagation 66
4.2.5 Simulation Model 68
4.2.6 Barrier film architectures for crack healing test. 69
4.2.7 Barrier film architectures for the influence of sequence of layers. 71
4.3 Results and discussion 72
4.3.1 Performance of the barrier films containing particle inclusions of different composition. 72
4.3.2 Tensile test 74
4.3.3 Finite Element Modeling 76
4.3.4 Healing of cracks with PECVD SiNx 79
4.3.5 Influence of the sequence of layers in barrier films. 81
4.4 Conclusions 85

CHAPTER 5. Side permeation in barrier encapsulation 87
5.1 Introduction 87
5.2 Experimental Methods 89
5.3 Theoretical Model Development 91
5.4 Results and discussion 97
5.5 Comparison of diffusivity through the bulk and capillaries 103
5.6 Conclusions 105

CHAPTER 6. Stability of ALD films in Biological solutions 106
6.1 Introduction 106
6.2 Experimental 107
6.2.1 Atomic layer deposition 107
6.2.2 MTT Test 108
6.2.3 Electrochemical measurements 109
6.2.4 Chemical characterization 110
6.3 Results and discussion 110
6.3.1 Cytocompatibility of ALD materials 110
6.3.2 ALD films in PBS solution 111
6.3.3 ALD films in Saliva solution 115
6.3.4 ALD films in Sweat solution 119
6.4 Conclusions 124

CHAPTER 7. Stability of ALD films in Ionic solutions 126
7.1 Introduction 126
7.2 Experimental 127
7.2.1 EIS and ZnO photoluminescence test 127
7.2.2 Materials characterization 129
7.3 Results and discussion 130
7.3.1 ALD films in NaCl solution 130
7.3.2 ALD films in sea water 132
7.3.3 ALD films in H_2SO_4 and HCl 135

7.3.4 ZnO photoluminescence test results 137
7.4 Conclusions 146

CHAPTER 8. Integration of encapsulation with perovskite cells 147
8.1 Introduction 147
8.2 Experimental 148
8.2.1 Protection of aluminium electrodes 149
8.2.2 Extension of electrodes 150
8.2.3 Buffer layer before application of adhesive tape 150
8.2.4 Device encapsulation and efficiency measurements 152
8.2.5 Results of Perovskite cell encapsulation 153
8.3 Summary 155

CHAPTER 9. Conclusions 156
9.1 Summary and Conclusions 156
9.2 Future work 161
9.2.1 Chemical stability of ALD materials 161
9.2.2 Biocompatibility of ALD materials 162
9.2.3 Encapsulation of perovskite solar cells 163

REFERENCES 165

LIST OF TABLES

Table 1	Structure of Barrier films	71
Table 2	List of samples used for tensile test with their crack onset strain, fracture energy and fracture toughness.	76
Table 3	Mechanical properties used for modeling	78
Table 4	Structure of Barrier films	90
Table 5	ALD material, precursors, pulse times, number of cycles and final thickness	108

LIST OF FIGURES

Figure 1	Schematic illustration of one ALD reaction cycle.[34]	10
Figure 2	Representative cross-sectional SEM images of 300 nm thick Al_2O_3 films deposited on Si wafers with trench structures.[36]	11
Figure 3	Schematic of ALD window.[41]	11
Figure 4	Schematic representation of thermal and plasma-assisted ALD. First half cycle is common for both of them. In second half cycle, the substrate is exposed to gaseous phase reactants (for thermal ALD) or to species generated by plasma (for plasma ALD).[35]	13
Figure 5	Schematic of the device encapsulation methods (a) direct encapsulation method where barrier films are deposited directly on the devices, (b) and (c) indirect encapsulation method where the devices and barriers films, prepared separately, are sandwiched using an epoxy sealant and an adhesive. Adapted and modified from reference.[10]	15
Figure 6	Schematic diagram showing the gas permeation pathways through different features in barrier film. The mechanism followed by the permeating species depends on the ratio of the sizes of species and feature in the barrier film.[53]	16
Figure 7	Encapsulation requirements for different kinds of device and commercial applications. (A: organic light emitting diode grade; B: solar cell grade).[54]	17
Figure 8	Schematic of different barrier structures. Polymer layer is often used for surface smoothening. Nanolaminates consist of thin alternating layers of two different ALD materials.	19
Figure 9	Schematic of a multilayered structure showing the tortuous pathway followed by the permeating species through the defects in inorganic layer and bulk of the polymer layer. Modified from reference.[58]	21
Figure 10	SEM image of a cross-section of a multilayer structure with alternate organic and inorganic layers (Vitex Systems, Trade name: Barix®). Modified from reference.[14]	22
Figure 11	(a) Type A structure with only ALD layers on polymer substrate leading to the formation of cracks due to large magnitude	26

residual stresses. (b) Type B structure without any crack due to the compensation of tensile residual stress in ALD layer with the compressive residual stresses in SiNx layer. Modified from reference.[20]

Figure 12 Schematic of different stress regions in barrier films with particle getting incorporated in the barrier at different deposition processes. 26

Figure 13 Optical images of localized cracks near particles in low stress barrier structures. Structure: 4300 nm CYTOP + 100 nm SiNx + 200 cyc Al_2O_3 + 20x(5 cyc Al_2O_3 + 5 cyc HfO_2). 27

Figure 14 Optical image of a spot in Ca sample with particle at its center. 27

Figure 15 Moisture ingress through different regions in the sample structure. 39

Figure 16 Schematic of degraded Ca for calculation of water permeation rate. 39

Figure 17 Scanned image of a Ca sample. 40

Figure 18 Scanner used for taking Ca images. 41

Figure 19 Schematic of an optical scanner. 43

Figure 20 Schematic of Ca devices on a glass substrate. The numbers represent the position of the Ca devices in terms of rows and columns. 48

Figure 21 Band structure of ZnO.[132] 50

Figure 22 Schematic of excitation of ZnO samples using 325 nm laser source and collection of PL emissions using Horiba JY LabRAM HR800 Raman Spectrometer. 51

Figure 23 Exposure of ZnO samples to different solutions. 51

Figure 24 Setup for EIS measurements. 54

Figure 25 The schematic of electrode design. (a) Pattern of Au electrode deposited on glass substrate. (b) Cross-section of the electrode showing different layers of glass substrate, electrode material and ALD coating. 54

Figure 26 Nyquist and Bode plots of Al_2O_3 in 3.5 wt. % NaCl solution at different positions in the EIS cell. 56

Figure 27 Equivalent circuits used to explain the data (a) Circuit #1, (b) Circuit #2, (c) Circuit #3. R_1, R_2, R_3 and R_4 represent resistances, C1 and C_2 represent capacitors, and CPE_1 and CPE_2 represent constant phase elements in the equivalent circuits. (d) Fitting of EIS data with different circuit models. The dots represent experimental data and solid lines represent fitted data using corresponding equivalent circuit for ZrO_2 in sea water. Color code: bare electrode (black), ZrO_2 on 1st day (red) and ZrO_2 on 21st day (green) in sea water. 58

Figure 28 Structure of the perovskite cells. 61

Figure 29 A typical JV curve for a perovskite solar cell demonstrating the performance of the cells under dark and illumination conditions. 61

Figure 30 (a) Schematic demonstrating the inclusion of particles followed by the deposition of ALD and PECVD layers on PEN substrate. This barrier is used for the indirect encapsulation of glass substrate with Ca devices using a double sided adhesive. (b) Final structure of the samples having particle inclusions. 65

Figure 31 Schematic for tensile testing showing that the particles are embedded in the ALD layer while tensile strain is being applied in the horizontal direction. Formation of cracks on the surface of the strip is monitored using a microscope. 66

Figure 32 Structure and dimensions of the sample used for FEM modeling. Inset in the figure shows assignment of seam for crack formation located at the lower portion of particle. 69

Figure 33 (a) Cross-section of ALD Al_2O_3 deposited on PEN substrate. (b) Schematic showing the bending method for applying of 2% tensile strain on ALD Al_2O_3 films deposited on PEN substrates leading to the formation of cracks. (c) Schematic of the cross-section ALD Al_2O_3 layers consisting of cracks after bending. (d) Cross-section of PECVD SiNx deposited on PEN substrate. (e) Healing of cracks in ALD Al_2O_3 by SiNx. 70

Figure 34 Schematic of samples depicting difference in barrier film architectures. 72

Figure 35 Ca samples demonstrating the effect of nature of particle contamination on performance of barrier films. 73

Figure 36 Images of first cracks in the samples at the crack onset strain. 75

Figure 37	Effect of change in modulus of particles on energy release rates with and without residual stresses in ALD layer.	79
Figure 38	Scanned images of Ca samples after exposure to humid conditions of 60°C/90%RH. These images demonstrate the degradation of Ca at different intervals representing the quality of different barriers used for their encapsulation.	81
Figure 39	Scanned images of Ca samples with time after exposure to humid environment at 60°C/90% RH.	83
Figure 40	Degradation of Ca samples on exposure to humidity at 60°C/90% RH. (a) and (b) change in Normalized Ca Area of samples with 500 nm SiNx and 1000 nm SiNx, respectively. (c) and (d) show changes in the Ca thickness for 500 nm SiNx and 1000 nm SiNx, respectively. All data show that the Ca samples show some level of degradation for Type A samples at a much earlier time than Type B samples.	84
Figure 41	Distribution of particle defects appearing in different samples. Inset in the figure shows the numbering of devices in the Ca sample.	84
Figure 42	Schematic of samples representing encapsulation using different barrier architectures (inverted barrier structure) on Ca substrates using a double-sided adhesive.	89
Figure 43	Surface forces acting at different interfaces for a droplet.	92
Figure 44	Configuration of capillary meniscus formed by the presence of water between two surfaces with different contact angles.	93
Figure 45	Optical images of Ca samples at different durations in humid environment (60°/90% RH).	98
Figure 46	(a) Image of Ca sample representing distance moved by the edge of a Ca device from its original position represented by red square box. The device numbers represent the Ca devices used for determining the movement of device edges. (b), (c) and (d) Plots of distance moved by the edges of 8 Ca devices with time for samples with PECVD SiNx, ALD TiO_2 and ALD Al_2O_3 as the interface materials, respectively. Insets in the figure represent contact angles of materials at the interface with water.	101
Figure 47	Side permeation rates for samples with different interface materials between the barrier and the adhesive.	102

Figure 48 Various permeation pathways possible for water ingress in an encapsulated device. 102

Figure 49 Diffusion coefficient of a capillary of thickness 10nm with varying contact angles on both the surfaces of a capillary. Contact angles (θ_1) for first surface are represented along x-axes. Different plots represent different values of contact angles (θ_2) for second surface. 104

Figure 50 Normalized absorbance intensity of 570 nm wavelength through the control and ALD coated coverslips. No significant difference (Dunnett's statistic test) in absorbance was observed between control group and each different sample coated coverslips, indicating ALD coatings were cytocompatible. 111

Figure 51 EIS response in PBS for (a) Al_2O_3, (b) HfO_2, (c) TiO_2, and (d) ZrO_2 over a time period of 21 days. Dotted line represents impedance response from bare electrode. Blue arrows point towards the direction of measured data. Insets in the figure represent phase response for first and last measurement. Red arrow point towards the appearance of second time constant in the phase plots. 114

Figure 52 XPS spectra of metallic elements. Color code: Black represents binding energy for native samples (before exposure) to biological solutions. Red, green and blue represent binding energy for samples in PBS, saliva and sweat after exposure for 21 days, respectively. 115

Figure 53 EIS response in saliva solution for (a) Al_2O_3, (b) HfO_2, (c) TiO_2, and (d) ZrO_2 over a time period of 21 days. Dotted line represents impedance response from bare electrode. Blue arrows point towards the direction of measured data. Insets in the figure represent phase response for first and last measurement. Red arrow point towards the appearance of second time constant in the phase plots. 119

Figure 54 EIS response in sweat solution for (a) Al_2O_3, (b) HfO_2, (c) TiO_2, and (d) ZrO_2 over a time period of 21 days. Dotted line represents impedance response from bare electrode. Blue arrows point towards the direction of measured data. Insets in the figure represent phase response for first and last measurement. Red arrow point towards the appearance of second time constant in the phase plots. 123

Figure 55 (a) Schematic of setup for PL measurement from ZnO, (b) Exposure of ZnO samples to different solutions. 129

Figure 56 EIS response in 3.5% NaCl solution for (a) Al_2O_3, (b) HfO_2, (c) TiO_2, and (d) ZrO_2 over a time period of 21 days. Dotted line represents impedance response from bare electrode. Blue arrows point towards the direction of measured data. Insets in the figure represent phase response for first and last measurement. Red arrow point towards the appearance of second time constant in the phase plots. 132

Figure 57 EIS response in sea water for (a) Al_2O_3, (b) HfO_2, (c) TiO_2, and (d) ZrO_2 over a time period of 21 days. Dotted line represents impedance response from bare electrode. Blue arrows point towards the direction of measured data. Insets in the figure represent phase response for first and last measurement. Red arrow point towards the appearance of second time constant in the phase plots. 134

Figure 58 EIS response in HCl (pH4) for (a) Al_2O_3, (b) HfO_2, (c) TiO_2, and (d) ZrO_2 over a time period of 21 days. Dotted line represents impedance response from bare electrode. Blue arrows point towards the direction of measured data. Insets in the figure represent phase response for first and last measurement. Red arrow point towards the appearance of second time constant in the phase plots. 136

Figure 59 EIS response in H_2SO_4 (pH4) for (a) Al_2O_3, (b) HfO_2, (c) TiO_2, and (d) ZrO_2 over a time period of 21 days. Dotted line represents impedance response from bare electrode. Blue arrows point towards the direction of measured data. Insets in the figure represent phase response for first and last measurement. Red arrow point towards the appearance of second time constant in the phase plots. 137

Figure 60 PL from ZnO substrates coated with (a) Al_2O_3, (b) HfO_2, (c) TiO_2, and (d) ZrO_2 before and after soaking for 21 days. 142

Figure 61 Surface scan of (a) Al_2O_3, (b) HfO_2, (c) TiO_2, and (d) ZrO_2 coated samples using XPS. 143

Figure 62 (a) Optical image of HfO_2 coated ZnO sample after 10 days HCl solution, (b) PL from dark and light regions, (c) XPS depth profile of light region, (d) XPS depth profile of dark region. 144

Figure 63 XPS depth profiles for (a) TiO_2 and (b) ZrO_2 coated ZnO samples in HCl after 21 days. 145

Figure 64	Pitting type corrosion of oxide films.	145
Figure 65	Deposition of Au electrodes on exposed Al electrodes to increase the robustness and to protect them from oxidation in open atmospheric condition.	149
Figure 66	Deposition of Au electrodes on FTO electrodes along sides of the devices.	150
Figure 67	Schematic of protection of electrodes during PECVD SiNx deposition.	151
Figure 68	Schematic of device encapsulation with different layers.	152
Figure 69	JV curves and efficiency measurements of the devices.	154
Figure 70	Images of PSCs after the deposition of 500 nm of PECVD SiNx at 110°C.	163

LIST OF SYMBOLS AND ABBREVIATIONS

a	area
C	concentration
E	Young's modulus
eV	electron volt
F	force
G	energy release rate
h	thickness
I	current
I	intensity of light
J	mass flux
J_{sc}	short-circuit current density
K	stress intensity factor
m	moles
M	molar mass
P	power
R	reflectance

T	transmittance
t	time
V	voltage
V_{oc}	open circuit voltage
w	weight
Z	dimensionless energy release rate
γ	surface energy
η	efficiency
θ	contact angle
μ	attenuation coefficient
ν	Poisson's ratio
ρ	density
σ	stress
ALD	atomic layer deposition
AP-ALD	atmospheric pressure atomic layer deposition
CB	conduction band
CCD	charge-coupled device
CVD	chemical vapor deposition

DEZ	diethyl zinc
DLC	diamond-like carbon
DMEM	Dulbellcco's Modified Eagle's Media
dpi	dots per inch
EIS	electrochemical impedance spectroscopy
FF	fill factor
HTM	hole-transporting material
IPA	isopropyl alcohol
IR	infrared
LED	light emitting diode
MEMS	Microelectromechanical systems
MLD	molecular layer deposition
OPV	organic photovoltaics
OTR	oxygen transmission rate
PBS	phosphate buffered saline solution
PCE	power conversion efficiency
PEALD	plasma enhanced atomic layer deposition
PECVD	plasma enhanced chemical vapor deposition

PEN	polyethylene naphthalate
PET	polyethylene terephthalate
PL	photoluminescence
PSCs	perovskite solar cells
PTFE	polytetrafluoroethylene
PVD	physical vapor deposition
RH	relative humidity
sccm	standard cubic centimeters per minute
SEM	scanning electron microscope
TDMAH	tetrakis(dimethylamido) hafnium
TDMAT	tetrakis(dimethylamido) titanium
TDMAZ	tetrakis(dimethylamido) zirconium
TMA	trimethylaluminum
UV	ultraviolet
VB	valence band
WVTR	water vapor transmission rate
XPS	X-ray photoelectron spectroscopy
XRD	X-ray diffraction

SUMMARY

Over the past decade, a wide range of electronic devices have been developed that require barrier film technologies to improve their lifetime. For example, organic electronic devices have the ability to produce light weight, scalable and flexible electronics. Despite having several advantages over their peers, the commercial application of such devices is still challenging as they are prone to rapid degradation on exposure to atmospheric species like oxygen and water vapor. The stability of such devices can be increased by using a barrier layer that prevents the ingress of oxygen and water vapor to the active layers in the devices. More recently, perovskite solar cells (PSCs) have attracted significant attention from the photovoltaics community through their rapid advancement in power conversion efficiency which has gone above 20% in less than a decade. However, their poor environmental stability is a major challenge that needs to be addressed before any practical application. Just like organic electronic devices, PSCs are also prone to degradation by the atmospheric species. Other miniaturized electronic devices, including bioimplants and wearables, have been developed which operate either inside or worn outside the human body. Such devices are exposed to different bodily fluids which are corrosive in nature.

In the quest to make barrier films for these applications, several studies have been conducted using a variety of vacuum deposition techniques, out of which, ALD has shown the greatest potential for making ultra-thin barrier films because of their ability to form conformal and pinhole free films. Low temperature grown ALD barrier films are desirable since the organic materials they are coated onto cannot withstand high temperatures. For this, plasma-enhanced ALD (PEALD) has been used to process films at low temperatures.

Recent studies have demonstrated water vapor transmission rates of PEALD films to be on the order of 10^{-6} g/m^2/day which is desirable for commercial applications. However, the existence of defects in the barrier films significantly deteriorate their quality. Various architectures using nanolaminates and hybrid structures have been tested to minimize the impact of defects in the barrier, but none have been able to achieve the desired level of permeation resistance against atmospheric species in the presence of particle contamination. The particles can get incorporated into the barrier structure during any stage of fabrication leading to the formation of defects. It is commercially expensive to maintain ultraclean environment throughout the fabrication of barrier films to avoid particle contamination. Thus, there is a need to develop a robust structure of the barrier film which has sufficient tolerance to these defects.

Most of the studies conducted on the fabrication of barrier films have limited their approach to improve the permeation resistance against atmospheric species through the thickness of the barriers. In case of indirect encapsulation, despite having high quality barrier films, atmospheric species can permeate to the active regions of the devices through the interface between the barrier and sealant. Sealants are often used along the sides of the encapsulations to protect the devices from side permeation of atmospheric species. Still, a significantly higher permeation rate, as compare to that through the thickness of the barrier, exists through the sides of the encapsulation. Thus, there is a need to have a larger control over the rates of side permeation.

The direct deposition of ALD on PSCs also has additional issues beyond defects in the barriers, namely in the chemical compatibility with the deposition process. Several studies have shown that plasma and ozone can lead to the degradation of devices. High

temperature deposition is not possible due to the thermal instability of PSCs. The adhesive material, used during indirect encapsulation, can interact chemically with the PSCs leading to their degradation. This calls for the development of appropriate strategies for the encapsulation of perovskite cells to enhance their stability and lifetime.

In addition to permeation barriers for atmospheric species, ALD films can also have application as protective barriers for electronic devices in harsher environments consisting of various ionic and biological species. Such conditions may exist in solar cell encapsulations or in newer applications like biomedical implants. Very little has been done so far to understand the corrosion resistance of ALD barrier films in different ionic and biological environments.

In this dissertation, to address the issue of defect formation due to particle contamination, first, the impact of particles with different mechanical properties on crack formation in ALD barrier films has been investigated. It has been demonstrated that particles with lower elastic modulus are more likely to form cracks as compared to those with higher elastic modulus. Later, the study focuses on the healing of cracks created due to particle contamination. It has been experimentally shown that the performance of an ALD barrier film consisting of several cracks can be improved significantly by filling the crack openings using PECVD SiNx. Due to the crack healing effect of PECVD SiNx on ALD layers, it was suggested that the order of deposition when creating such ALD/PECVD hybrid barriers matters. It has been shown that ALD depositions should always be followed by the deposition of PECVD SiNx as it can heal the defects in the ALD layer, thereby, improving the performance of ALD barrier containing defects.

To address the issue of side permeation, we studied the impact of the outer layer of the barrier in contact with an edge sealant on the side permeation rates for a given barrier sealant/adhesive. It was found that the amount of moisture permeating through the sides of the barrier encapsulation is several orders of magnitude higher than the permeation through the barrier film. It has been shown that the rate of side permeation can be controlled by changing the materials at the interface. The strong dependency of the moisture permeation rate on the contact angle of water on the material at the interface has been demonstrated. It has, therefore, been recommended to use materials with higher contact angles at the interface to reduce the side permeation rate for water.

The next part of this dissertation focuses on the stability and reliability of the ALD barrier films in harsh chemical environments. For extending the domain of ALD barriers from just gas permeation barriers, the chemical stability of ALD materials was investigated in a variety of solutions including ionic and biological media. This study uses a combination of PL emission, XPS, EIS, and cytocompatibility analysis to determine the corrosion resistance of several ALD metal oxides as well as their biocompatibility.

The last section of this dissertation deals with the application of ALD barrier films for the encapsulation of PSCs. The chemical sensitivity of the PSCs makes it difficult to directly integrate many known encapsulation processes. Therefore, the concept of using PECVD SiNx on top of the PSCs as a chemical buffer layer prior to applying various encapsulation materials has been introduced. PECVD SiNx helps in preventing any interaction between the PSCs and barrier materials during the encapsulation process. It, therefore, introduces the possibility of using a variety of indirect encapsulation techniques and barrier structures for improving the lifetime of PSCs.

CHAPTER 1. INTRODUCTION

1.1 Overview and Motivation

Organic electronics, perovskite cells, biological implants and wearable devices are rapidly developing fields leading to the development of advanced and highly efficient devices.[1-6] The success of these technologies depends on the advancement in material and device design that enhance their stability and efficiency while being amenable to scalable manufacturing methods. However, the intrinsic vulnerability of these electronic devices to their surrounding environment highlights the need for the development of an effective permeation barrier technology that can prevent the exposure of the devices to harmful species from the surrounding environment.[7-11] These barriers should be stable under different exposure conditions while maintaining their functionality.

For organic electronics, studies have shown that barriers should have a water vapor permeation rate (WVTR) and oxygen transmission rate (OTR) on the order of 10^{-6} g/m^2/day and 10^{-3} cc/m^2/day/atm, respectively for devices to function for a period of at least 10 years.[12, 13] Several studies have shown that using ALD based barrier films, the required value of WVTR can be achieved.[14-17] Because of the presence of defects in single ALD layers, multilayer and hybrid barrier structures have been introduced which help in decoupling of the defects while increasing the lag-time for moisture permeation.[18-22] However, the effectiveness of these barriers is severely affected by the inclusion of particle contamination which results in the formation of cracks.[20] With the manufacturing constraints for large scale production, it is expensive and not possible to manufacture barrier films completely free from particle contamination. This raises the question of

whether it is possible to design barrier films such that they are more defect tolerant and provide the ultrabarrier performance required for application to devices. If this is possible, it will allow barriers to be manufactured without strict clean environments and cleaning steps currently needed by industry, allowing a pathway to lower cost.

In the integration of ultrabarrier films with electronics, the barrier can be deposited onto the devices (direct encapsulation) or deposited onto a substrate and attached to the electronics using an adhesive and/or edge sealant (indirect encapsulation). The direct encapsulation approach eliminates the need for adhesives and edge sealants, but requires that the electronic device be compatible with the deposition process for the barrier (e.g., temperature, duration, etc). For indirect encapsulation, the deposition compatibility is only with the substrate and can thus be attached to electronics sensitive to processing temperatures and environments, as long as the devices are amenable to the attachment adhesives/sealants. The issue then arises that side permeation can occur through the edge sealant and thus, barrier adhesives/sealants have been developed to help match the properties of the ultrabarrier. However, the edge permeation often remains the weak link. While most people consider the permeation through the adhesive/edge sealant, there has been little thought as to the permeation along the interface where the barrier comes into contact with the adhesive. This interface is imperfect and can contain micro or nanovoids which allows permeation of water vapor. Thus, surface properties at this interface can play a role in the side permeation during indirect encapsulation. Thus, the question remains: is it possible to impact the side permeation rate with indirect encapsulated devices by judiciously choosing materials with the appropriate surface energies that may slow water ingress?

Similar to organic electronic devices, barriers are desirable for perovskite solar cells (PSCs) as well. PSCs are based on inorganic perovskite materials and have shown a very rapid increase in their efficiency up from 3.81% in 2009 to about 20.3% in 2014.[23-25] This makes them a promising candidate to replace conventional silicon based solar cells. Various PSC fabrication techniques have been introduced which includes dual source vapor deposition, vapor-assisted solution process, and low-temperature solution casting, etc., with a continuous improvement in device performance.[26-28] The materials used for the fabrication of PSCs, however, are prone to degradation on exposure to moisture and high temperature conditions.[29] Although, there has been a significant improvement in the efficiency of PSCs in a very short time, only a few investigations have focused on stability, degradation and encapsulation of the devices.[30-32] Whenever encapsulation is carried out on PSCs using either direct or indirect encapsulation method, there is a potential to rapidly degrade devices if the encapsulation process is not chemically compatible with the PSC. Hence, there is a need to develop a fabrication methodology such that the direct interaction between the barrier materials and PSCs can be avoided or is chemically inert. Thus, the question remains: is it possible to insert a chemical barrier layer between the PSC and encapsulation materials such that a wide range of ultrabarriers can be introduced in the packaging of PSCs?

As mentioned above, ALD based barrier films have mostly been used in the fabrication of barriers for protecting the electronic devices from atmospheric gaseous species. However, owing to the control in thickness, high density, pin-hole free and conformal nature of the films, ALD films can have potential application in the fabrication of barrier films for devices that are used in different chemical environments like biological

implants and wearable devices. With the advancement in technology, several miniaturized electronic devices have been developed which operate either inside or worn on the human body. During their normal operating conditions, such devices are exposed to different biological fluids which are corrosive in nature. For long term and continuous operation of the devices, there is a need for a protective layer to prevent them from getting corroded by the surrounding media. Therefore, ALD based barriers can play a significant role in fabricating ultrathin conformal barriers which can protect the devices while maintaining their functionality. Also, there are numerous applications where electronics can be exposed to harsh chemical environments including acidic or ionic (e.g., saltwater). In all of these aforementioned cases, the long term durability of ALD barrier films, especially those in biological solutions, has not been reported. Thus, the questions would be: how do we test the corrosion stability of ALD ultrabarrier films, how quickly do ALD metal oxides degrade in harsh chemical environments, and which materials show superior stabilility even at <20 nm thickness? Therefore, for using ALD in fabricating barrier films for biological implants, wearable devices and electronics in harsh chemical environments, it is necessary to understand the corrosion behavior of different ALD materials in the environments consisting of various ionic and biological species.

1.2 Objectives of Dissertation

The objective of this research is to address the fundamental issues of ALD based barrier films that can be used to improve the lifetime and reliability of electronic devices. As gas permeation barriers, ALD films often incorporate particle contamination during the

manufacturing processes resulting in the formation of cracks in the barriers which act as free permeation pathways for moisture. When used for indirect encapsulation, there is issue of side permeation through the interfaces between the barrier and encapsulant material. This work addresses both these issues in case of moisture permeation barriers. The first objective is, therefore, to devise a technique that can make barrier films tolerant of particle contamination and control the rate of side permeations through the interfaces. With the potential of ALD barrier films to be used for protecting the electronic devices in various chemical and biological environments, this work explores the chemical stability of various ALD materials in environments consisting of various ionic and biological species. This study is to determine the ALD materials that are suitable for application in a particular kind of environment. Lastly, due to the sensitivity of the PSCs to different encapsulation methods, the objective of this work is to devise a fabrication method that can facilitate the encapsulation of PSCs. As per the objectives, this dissertation is organized as following.

Chapter 2 gives the introduction to the PECVD and ALD deposition techniques used for the deposition of thin films during the fabrication of barrier films for the encapsulation of various devices. It also discusses the recent developments in barrier film technology and the various aspects of different barrier architectures. It later describes the mechanical and corrosion related issues with the barrier film materials. Lastly, it describes the recent developments and encapsulation related issues for perovskite cells.

Chapter 3 describes all the experimental and measurement techniques used in this dissertation. It includes the description of Ca corrosion tests and indirect encapsulation methods used to determine the performance of barrier films for organic electronic devices. It also presents a method combining ZnO photoluminescence tests and electrochemical

impedance spectroscopy for the determination of chemical stability of ALD films in ionic and biological solutions. Lastly, it describes the various aspects for the measurement of efficiency of perovskite solar cells used as a demonstration platform for the application of developed barrier film technology.

Chapter 4 addresses the question of whether it is possible to develop barrier films that are defect tolerant. To do so, this chapter first describes the effect of particle inclusions in the barrier film performance. It deals with the mechanics and deformation in the vicinity of particle inclusions which can lead to the formation of defects in the encapsulation. The chapter also explores methods to mitigate the impact of defects on water vapor permeation by using hybrid deposition processes to heal crack that can be generated by particles. This addresses the defect tolerance aspect of barrier film processing including the impact of the order of film deposition in the barrier architecture.

Chapter 5 addresses the question of whether the surface energy of the outer layer of the barrier film can impact the side permeation in indirect encapsulated devices. First describes the impact of side permeation in barrier films that are applied to devices using encapsulants and edge sealants. It shows the correlation between the rate of side permeation through the bonded interface and its relationship with surface properties of the outer barrier layer. These results aim to show the role of side permeation through the edge sealant as well as along the interface between the barrier and the edge sealant. This is a significant permeation pathway which has received little attention by researchers before this study.

Chapter 6 and chapter 7 addresses the questions surrounding the chemical stability and reliability of ALD films in biological and ionic solutions, respectively. Experimental

methods were developed evaluate the corrosion of ALD films in these solutions and provide insight into the nature of their degradation. In addition to chemical stability tests, chapter 6 also includes the cytocompatibility test used for the determination of toxicity of ALD materials to the living cells.

Chapter 8 deals with the integration of barrier films with the perovskite cells and the question of whether it is possible to use an inorganic interlayer to improve the integration of barrier films with PSCs. It first describes the complexity and challenges for the application of any kind of barrier encapsulation of perovskite cells. In an attempt to improve the chemical stability of the perovskites with barrier applications, an inorganic interlayer was inserted between the barrier and perovskite. Experiments are then performed to determine the performance of the perovskites after the insertion of the inorganic layer and the attachment of the barrier films.

Finally, chapter 9 summarizes the achievements and the contributions of this dissertation and discusses future work.

CHAPTER 2. LITERATURE REVIEW

2.1 Introduction

This chapter will provide the basics of atomic layer deposition (ALD) technique used for the manufacturing of barrier films. Afterwards, fundamentals of the barrier film technology, its requirements, and different strategies for characterizing their performance are discussed. Following this, the current research issues in barrier film technology, which are the focus of this dissertation, will be presented. This includes mechanical and chemical reliability of barrier films.

2.2 Atomic layer deposition

Atomic layer deposition (ALD) is a thin film fabrication technique used for manufacturing inorganic materials with thicknesses down to the precision of a single atomic layer.[33] It is based on the sequential use of self-terminating surface reactions which can be described by the following steps as shown in Figure 1.[34]

(1) Introduction of the first reactant which forms a single monolayer on the substrate surface.
(2) Purging of the unreacted first reactant and gaseous by-products of the reaction in the first step.
(3) Introduction of the second reactant which reacts with the monolayer formed in the first step.

(4) Purging of the unreacted second reactant and gaseous by-products of the reaction in the third step.

The first and third steps are self-limiting in nature and are often called half reaction processes. Due to self-limiting nature of half reactions, the thickness of films deposited can be controlled with the precision of a single atomic layer which is typically in the range of 0.05 nm to 0.1 nm.[35] All of the above described steps constitute one ALD cycle and the amount of material deposited in one ALD cycle is termed as growth per cycle (GPC). A single layer of desired material is obtained at the end of one complete ALD cycle. Therefore, by repeating the number of ALD cycles, desired thickness of material can be deposited. As the materials are deposited by single layer of precursors from half reactions, a uniform cover of material is deposited irrespective of the nature of the substrate surface. Thus, the ALD films are highly conformal in nature as shown in Figure 2.[36] ALD films are, therefore, considered to be a good candidate for producing defect-free conformal barrier films.[18, 19, 37-39]

For successful completion of the ALD process, several conditions need to be satisfied. During the introduction of the precursors/ reactants, there is simultaneous adsorption and desorption processes of reactant species on the substrate surface. The thermal energy of the system should be such that it allows the formation of a monolayer of the reactant species following its simultaneous adsorption and desorption. Therefore, the ALD processes are carried out in a specific range of temperatures which is termed the 'ALD temperature window'.[40] The schematic for the ALD window is shown in Figure 3.[41] The temperatures outside of this window result in either poor quality films or non-ALD type depositions. Low temperatures can result in condensation of the precursors on

the substrate surface and/or slow reaction kinetics, whereas, high temperature can result in decomposition of the precursors and/or rapid desorption of the precursors from the substrate surface leading to incomplete layer formation.[40]

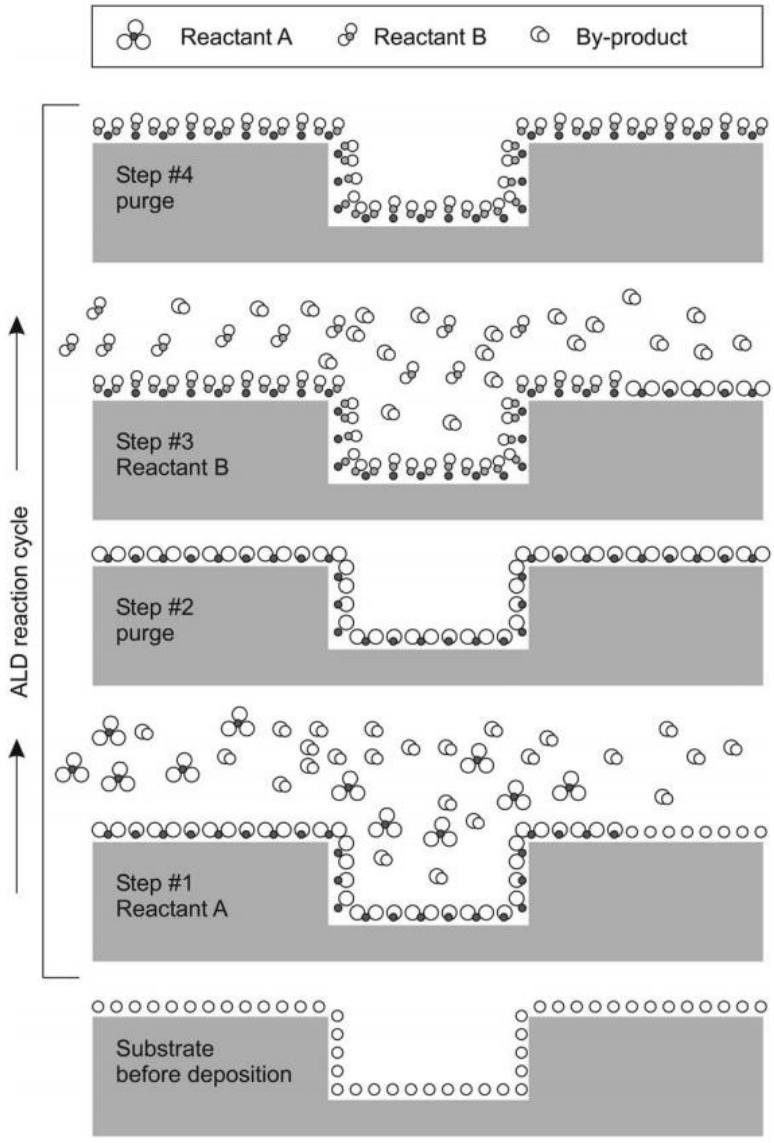

Figure 1 - Schematic illustration of one ALD reaction cycle.[34]

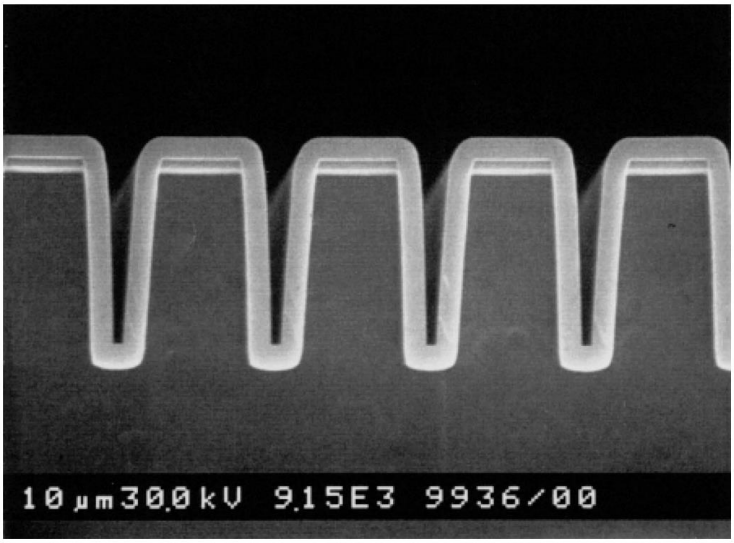

Figure 2 - Representative cross-sectional SEM images of 300 nm thick Al_2O_3 films deposited on Si wafers with trench structures.[36]

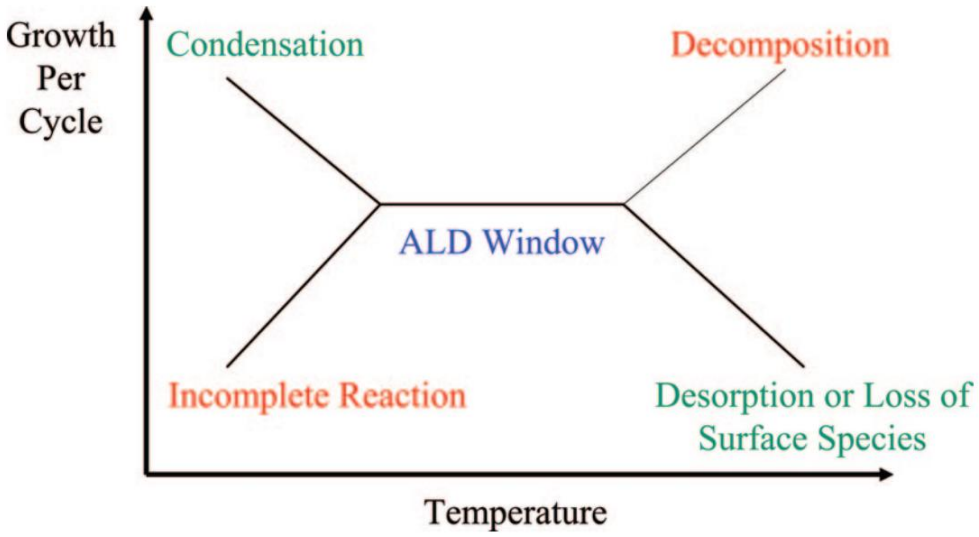

Figure 3 - Schematic of ALD window.[41]

Thin films deposited using atomic layer deposition (ALD) technique have been shown to produce high quality thin barrier films for applications in the protection of electronic devices. As compared to other deposition techniques like CVD and physical vapor deposition (PVD), ALD provides films that tend to be very continuous and pin-hole free.[33] Despite having great advantages over other deposition techniques, ALD has mainly two drawbacks, namely high deposition temperature and slow deposition rate. During the ALD processing where thermal energy is used to drive the reaction (thermal ALD) the surface reactions are governed by the temperature of the substrates which typically needs temperatures in the range of 100°C – 350°C.[35, 42] This high deposition temperature limits the use of ALD while manufacturing barrier films for electronic devices like OLEDs which typically have the maximum processing limit is of 130°C.[43] Although the depositions using thermal ALD can be carried out at 100°C, the films have relatively higher impurity content due to unfinished reactions because of the low temperature.[35] After the introduction of Plasma ALD, which uses high power plasma during reaction process, the temperature required for carrying out ALD process has been brought down to room temperatures.[44-46] It should be noted that the direct deposition of plasma assisted ALD will be subject to the reactivity of the devices with plasma processing. The schematics representing the thermal and plasma-assisted ALD are shown in Figure 4.[35] The second issue of slow deposition rates results from long purge times required to remove the unreacted species in each cycle. For countering this issue of slow deposition rate, spatial ALD technique, which is a variant of thermal ALD, has been introduced in which the ALD precursors are present in separate chambers and the substrate is alternately moved through the chambers until desired thickness is achieved or the substrate is moved underneath an

alternating precursor and inert gas delivery shower head in order to expose the substrate to the cycles needed to create the ALD film.[47-50] Plasma-assisted ALD also provides advantages of improved deposition material, better control over stoichiometry and film composition, and increased growth rate over thermal ALD.[35] Introduction of atmospheric pressure ALD (AP-ALD) has further increased the possible applications of ALD.[48, 51]

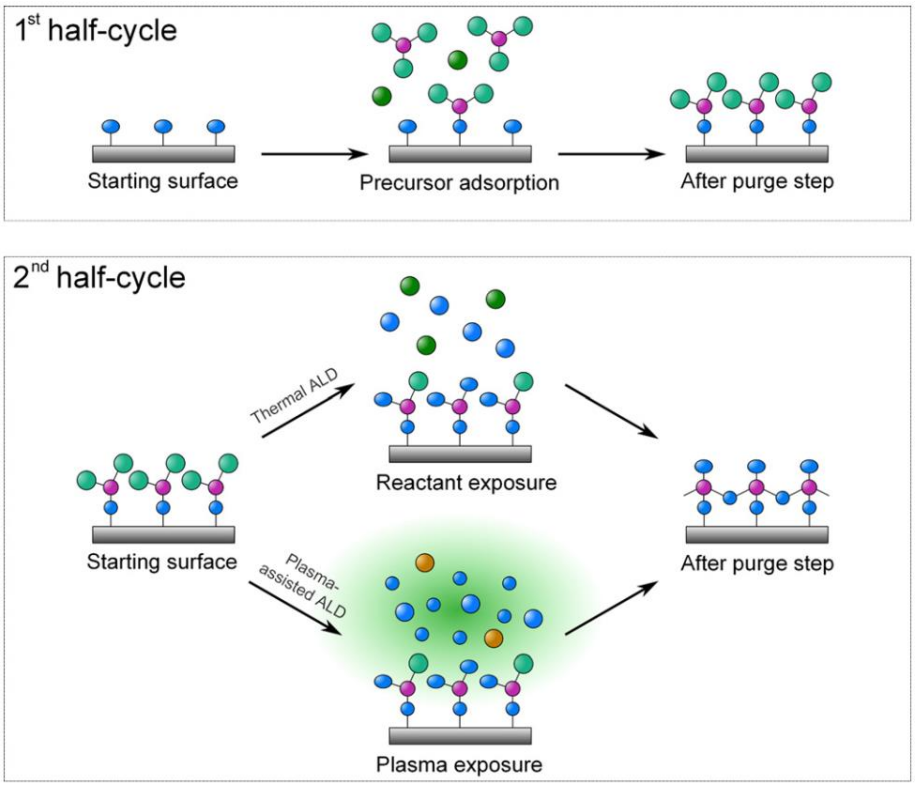

Figure 4 - Schematic representation of thermal and plasma-assisted ALD. First half cycle is common for both of them. In second half cycle, the substrate is exposed to gaseous phase reactants (for thermal ALD) or to species generated by plasma (for plasma ALD).[35]

2.3 Barrier film technology

Glass barriers are very effective as oxygen and moisture permeation barriers, but restrict the flexibility of organic electronic devices. Glass barriers are also heavy in weight which adds to maintenance and handling costs. On the contrary, films deposited using atomic layer deposition (ALD) have the potential to make flexible barrier films. ALD deposited metal oxides like aluminum oxide (Al_2O_3), titanium dioxide (TiO_2) and zirconium oxide (ZrO_2) have been quite extensively researched because of their ability to form highly dense and conformal coatings for ultra-barrier architectures.[7, 18, 20, 21, 52] Encapsulation methods using these materials include direct deposition of barrier films on the device and deposition of barrier on a flexible lid followed by sealing of the device as shown in Figure 5.[10] Figure 5(a) shows that the barrier layer is first deposited on the polymer substrate and then the device is fabricated on top of it. Following this, another layer of barrier film is deposited directly on the device. This method is called direct deposition method. If the substrate is glass, then there is no need to deposit a first barrier layer. Figure 5(b) and (c) demonstrate the structures in case of indirect encapsulation method. In this method, barrier films and devices are prepared separately on their respective substrates, and then both of them are sandwiched together using a sealant along the sides of the structure (Figure 5(b)), or an adhesive layer applied uniformly all over the devices (Figure 5(c)). The application of any of these methods for encapsulation depends upon the nature of device and encapsulation manufacturing conditions. The direct encapsulation method can be applied in case where the devices are stable under the processing conditions for barrier film fabrication because the barrier film materials are deposited directly on the devices. The temperature of the depositions should also not affect

the devices. Whereas, for indirect encapsulation, temperature and barrier film manufacturing processes are not of any concern as the barrier films are prepared separately. However, issues of delamination and debonding may arise while using epoxy sealants. Also, care needs to be taken while using adhesives as there could be some chemical interaction between the adhesive and the device which can adversely affect or even kill the devices. Therefore, the compatibility of the encapsulation process with the device must be taken into consideration.

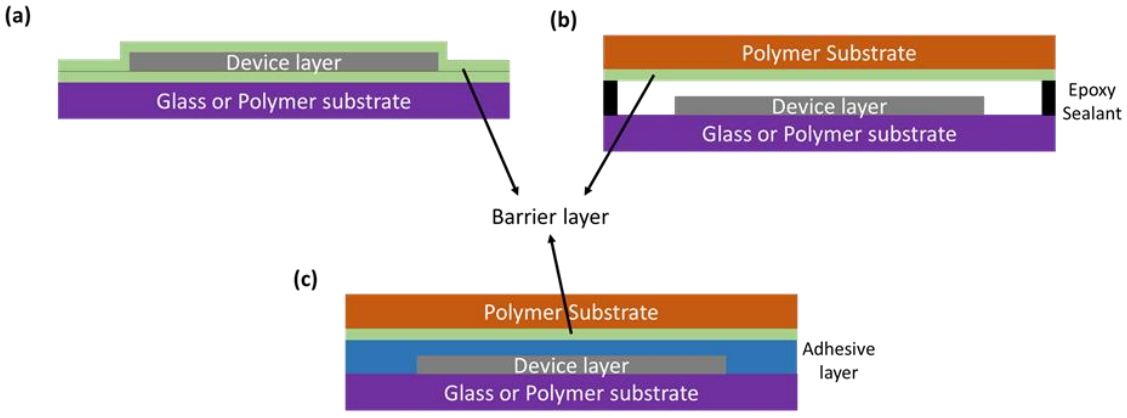

Figure 5 - Schematic of the device encapsulation methods (a) direct encapsulation method where barrier films are deposited directly on the devices, (b) and (c) indirect encapsulation method where the devices and barriers films, prepared separately, are sandwiched using an epoxy sealant and an adhesive. Adapted and modified from reference.[10]

2.3.1 Permeation through a barrier film

The permeation of gaseous species, water vapor and oxygen, from the atmosphere through the barrier films takes place through different mechanisms depending on the nature

of pathway through which permeation occurs. The permeation pathways could be pores and defects like cracks in the barrier film. The permeation mechanism depends upon the size of permeating species and the size of permeation pathways, as shown in Figure 6.[53] Perrotta *et al.* have shown that pores larger than 1 nm in the barrier films lead to mediocre performance.[16] They found that with just 1% of porosity with pores larger than 1 nm can lead to the WVTR of 10^{-2} to 10^{-3} g/m^2/day. They also mention that the pore size range of 0.3 to 1 nm and its relative content can control the transition in WVTR between 10^{-4} to 10^{-6} g/m^2/day.[16] Therefore, it is highly significant to have control over the residual nanoporosity in the barrier film.

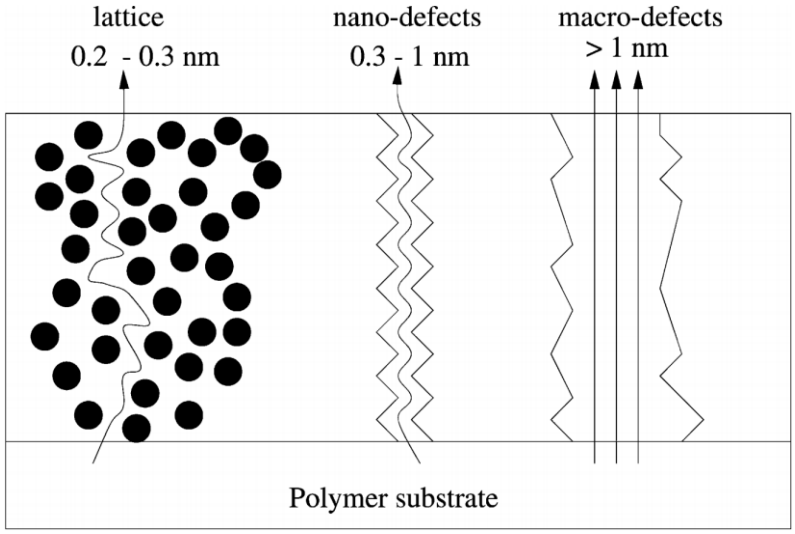

Figure 6 - Schematic diagram showing the gas permeation pathways through different features in barrier film. The mechanism followed by the permeating species depends on the ratio of the sizes of species and feature in the barrier film.[53]

The range of requirements for permeation rate of gaseous species through the barrier films depends on the type of application. Figure 7 shows the value of OTR and WVTR required for the commercial applications from various fields.[54] It is shown in the Figure 7 that organic electronics based devices require the lowest permeation rates with WVTR of $< 10^{-6}$ g/m^2/day.

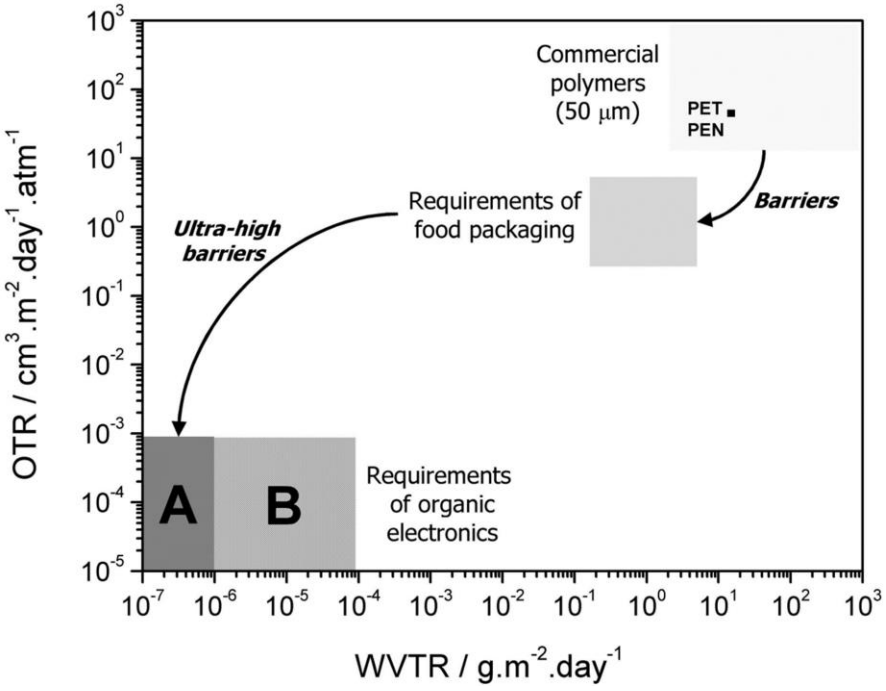

Figure 7 - Encapsulation requirements for different kinds of device and commercial applications. (A: organic light emitting diode grade; B: solar cell grade).[54]

The permeation rate, which is analogous to mass flux, depends on the diffusion coefficient of the barrier film which is a material property. The relation between mass flux and diffusion coefficient is represented by equation 2.1, as shown below.

$$J = -D\frac{\Delta C}{\Delta x} \tag{2.1}$$

where, J is flux through the barrier film, D is the diffusion coefficient, ΔC is the concentration difference across the barrier film and Δx is the thickness of the barrier film. Thus, in order to reduce the magnitude of flux through the barrier film, the diffusion coefficient can be reduced or the thickness of the barrier can be increased. As the diffusion coefficient is a material property, its intrinsic property can only be controlled through material processing which may be limited by the compatibility of the substrate or devices on which it is being deposited. Therefore, the quality of the material being deposited eventually determines the performance of the barrier film.

2.3.2 Barrier film architectures

As mentioned in the previous section, ALD deposited materials are expected to take the form of ultrathin, highly conformal and pinhole-free films. Thus, even a single layer of ALD, as shown in Figure 8(a), should be able to act as a perfect barrier. However, the imperfections created in the ALD layer during the fabrication processes and the introduction of particle defects into the barrier structure can severely affect the performance of the barrier as the defects created by particles lead to localized permeation pathways for moisture.

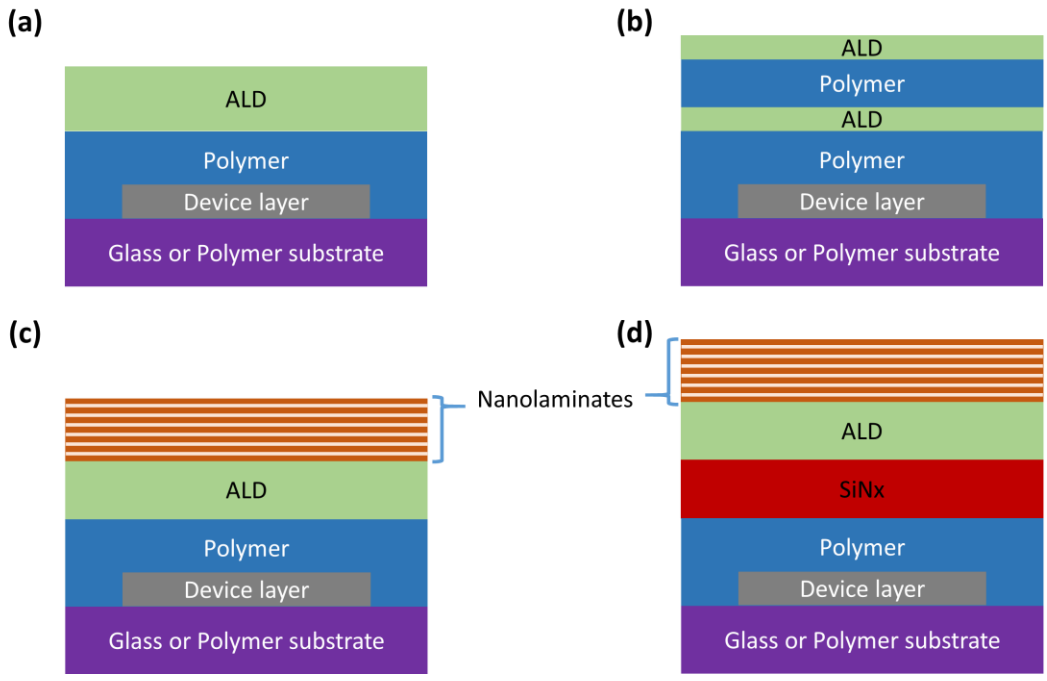

Figure 8 - Schematic of different barrier structures. Polymer layer is often used for surface smoothening. Nanolaminates consist of thin alternating layers of two different ALD materials.

One way to get over the effect of imperfections is to increase the thickness of the barrier film as it lowers the value of WVTR.[55, 56] However, increasing the thickness of the barrier films is limited by the ability to process the barrier on the device in a practical amount of time. Also, with the increase in the thickness, the flexibility of the barrier film is compromised because the value of critical onset strain decreases with increase in the thickness of the film.[57] Therefore, simply increasing the thickness of the barrier films is not always a viable option.

The performance of barrier films can be improved over single layers by using laminate structures which have alternating polymer and inorganic layers, as shown in

Figure 8(b) and Figure 9.[58] With the use of a polymer layer in between two inorganic layers, the defects across the inorganic layers are decoupled. Thus, the permeation takes place through the defects and bulk of the polymer in the form of a tortuous path as shown in Figure 9.[58] This increases in the length of the total permeation path covered by the permeating species increases the lag-time. The performance of barrier films fabricated using this strategy is governed by several factors like the size of defects, thickness of the polymer layer and average distance between the defects. The lag time increases with decrease in the thickness of the polymer layer and reduction in the size of defects as both of these reduce the rate of permeation. Increase in the average distance between the defects also increases the lag time by increasing the distance covered by the permeating species in the polymer layer.[58]

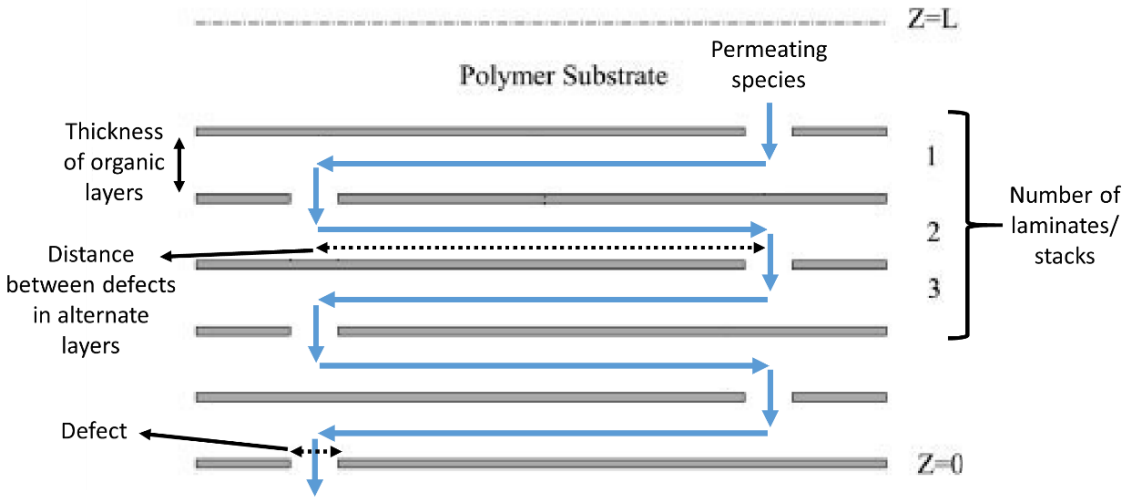

Figure 9 - Schematic of a multilayered structure showing the tortuous pathway followed by the permeating species through the defects in inorganic layer and bulk of the polymer layer. Modified from reference.[58]

Figure 10 shows the SEM cross-section image of a multilayered barrier film with alternate layers of organic (polyacrylate) and inorganic (Al_2O_3) materials.[14] One layer of each material together in the barrier structure is called a dyad as shown in the Figure 10. By using 5 dyads in the barrier structure, a WVTR of 10^{-6} g/m^2/day was achieved. In this structure, the inorganic layers of Al_2O_3 were deposited using sputtering and the organic layers of polyacrylate were deposited using evaporation followed by UV curing. The polymer layer of polyacrylate has multiple functions in this kind of structure: it acts as a smoothening layer, fills some of the defects in the inorganic layers and also acts as a buffer against any mechanical damage to the inorganic barrier layer of Al_2O_3.[14]

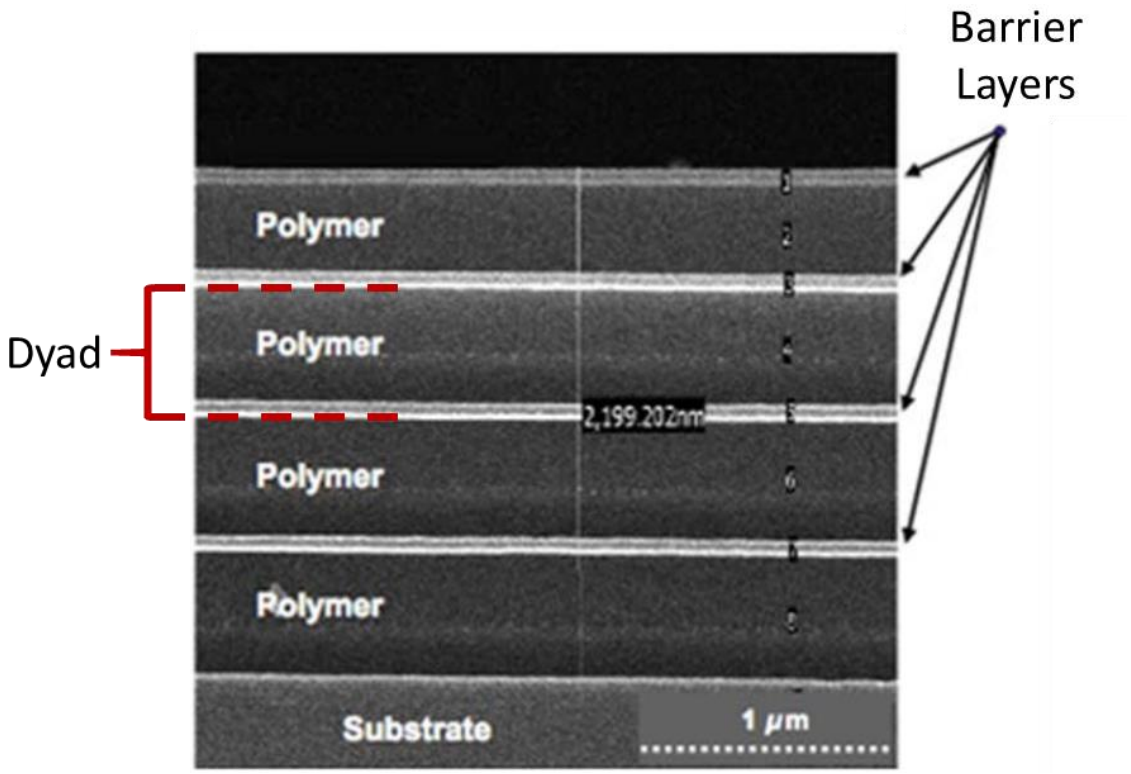

Figure 10 - SEM image of a cross-section of a multilayer structure with alternate organic and inorganic layers (Vitex Systems, Trade name: Barix®). Modified from reference.[14]

The inorganic layers used in barrier films can sometimes have the issue of corrosion due to the presence of water. Carcia *et al.* have shown that ALD Al_2O_3 on exposure to moisture can convert to its hydroxide form which is partially crystalline in nature.[18] Under such conditions, water or any other permeating species can selectively diffuse along the grain boundaries of the partially crystalline ALD Al_2O_3. Therefore, to tackle with the issue of corrosion in some of the ALD materials, nanolaminate structures can be used.[18] The schematic of the nanolaminate structures is shown in the Figure 8(c) and (d). This kind of structure utilizes the chemical stability of one layer while the permeation resistance property of the other ALD material blocks the moisture.

2.4 Mechanical Issues with ALD barrier films

As mentioned earlier, the performance of ultrathin barrier films for organic electronic devices can be severely affected by the formation of defects due to the inclusion of particles into the barrier matrix.[59, 60] To begin with, the first possible source of particle contamination is an unclean substrate surface. If not cleaned properly, the substrate may contain particles on its surface. To tackle with the issue of particle contamination on substrate surfaces, polymer coatings are used as smoothening layers over the substrates prior to the deposition of ALD layers.[22, 61] The smoothening layers of polymers cover the particle contamination such that the top surface becomes smooth while providing ideal conditions for the deposition of ALD barriers. The deposition of ALD layer on the polymer, however, results in a large magnitude of elastic mismatch due to differences in the nature of these materials. Bulusu *et al.* have shown that increasing the thickness of polymer layer results in the formation of cracks in the ALD layer due to stress concentrations around the particles and from increased crack driving forces from the elastic mismatch between the ALD layer and the polymer layer. [20] Figure 11(a) shows the schematic of barrier structure with tensile stresses in the ALD layer and cracks in the Ca sample. Therefore, using very thick smoothening layers is not a viable option. Other source of particle contamination can arise from the environmental conditions during the manufacturing processes for ALD barriers. Particles can originate from the deposition chamber, and also from the surroundings while handling and transfers. Another possible source is the use of anti-block particles. The anti-block particles are often used in commercial polymer films to prevent any adhesion between the two adjacent surfaces on a roll. Even these anti-block particles can be a significant source of particle contamination.[62] With the financial constraint of

keeping the cost of commercial products low, increasing the thickness of ALD coatings indefinitely or cleaning the fabrication facility at short intervals is not a practical solution. Also, with increase in the thickness of the ALD layers, the crack onset strain decreases which reduces its potential to be used in a flexible device.[57]

The ALD films always have a certain value of mechanical residual stresses after the deposition.[63-65] The stress concentrations in the ALD layer get enhanced around the coated particle whose magnitude is directly correlated to the magnitude of residual stress in the ALD layer. Therefore, the strategy that can be used to improve the performance of barrier films is to lower the magnitude of residual stresses in the barrier structure by using multilayers of different materials. For example, while using PECVD SiNx and SiOx in the multilayer structure, films with lower stresses were found to have better performance than those with higher stresses.[66] Bulusu *et al.* have previously shown similar results by using multilayer barrier architectures consisting of nanolaminates of ALD Al_2O_3 and HfO_2, and PECVD SiNx on polymer layer, as shown in Figure 11(b).[20] In this structure, the ALD nanolaminates had a tensile residual stress of ~550 MPa whereas the PECVD SiNx had a compressive residual stress of ~360 MPa. The opposite directions of residual stresses in both the materials lowered the magnitude of net residual stresses, thereby reducing the formation of large cracks. This strategy, however, may not work in certain cases as the conditions for reducing stress levels might not be achieved in the proximity of particles as shown in Figure 12. Particles can get incorporated into the barrier structure at different levels which can introduce highly curved regions and edges around it. In case I, the particle is on the polymer layer and is covered by both PECVD and ALD layers, whereas in case II, it is on the SiNx layer and is thus covered only by the ALD layer. In the areas which are

far from the particle, there will be a lower magnitude of residual stress due to stress compensation between PECVD and ALD layers. However, for case I, there will be areas of high stress concentrations at the curved regions and the edges of the particle. In case II, since the ALD layer is coated on the particle, high stress concentration regions are formed around the particle. Thus, the condition for stress compensation is again not satisfied. Therefore, in both of these cases, there will be the formation of high stress concentration regions around the particles due to the geometry and non-satisfactory conditions for stress compensation which can lead to the initiation of localized cracks. Figure 13 shows the optical images of cracks around the particle contamination in a barrier film with reduced levels of stresses formed by the combination of the ALD and PECVD layers. It is clearly seen in the Figure 13 that there is the formation of cracks around the particles, however, the cracks are confined around the particle defects and do not propagate over longer distances. However, these cracks still act as permeation pathways for the atmospheric gases to pass through the barrier films resulting in the localized degradation which appears as a spot in Ca samples, as shown in Figure 14. It can, therefore, be concluded that by using the hybrid structure with ALD and PECVD SiNx layers, the propagation of cracks can be avoided but not the initiation of cracks in the presence of particle defects.

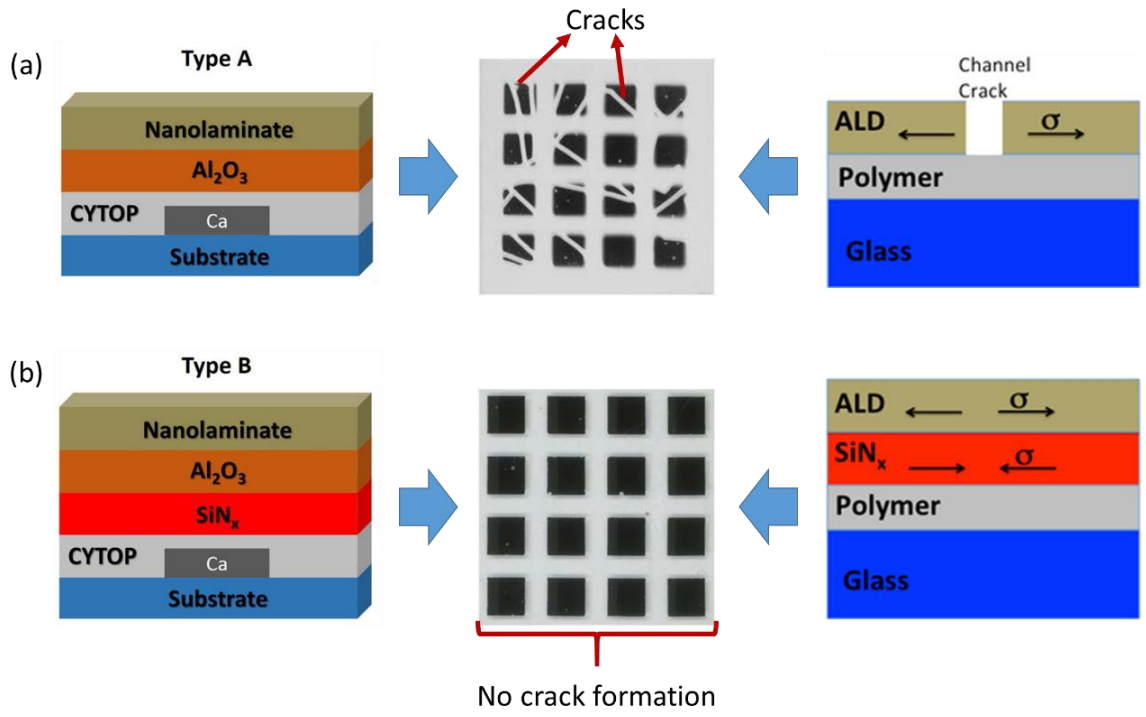

Figure 11 - (a) Type A structure with only ALD layers on polymer substrate leading to the formation of cracks due to large magnitude residual stresses. (b) Type B structure without any crack due to the compensation of tensile residual stress in ALD layer with the compressive residual stresses in SiNx layer. Modified from reference.[20]

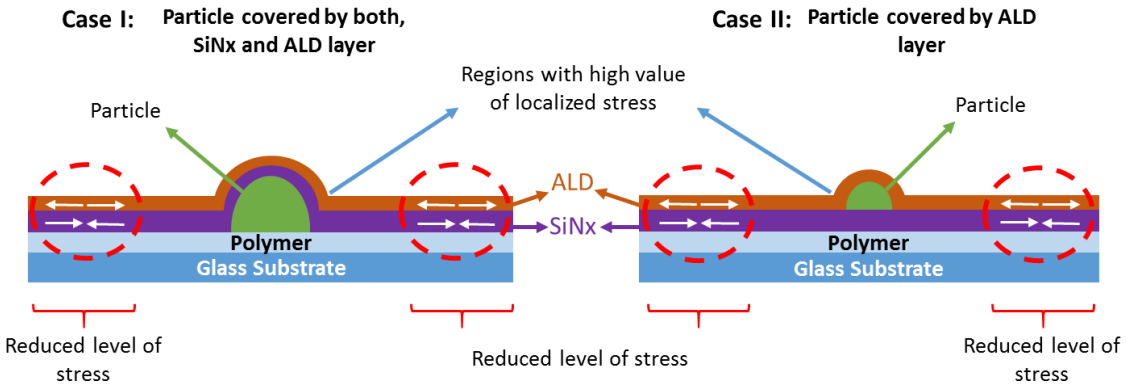

Figure 12 - Schematic of different stress regions in barrier films with particle getting incorporated in the barrier at different deposition processes.

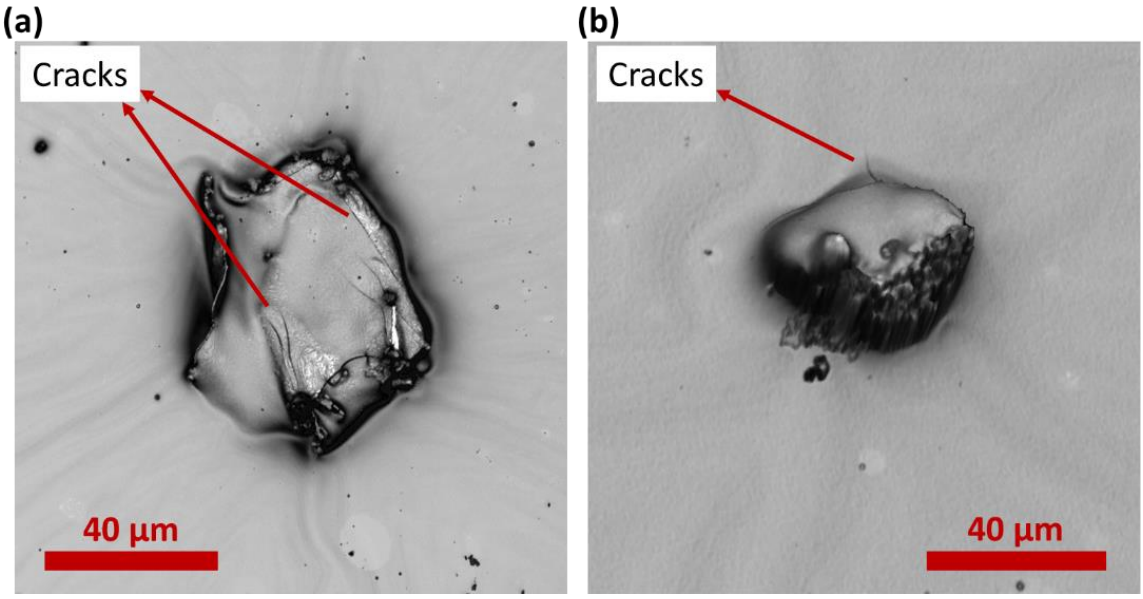

Figure 13 - Optical images of localized cracks near particles in low stress barrier structures. Structure: 4300 nm Cytop + 100 nm SiNx + 200 cyc Al_2O_3 + 20x(5 cyc Al_2O_3 + 5 cyc HfO_2).

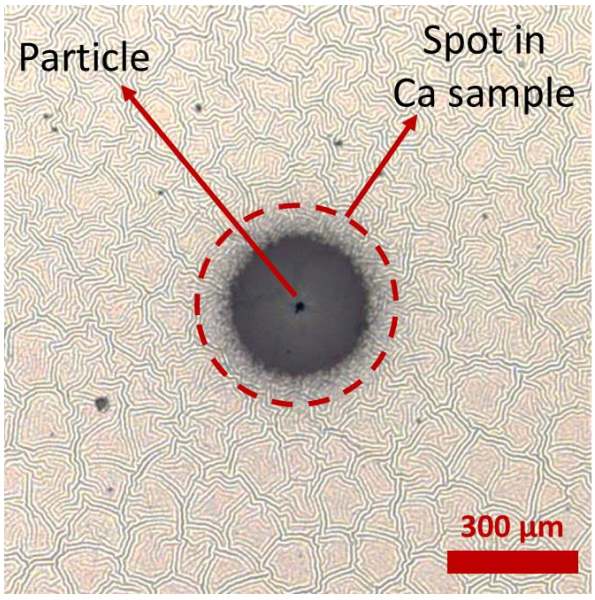

Figure 14 - Optical image of a spot in Ca sample with particle at its center.

Looking at the origins of particles and their impact on crack formation, it becomes highly significant to understand the effects of particles with different mechanical properties on the performance of barrier films. To the best of our knowledge, there has not been a study conducted primarily on the nature of particles involved in the failure of barrier films. Based on their physical and mechanical properties, each particle can have a different response to the applied strain in the barrier film. As it appears almost impossible to get rid of the particle contamination completely within the practical constraints, knowing the effect of particles with different origins can help in isolating the portions of deposition processes which need additional attention.

2.5 Corrosion

2.5.1 Corrosion of ALD Barriers in Moisture and Ionic Solutions

ALD Al_2O_3 films deposited at low temperatures have been found to be susceptible to hydration reactions and corrosion in presence of water.[39, 67, 68] Carcia *et al.* have shown that high hydrogen content in the ALD Al_2O_3 films deposited at low temperatures leads to the formation of crystalline hydroxide phases on exposure to moisture.[18] The grain boundaries, created due to formation of crystalline hydroxide phases in moisture, can allow rapid permeation of water through the barrier layer.

Besides moisture barriers, ALD films can also be used as a protective barrier in aqueous media. However, their application in aqueous environment will be subjected to their stability in water. Several studies have explored the corrosion resistant ability of ALD

films on variety of substrates in corroding media. Abdulagatov *et al.* studied corrosion protection of ALD Al_2O_3 and TiO_2 on copper in water.[39] They found that ALD Al_2O_3 dissolved in water, whereas ALD TiO_2 had nucleation difficulties which prevented it from completely covering the copper surface. The composite coating consisting of ALD Al_2O_3 as the adhesive layer with the capping layer of ALD TiO_2 was found to be most resistant to water corrosion. Bulusu *et al.* demonstrated improvement in stability of ALD Al_2O_3 films in aqueous environment with the help of metal oxide capping layers.[67] They found that the addition of thin layers of hydrolytically stable metal oxides can improve the stability of ALD Al_2O_3 films. Potts *et al.* studied corrosion protection of ALD Al_2O_3 on steel and aluminum alloys.[69] The ALD films of varying thicknesses deposited at range of temperatures were used for the study. They found that plasma enhanced ALD (PEALD) films were superior to thermal ALD deposited films with lower porosity and excellent adhesion with no delamination. These two qualities are essential for any material to be used as a barrier. Marin *et al.* [70] and Shan *et al.* [71, 72] have studied the corrosion protection of stainless steel using ALD films in separate studies where they found that thin ALD coatings were able to increase the resistance of stainless steel from electrochemical corrosion in NaCl media.

Most of these studies conducted are limited by their time based analysis. Many of these tests evaluate the film stability by monitoring the performance of the device or material they are protecting. Little is known about the corrosion kinetics of the barrier. Thus, to fully understand the chemical stability of these films, long term testing in corroding media must be performed in order to understand the failure of the protected surface at a later stage of exposure. Thus, it becomes critical to conduct chemical stability

tests for longer durations or in a manner that provides corrosion rates in order to better project the durability of these coatings in harsh environments. This demands for a different strategy to determine the corrosion protection ability of a barrier layer.

2.5.2 ALD Barriers For Biological Environments

Miniaturized medical and wearable electronic devices have recently gained significant popularity for their new treatment and monitoring capabilities, ease of application and enhanced portability. These devices include artificial pacemakers, cochlear implants, drug-eluting stents, artificial heart valves, defibrillators, and physiological monitors.[73-79] These devices are often exposed to harsh environmental conditions that are not typically experienced by electronics designed to operate in ambient air. When used as an implant or a wearable device, they are exposed to different bodily fluids with varying pH and salt concentrations, which can lead to rapid degradation of the electronics and materials used for the implant. Rigid and hermetically sealed packages are often used for implanted devices in order to prevent the exposure of the electronics to this environment. However, this prevents the utilization of soft or flexible devices which are able to more easily conform to the natural deformation of the body. Such devices require a protective coating which must also be thin and conformal in order to allow for the inherent flexibility in the device structure. For many of these cases, there is a strong need for developing reliable barrier films that can protect the electronic circuitry against the harsh biological environment. The requirements for such barrier layers include the need for them to be chemically and mechanically stable, biologically compatible, and have low permeability

to environmental stressors that could lead to the corrosion or degradation of the electronic devices. Overall in developing such barriers, the key is to allow the device to operate in the biological environment with excellent long-term retention of performance with minimal negative impact on the host biological system.[80]

When considering chemical resistance against biological media, a number of materials (e.g., urethanes, polyimides, Teflon, parylenes, silicon nitride (Si_3N_4), amorphous silicon carbide (*a*-SiC), diamond-like carbon (DLC) and silicones) have been investigated for use as barrier coatings to protecting electronic components in biological environments.[81-84] The evaluation of the barrier material stability has focused on the stability of device performance, which includes measurements of electrical leakage, resistivity, and impedance, as well as transport rates for H_2O and ionic species through the barrier and dissolution rates from infrared (IR) spectra.[83, 85] Polymer coatings such as polytetrafluoroethylene (PTFE), parylene, and silicone rubber have been explored widely due to their biocompatibility and ability to coat complex shapes. Parylene C has gained significant interest in a wide range of applications, such as neuronal probes, cardiac pacemakers, defibrillators, and other BioMEMs applications.[86] The advantages of Parylene C include USP Class VI biocompatibility as it is chemically inert, non-toxic, non-biodegradable and biocompatible.[87-91] While biocompatible, polymers generally have a limited ability to protect sensitive devices from water or ionic solution ingress due to their relatively high diffusion coefficients when compared to dense inorganic or metallic materials.[92-94]

In another approach, the ALD films can be used as a protective layer and can simultaneously be used to modify the surface properties to develop biocompatibility.[95]

Researchers have investigated a plasma-assisted ALD of Al_2O_3/parylene C bi-layer barrier coating on an interdigitated capacitive electrodes device. They demonstrated that the high impedance and low leakage currents in the Al_2O_3/parylene bi-layer are preserved at least three times longer than that of single parylene C layer barrier when tested in phosphate buffered saline solution (PBS) at 80°C.[96] Nonetheless, the corrosion or failure of low temperature deposited ALD barriers remains a concern in harsh environments. Thus, the understanding of the chemical stability of thin ALD barrier films is critical to project their long term reliability for protecting electronics in biological environments.

Another point of consideration for the encapsulation of implantable sensors and wearable devices is that the coatings should not cause any damage to the biological host when implanted or worn. Carlisle *et al.* have demonstrated the application of ALD deposited materials for making hermetic bio-inert coatings for bioimplants.[97] Finch *et al.* studied the biocompatibility of ALD alumina and ALD hydrophobic coatings on standard glass cover slips.[98] After testing ALD coated substrates in a cell culture solution for 7 days, Finch *et al.* found that ALD alumina is more biocompatible than ALD hydrophobic films. Thus, it was concluded that ALD alumina can provide several advantages like conformality and excellent dielectric properties for bio-sensors, actuators and microfluidic devices. Hyde *et al.* studied the biocompatibility of ALD aluminum nitride coatings on cellulose fiber substrates.[99] This work demonstrates the potential application of ALD coatings deposited at low temperatures for surface modification to produce biocompatible materials. In subsequent work, Hyde *et al.* used ALD Al_2O_3 to alter the surface wetting properties of unwoven polypropylene and woven cotton fabrics.[100] They demonstrated that surface wetting transitions are dependent on different processing conditions like

deposition temperature and coating thickness. All these studies strongly suggest the successful application of ALD in biological devices. Since, the stability of ALD films in different solution environments is critical to such application, there is a need to understand the chemical stability of ALD thin-films in different biological solutions.

2.6 Integration with Photovoltaic Devices

As an alternate to conventional PV technology, Perovskite solar cells (PSCs) are marked by cost-effective materials and fabrication processes.[23, 101] PSCs have shown a remarkable increase in efficiency in less than a decade. Use of perovskites in liquid-electrolyte based dye-sensitized solar cells (DSSCs) was first introduced by Kogima *et al.* in the year 2009.[23] The power conversion efficiency (PCE) of the devices were just 3.8%. The devices were extremely unstable due to the dissolution of perovskites into the organic solvent.[102] A significant improvement in the performance of devices was made by replacing the liquid electrolyte with a solid hole-transporting material (HTM), *i.e.*, spiro-MeOTAD, which also helped in improving the stability of the devices by removing the chance for dissolution of perovskites into the organic solvents.[103, 104] The most recent devices have attained an efficiency of above 20%.[105] However, the stability of PSCs is still a major issue. Studies conducted on PSCs have identified several factors affecting the stability of devices. These factors can be categorized as environmental (oxygen and moisture), thermal (high temperature and intrinsic heating) and photo-stability (light).[106-114] This work focuses on improving the stability of PSCs while protecting them from oxygen and moisture.

2.6.1 Degradation in Perovskite cells due to atmospheric gases

PSCs, to have a viable commercial application, should be able to function in open atmospheric conditions for long durations. During their application period, PSCs should not undergo any significant degradation which reduces their performance. However, even after huge improvements in the stability of PSCs in recent past, the devices are still susceptible to degradation because of oxygen and moisture from the atmosphere. This is because the materials used for the fabrication of PSCs are susceptible to oxidation and hydration. Rafael *et al.* found that, a commonly used hole transporting material (HTM), Spiro-OMETAD, undergoes photo-induced oxidation in both, air and inert atmosphere.[115] O'Mahony *et al.* probed yields and lifetimes of photo-induced, long-lived charge separation in various $MAPbI_3$-sensitized solar cells.[116] They observed a rapid and significant degradation in the yield of long-lived charge separation for coated mesoporous Al_2O_3 and bilayer systems when exposed to ambient conditions. This process was found to occur only when both, oxygen and light, were present. Therefore, they concluded it to be the result of photo-oxidation of perovskites. In presence of moisture, perovskites are easily decomposed due to the presence of hygroscopic amine salts.[106, 117] Shriayama *et al.* proposed that the degradation of $MAPbI_3$ in presence of humid air follows following mechanism.[118]

$$CH_3NH_3PbI_3 \rightarrow PbI_2 + CH_3NH_3I \text{ (or } CH_3NH_2 + HI) \quad 2.2$$

$$CH_3NH_3PbI_3 + H_2O \rightarrow PbI_2 + CH_3NH_3PbI_3.H_2O \quad 2.3$$

$$4(CH_3NH_3PbI_3) + 2H_2O \rightarrow (CH_3NH_3)_4PbI_6.2H_2O + 3PbI_2 \qquad 2.4$$

Shriayama *et al.* claimed that the reaction in Equation 2.2 leads to a decrease in volume or thickness of the layer due to formation of non-volatile PbI_2 which remains in the layer, and desorption of volatile CH_3NH_3I (or CH_3NH_2 + HI) which escapes from the structure. They also mention that reaction (2.3) and (2.4) result in increase in volume or thickness of the layer due to incorporation of water molecules into the structure with reaction (2.3) being reversible in nature.[118, 119] Christians *et al.* showed that the incorporation of H_2O leads to a loss in absorbance across the visible spectrum.[120] Thus, exposure to oxygen and moisture pose a huge problem which needs to be addressed for making PSCs a viable commercial product. PSCs, therefore, require encapsulations that can prevent photo-oxidation and hydration of the materials used for making the devices. The encapsulations will ensure long-term stability of PSCs for commercial application.

2.6.2 Encapsulation of Perovskite cells

Taking a cue from the encapsulations techniques developed for organic electronics, similar barrier architectures can be employed in case of PSCs. The barrier films can be fabricated either by direct or indirect encapsulation methods as discussed in previous sections. However, there are some concerns regarding the compatibility of methods for encapsulation of process with the PSCs. Zardetto *et al.* studied the effect of deposition of thermal and plasma ALD on perovskite material.[29] They found that perovskite materials are quite sensitive to high temperature conditions. This negates the possible use of high

temperature ALD processes for direct deposition of ALD based barrier encapsulation. They also show that perovskite materials can degrade on exposure to oxygen plasma during ALD deposition. Thus, low temperature plasma ALD can have detrimental effects on PSCs. In their study, thermal ALD has shown least effect on the perovskites and thus, can possibly be used for the deposition of ALD barriers on top of PSCs. However, long and sustained exposure of perovskites to high temperatures (~100°C) can severely affect the devices. The effect of long exposure times can be reduced by the application of spatial ALD deposition technique.[29, 49, 50, 121] Due to all these issues, the use of direct encapsulation techniques for the preparation of barrier encapsulation for PSCs seems to be a distant goal.

While using indirect encapsulation technique, barriers and devices are prepared separately. Thus, barriers can be prepared using any deposition process as it will not have any effect on the device. However, care must be taken while sandwiching the barriers and devices using an adhesive material between them. The adhesive layer must be compatible with the PSCs as they themselves could damage the devices by reacting chemically with them before even getting any effect from other external factors.

CHAPTER 3. EXPERIMENTAL METHODS

3.1 Introduction

This chapter provides the details of various experimental methods used in this dissertation. It starts with the optical Ca corrosion test used for the testing of barrier encapsulations. Detailed procedure for the calculation of intrinsic and extrinsic permeation rates is explained to determine the quality of various barrier film structures. Optical Ca tests have also been used to determine the side permeation rates in the case of indirect encapsulation. Further investigation of barrier film materials was conducted to determine their chemical stability and corrosion protection ability using ZnO photoluminescence test and electrochemical impedance spectroscopy. The concepts of these techniques have been described in detail followed by the description of the technique used for the determination of residual stresses in the ALD and PECVD SiNx films. In the last section, the procedure adopted for the determination of the efficiency of perovskite solar cells has been described.

3.2 Optical Ca corrosion test

With the development of ALD based barrier films technology, WVTRs through the barrier films in the order of 10^{-6} g/m^2/day have been achieved.[15-17] The determination of WVTRs in this order of magnitude is a big challenge as the standard techniques that are available have resolution limits that are too high to detect this rate of water vapor permeation.[122] Some of the standard methods available for determining the performance of a barrier film are isostatic methods with infrared sensor (Permatran, MOCON), isostatic

methods with coulometric sensor (Aquatran, MOCON), gravimetric cup test, mass spectroscopy, residual gas analyzer and radioactive tracing.[123-128] Besides the resolution limits and instrumentation costs, another major issue with these methods is that they can determine only the overall performance of a barrier film. These methods do not provide the information about the local factors like defects, cracks, etc., as indicated in the Figure 15, that govern the overall performance of the barrier films. Optical Ca corrosion tests, on the other hand, can give highly accurate and more detailed information.[129, 130]

Optical Ca corrosion tests are based on the fact that metallic Ca, which is opaque, reacts rapidly with oxygen and water molecules while being oxidized to its oxide and hydroxide forms which are transparent. In this technique, thin films of metallic Ca (e.g., 100 nm) are used as sensors that are encapsulated using barrier films. By determining either the opacity or transparency of metallic Ca, it is possible to determine the amount of reacting species that has permeated through the barrier encapsulation. In the Ca sample encapsulated with a barrier film, the degradation due to the permeation of atmospheric oxygen and water vapor can result in a decrease in the thickness and/or formation of spots with a decrease in the photographic area of Ca devices, as shown in Figure 16. These two aspects, Ca thickness and area, can be determined optically to calculate the amount of permeating species through different features in the barrier encapsulation. The details of the scanning methods to get the optical images of Ca samples and determining their performances are discussed in the following sections.

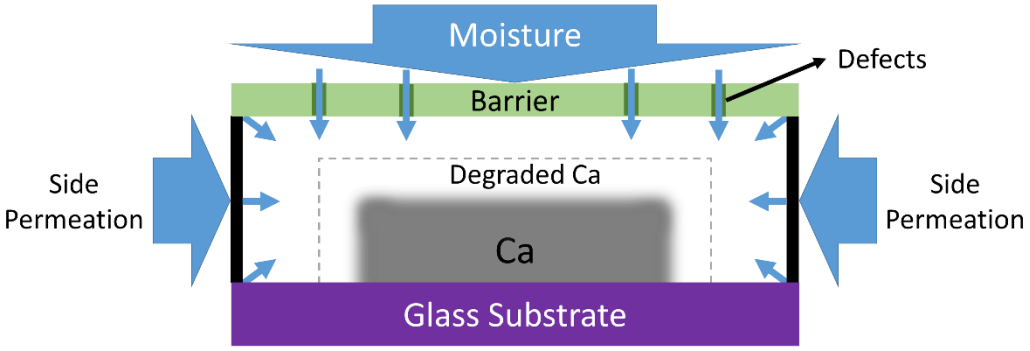

Figure 15 - Moisture ingress through different regions in the sample structure.

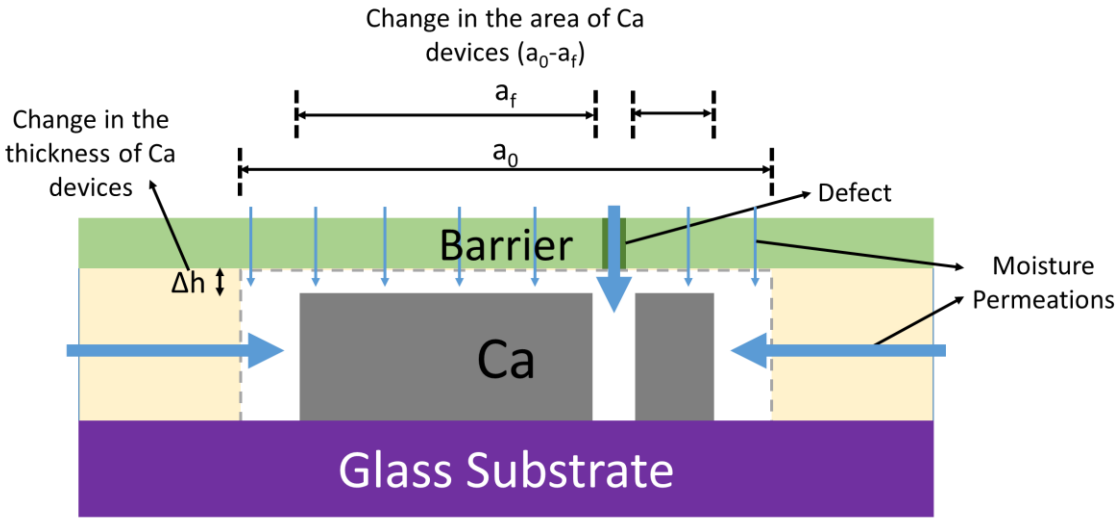

Figure 16 - Schematic of degraded Ca for calculation of water permeation rate.

3.2.1 Preparation and scanning of Ca substrates

In this dissertation, the permeation performance of barrier films were determined using optical Ca corrosion tests.[131] In this method, the Ca square sensors, with the dimensions of 5 mm x 5 mm and 100 nm thickness, were deposited on a detergent solvent cleaned glass substrate. The dimensions of the glass substrates used was 38 mm x 38 mm. Each glass substrate had 16 Ca squares as shown in Figure 17. The depositions of these Ca sensors were carried out using an EvoVac thermal evaporator (Angstrom Engineering, Inc.) connected to a nitrogen glove box. The barrier films were encapsulated on Ca substrates using either direct or indirect encapsulation methods. After encapsulation, the images of Ca samples were taken using an optical photo scanner (Epson V600), as shown in Figure 18, with the resolution of 2400 dpi.

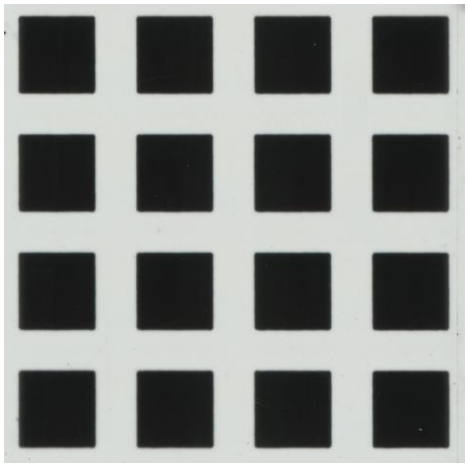

Figure 17 - Scanned image of a Ca sample.

Figure 18 - Scanner used for taking Ca images.

3.2.2 Determination of permeation rates through the barrier films

The permeation of atmospheric species through the barrier film can be divided into two categories. The permeation takes place through the regions of the barrier film free from microscale or localized defects is called intrinsic permeation. Intrinsic permeation rates depend on the barrier quality of different layers used for fabrication of a barrier film. Whereas, the permeation taking place through the defects in the barrier film is called extrinsic permeation because the factors resulting in the formation of defects are often external factors. These external factors include particle contamination and residual stresses in different layers of the barrier architecture. Using optical Ca corrosion test, it is possible to determine both the permeation rates separately as described by Kim *et al.*[131] Intrinsic

permeation results in uniform reduction in the thickness of Ca whereas extrinsic permeation results in formation of small spots in the Ca, as demonstrated in the Figure 15 and Figure 16. These two permeation rates were determined separately in this dissertation using the following methodology.

3.2.2.1 Determination of the change in thickness of Ca devices

The images of Ca samples were taken using an optical scanner, as previously mentioned. The schematic of scanning mechanism is shown in Figure 19. This figure shows that the light from the LED source first goes through the sample, gets reflected from the reflector and then passes through the sample again before being collected by the CCD. During this whole process, the light passes through various layers in the scanning setup. All the reflections and transmissions, therefore, need to be taken into consideration while determining the thickness of the Ca.

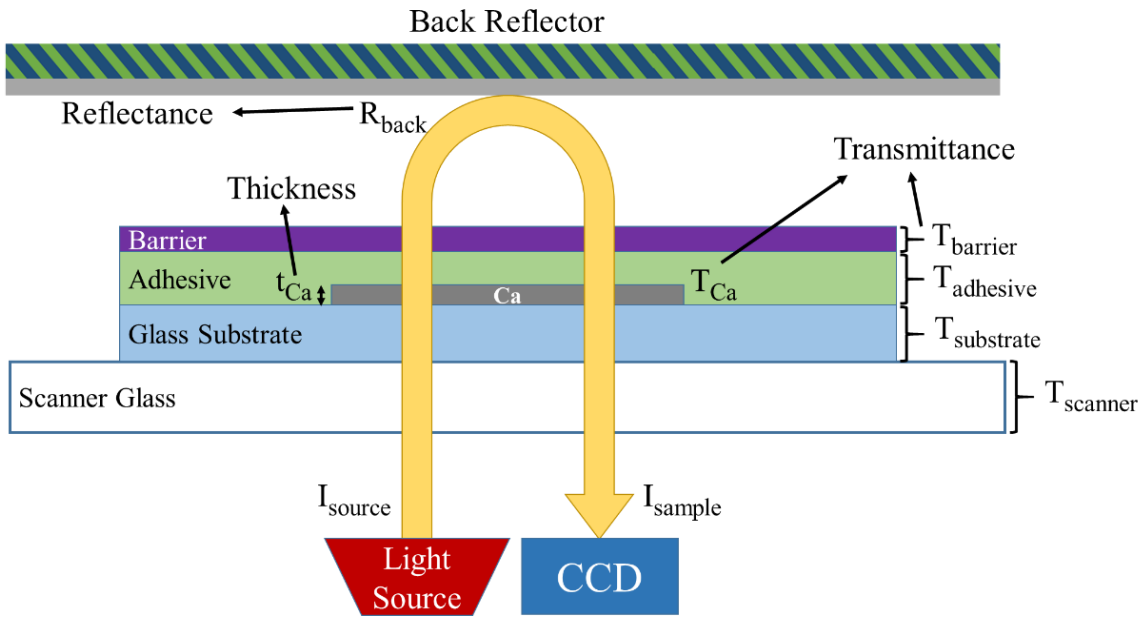

Figure 19 - Schematic of an optical scanner. Modified from reference.[131]

Using Beer-Lambert law, transmittance *T* of a material with the thickness of *t* and attenuation coefficient of μ can be written as

$$T = \frac{I_{transmitted}}{I_{incident}} = e^{-\mu t} \qquad 3.1$$

where, $I_{incident}$ and $I_{transmitted}$ are the intensities of incident and transmitted light, respectively. When this transmitted light passes through another material, it is considered as the incident light intensity and thus, final transmitted intensity is calculated again by using equation 3.1. Similarly, for reflected light, reflectance *R* can be written as

$$R = \frac{I_{reflected}}{I_{incident}} \tag{3.2}$$

where, $I_{reflected}$ is the intensity of reflected light.

While scanning Ca samples, the light from the source passes through various layers while getting reflected from the back reflector of the scanner before reaching the CCD camera, as shown in Figure 19. Two types of regions appear in the scanned images as shown in Figure 17. The regions of the sample where Ca is present appears dark whereas remaining part of the sample appears bright. Since, the only difference between the dark and bright region is the presence of Ca, the intensity of light from the bright region is considered as the background intensity and that from the Ca region is considered as the intensity after attenuation from Ca which is depends on its thickness. Therefore, using equations 3.1 and 3.2, the ratio of the intensities of light passing through the dark and bright regions is given by equation 3.3.

$$\frac{i_{dark}}{i_{bright}} = \frac{I_{source}\,(T_{scanner}T_{substrate}T_{Ca}T_{adhesive}T_{barrier})^2\,R_{back}}{I_{source}\,(T_{scanner}T_{substrate}T_{adhesive}T_{barrier})^2\,R_{back}} = T_{Ca}^2 = \left[e^{(-\mu h)}\right]^2 \tag{3.3}$$

where, I_{source} is the intensity of light source. $T_{scanner}$, $T_{substrate}$, T_{Ca}, $T_{adhesive}$ and $T_{barrier}$ are the transmittance of scanner glass, glass substrate, Ca device, adhesive and barrier, respectively. R_{back} is the reflectance of the back reflector of the scanner. μ and h are the attenuation coefficient and thickness of the Ca device, respectively. With the degradation in Ca, the thickness of Ca will change in time which will affect the transmission of light

from it. Using equation 3.3, the thickness of Ca at any instant can be determined by the ratio of intensities of dark and bright regions after initial and final scans as shown in equation 3.4.

$$h_f = h_i \frac{\left\{\ln\left(\frac{i_{bright}}{i_{dark}}\right)\right\}_f}{\left\{\ln\left(\frac{i_{bright}}{i_{dark}}\right)\right\}_i} \quad 3.4$$

where, h_i and h_f are the initial and final thicknesses of Ca device, respectively.

3.2.2.2 Calculation of intrinsic permeation rate

As shown in Figure 16, due to permeation of water through the barrier film, the thickness of Ca is reduced from h_i to h_f. Therefore, moles of Ca (m_{Ca}) oxidized is given by

$$m_{Ca} = \frac{\rho a(h_i - h_f)}{M_{Ca}} = \frac{\rho a \Delta h}{M_{Ca}} \quad 3.5$$

where, M_{Ca} is the molar mass of Ca, ρ and a are the density and area of Ca device. As mentioned earlier, metallic calcium reacts with oxygen and water vapor from the atmosphere to form oxide and hydroxides, respectively. For calculation purpose, following equation has been considered for the oxidation reaction of Ca

$$Ca + 2H_2O \rightarrow Ca(OH)_2 + H_2 \quad 3.6$$

This equation shows that 1 mole of Ca reacts with 2 moles of water. Therefore, the number of moles of water permeating through the barrier encapsulation would be twice the number of moles of degraded Ca. Therefore, the amount of water consumed while oxidation of metallic Ca is given by

$$w_{H_2O} = \frac{2\rho M_{H_2O} a \Delta h}{M_{Ca}} \quad 3.7$$

where, M_{H_2O} is the molar mass of water. Intrinsic water permeation rate per unit area is calculated by the following equation.

$$\text{Intrinsic water permeation rate} = \frac{2\rho M_{H_2O} \Delta h}{M_{Ca} \Delta t} \quad 3.8$$

where, Δt is the time of exposure of encapsulated Ca in number of days.

3.2.2.3 Determination of change in the area of Ca devices

Due to the presence of defects in the barrier film, the degradation in Ca devices is localized as shown in Figure 16 which reduces the area of Ca device. The amount of water consumed during the degradation of Ca with the change in area from a_i (initial area) to a_f (final area) is given by the following equation.

$$Amount\ of\ water\ consumed = \frac{2\rho(a_i - a_f)h_{Ca}M_{H_2O}}{M_{Ca}} \quad 3.9$$

where, h_{Ca} is the total thickness of Ca device. Extrinsic permeation rate per unit area is, therefore, calculated by the following equation.

$$Water\ permeation\ rate = \frac{2\rho(a_i - a_f)h_{Ca}M_{H_2O}}{M_{Ca}a_i\Delta t} \quad 3.10$$

where, Δt is the time of exposure of encapsulated Ca in number of days.

3.2.2.4 Calculation of average and standard deviation

Each glass substrate used for encapsulation tests contains 16 Ca devices. Each Ca device is considered separately during the data analysis and is numbered with respect to its position in the rows and columns, as represented in Figure 20. For determining the intrinsic and extrinsic permeation rates for all Ca devices in the sample, the thickness and area of individual Ca devices are normalized with respect to their initial values. The weighted average is taken to compensate for the fact that Ca devices have non-uniform degradation due to permeation through defects because of random distribution of defects and side permeation. The weighted average and standard deviation of intrinsic and extrinsic permeation rates is calculated by the following equations.

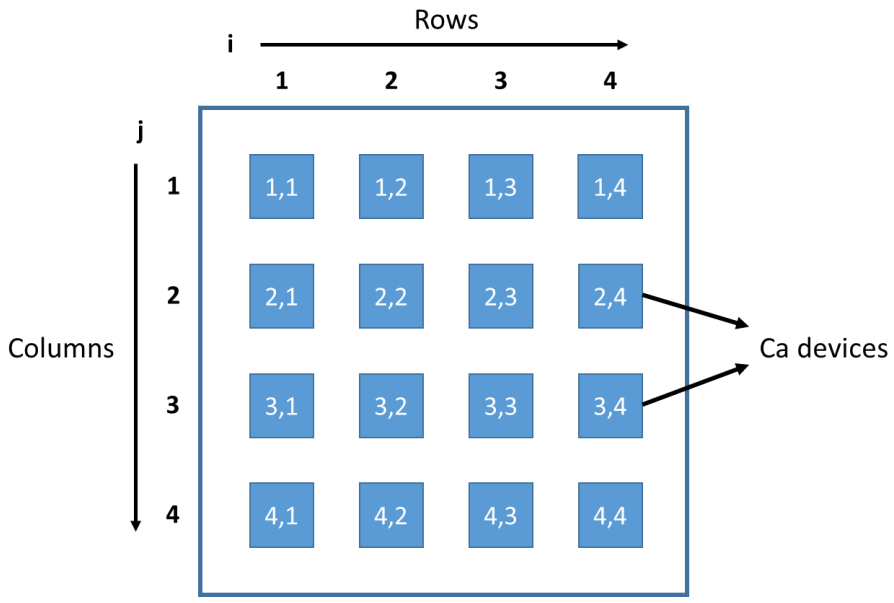

Figure 20 - Schematic of Ca devices on a glass substrate. The numbers represent the position of the Ca devices in terms of rows and columns.

$$Weighted\ Average,\ \ \bar{x}_w^m = \frac{\sum_{l=1}^{N} a_l^i x_l^m}{\sum_{l=1}^{N} a_l^0} \qquad 3.11$$

$$Weighted\ Standard\ Deviation,\ \ sd_w^m = \sqrt{\frac{\sum_{l=1}^{N} a_l^i (x_l^m - \bar{x}_w^m)^2 N'}{(N'-1)\sum_{l=1}^{N} a_l^0}} \qquad 3.12$$

where, l is the Ca device number, m is time of exposure in number of days, a_l^i is the area of l^{th} Ca device on first day, a_l^m is the area of l^{th} Ca device on m^{th} day, N is the total number of Ca devices, N' is the number of Ca devices with area $\neq 0$, and x_l^m = ratio of either the Ca area or Ca thickness on m^{th} day w.r.t that on the first day.

3.3 ZnO photoluminescence test to determine ALD corrosion

Photoluminescence spectroscopy is a non-contact technique used to probe the bandgap a of a material. In this technique, a light source is directed onto the material while a detector and spectrometer are used to determine the spectrum of the light emitted by the material. The incident photons are absorbed by the electrons in the material which get excited to higher energy states. This process of excitation is called photo-excitation. Since the higher energy state of is unstable, the excited electrons relax from the higher energy state to a lower energy state while losing the extra energy equal to the difference between the two states of transition. The energy lost during the transition process from higher energy state to lower energy state is released in the form of radiation. This phenomenon is called as photoluminescence (PL).

ZnO is a direct band gap semiconducting material which shows PL at around ~376 nm wavelength when excited by a UV light source. The electron energy band structure of ZnO with different defect states is shown in Figure 21.[132] On soaking ZnO (deposited using ALD) in water, it gets completely dissolved in less than 24 hours, and therefore, it does not show any PL. Using this phenomenon, ALD ZnO has earlier been used as a sensor to determine the chemical stability of various ALD films in water by coating ZnO with various ALD materials.[67] The same concept has been used in this dissertation to determine the chemical stability of ALD films in several other chemical environments like saline and acidic solutions which is discussed in later sections.

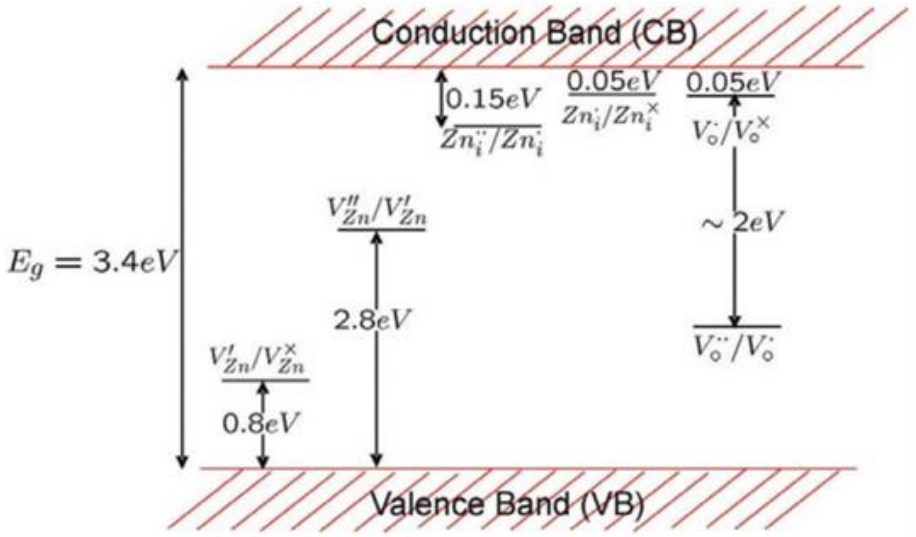

Figure 21 - Band structure of ZnO.[132]

In this dissertation, to determine the stability of ALD films in ionic solutions, ALD ZnO was used as a sensor material. It was coated with different ALD materials and soaked in various solutions while monitoring PL from the ALD ZnO layer in the sample at regular intervals. Absence of PL at any moment indicates that the barrier coating has deteriorated and degradation of the ALD ZnO layer has taken place. The PL from ALD ZnO was captured using Horiba Jobin Yvon HR800 Raman Spectrometer with a liquid nitrogen cooled backside illuminated charge-coupled device (CCD) detector. A 325 nm Helium-Cadmium (He-Cd) laser, with the laser power of 3.2 mW, was used as the excitation source. The spot size of the laser was about 3 µm. The laser light was focused on the ZnO sample and the PL was collected using the same 40x UV achromatic objective (LMU-40x, Optics for Research), as shown in Figure 22. The ALD coated ZnO samples were exposed to different solutions and PL measurements were taken at regular intervals as shown in Figure 23.

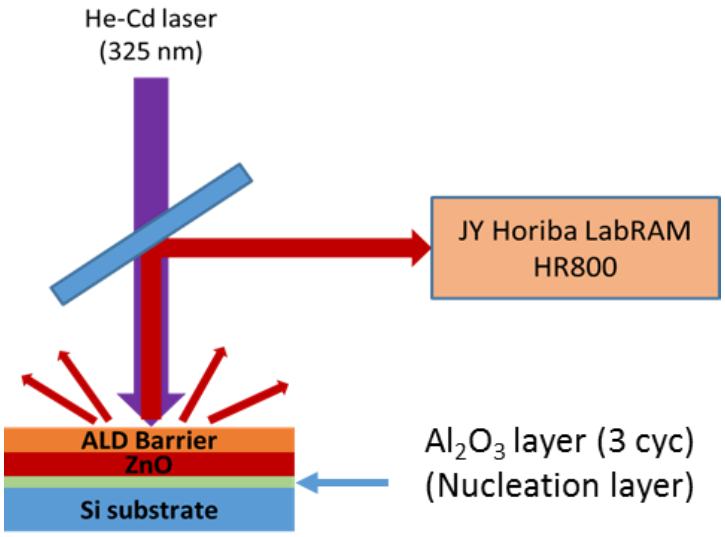

Figure 22 - Schematic of excitation of ZnO samples using 325 nm laser source and collection of PL emissions using Horiba JY LabRAM HR800 Raman Spectrometer.

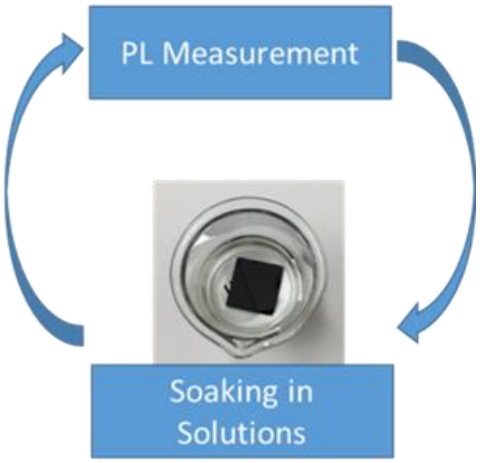

Figure 23 - Exposure of ZnO samples to different solutions.

3.4 Electrochemical impedance spectroscopy to determine the corrosion of ALD barriers

Electrochemical Impedance spectroscopy (EIS) is a powerful technique for investigating the electrochemical and corrosion response of materials and coatings.[133-135] In this technique, the impedance from the samples is measured across a large band of frequencies while applying a small magnitude of perturbation voltage. The small magnitude of applied voltage is to ensure that any response or relaxation process in the sample material follows a linear relationship with the applied voltage in a large frequency range. Thus, it is a steady-state technique that can assess relaxation phenomena for different processes whose relaxation times vary over several orders of magnitude of frequency. Equivalent circuits, used to fit the experimental data, enable us to interpret respective contribution from individual processes happening in the system.[136-139] Every element in the equivalent circuit corresponds to a physical phenomenon taking place at the interface or within the material under test. Changes in the value of respective circuit elements signifies a certain process during corrosion. Data using this technique can be collected at different time intervals to monitor changes in the system with time. Thus, EIS is a technique that provides time dependent quantitative information about the electrode processes. Information like stability of the films, formation of pores, etc., can be determined using EIS.

3.4.1 EIS setup

In this dissertation, EIS has been used for the determination of stability and corrosion protection of various ALD metal oxides in different ionic and biological solutions using a Reference 600^{TM} potentiostat from Gamry Instruments. The EIS measurements were conducted in a custom made cell with three-electrode configuration as shown in Figure 24(a). The custom-made cell can incorporate a maximum of 5 samples at the same time as opposed to just one sample in case of standard cells. Ag/AgCl electrode was used as the reference electrode and a graphite rod was used as the counter electrode. The working electrodes were prepared by depositing 10 nm Cr followed by 50 nm Au on glass substrates using E-beam evaporator (Denton, Explorer 14) with the deposition rate of 0.5 Å/s for both. The pattern of working electrodes deposited on glass substrates is shown in Figure 25. The electrical contacts to the working electrodes were made from the top while the square region of the electrode was covered with the solution, as shown in Figure 25(a). A thin layer of Ti metal with the thickness of 2 nm was deposited on top of Au using E-beam evaporator with the deposition rate of 0.5 Å/s. This Ti layer was oxidized to TiO_2 using oxygen plasma of 300 W for 200 s to form TiO_2 which acts as a nucleation layer for ALD depositions on Au electrode. The cross-section of the electrode structure is shown in Figure 25(b).

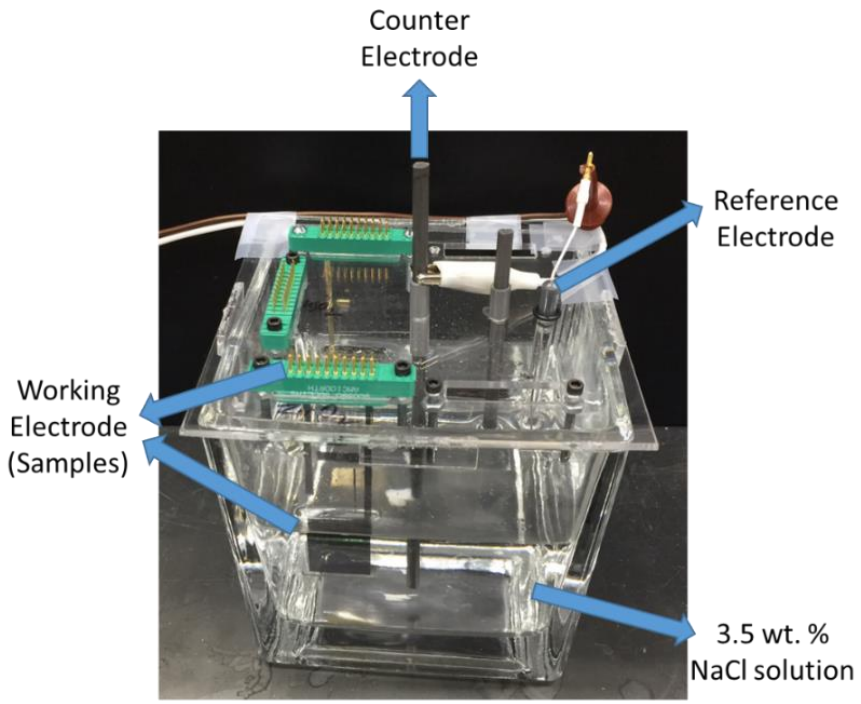

Figure 24 - Setup for EIS measurements.

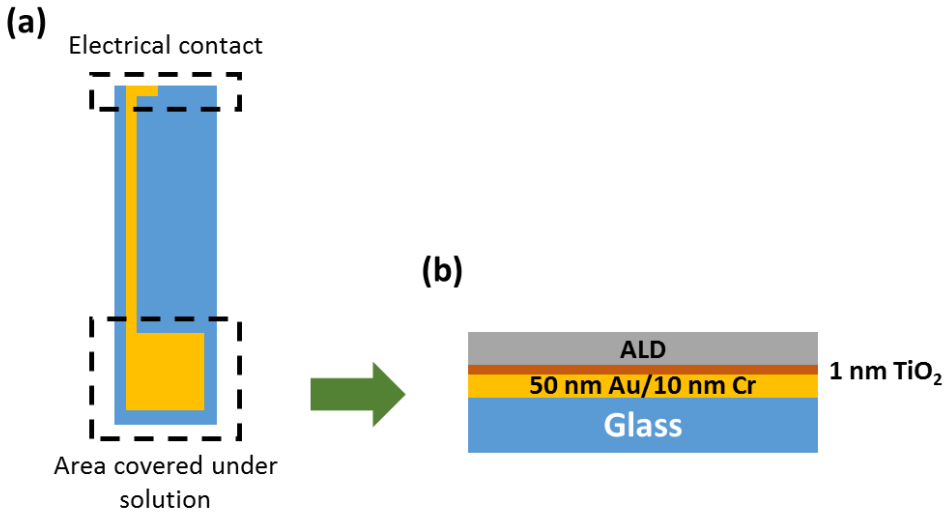

Figure 25 - The schematic of electrode design. (a) Pattern of Au electrode deposited on glass substrate. (b) Cross-section of the electrode showing different layers of glass substrate, electrode material and ALD coating.

3.4.2 Comparison of positions in EIS cell

There are 5 different positions in the customized cell where electrodes can be mounted simultaneously while using the same solution, as shown in Figure 24. To determine the differences in the impedance response of a working electrode with change in mounting positions, multiple measurements were taken at all 5 slot positions in the cell. For this purpose, 100 cycles of ALD Al_2O_3 deposited on Au electrodes at 100°C was used as the working electrode. Impedance measurements were carried out in 3.5 wt. % NaCl solution in the frequency range from 10^{-1} Hz to 10^5 Hz. Nyquist and bode plots for this sample are shown in Figure 26. It can be observed from the plots in Figure 26 that there is no significant difference between the responses of ALD Al_2O_3 with change in position. This shows that all the positions of the EIS cell can be considered to be equivalent. This confirms that the EIS measurements can be taken for a working electrode from any of the 5 positions. However, once a working electrode was placed in the cell, it was never moved from its position until the testing period is over. The solutions used for testing were replaced and refilled at regular intervals to maintain consistency with their concentration and quantity. These things made sure that any change in the impedance response will be the result of changes in the sample material only.

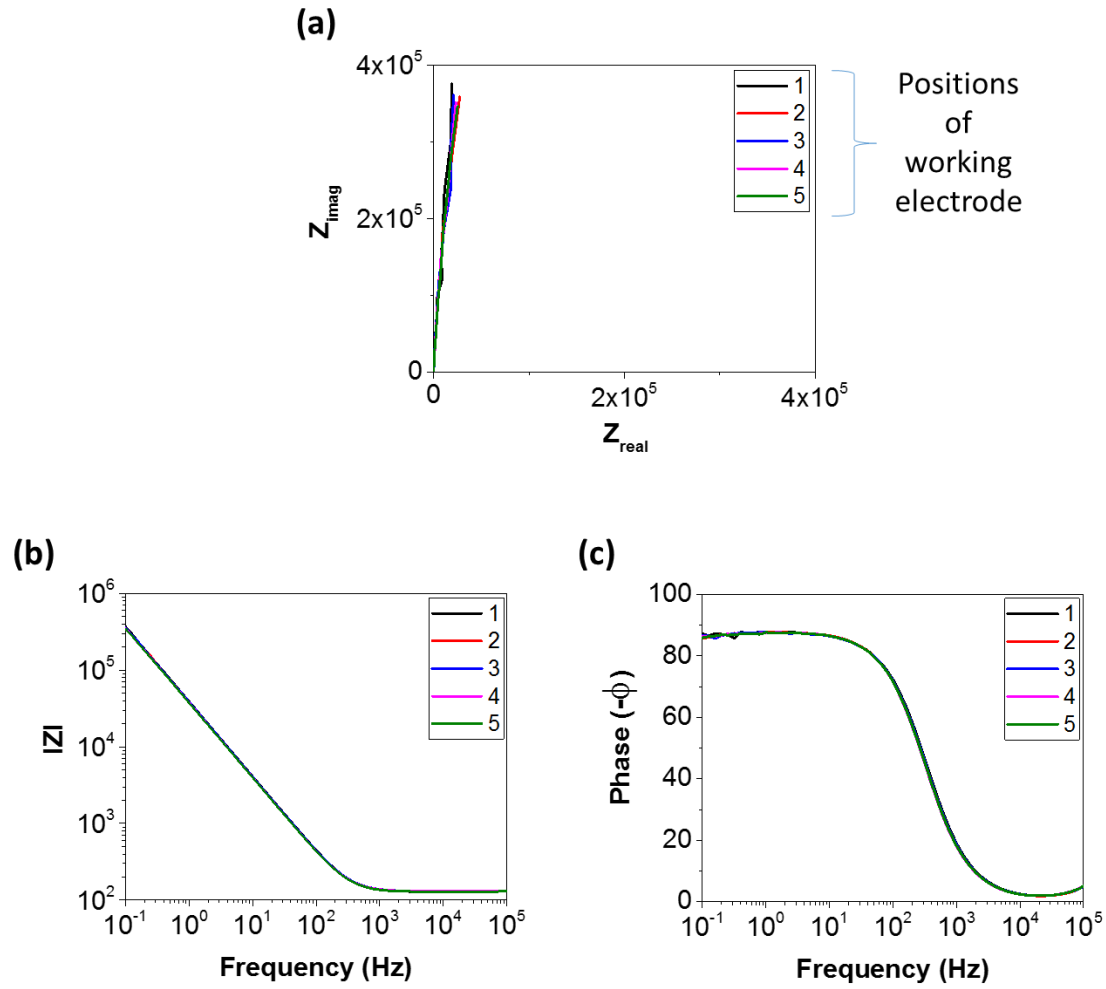

Figure 26 - Nyquist and Bode plots of Al_2O_3 in 3.5 wt. % NaCl solution at different positions in the EIS cell.

3.4.3 Impedance measurement and equivalent circuits

For the films to be viable barriers in ionic and biological solutions, they must be chemically stable in harsh environment conditions consisting of variety of species and ions present in the solutions. The ALD films were deposited on Au electrodes and exposed to different solutions forming a capacitive system. The degradation in ALD films is monitored

by change in impedance response of this capacitive system. The impedance response from such a system depends on several factors which dominate in different frequency regimes. Depending on the frequency range, the impedance is dominated either by the properties of the ALD material or on external circuit including the testing solution. On exposure to different solutions, the degradation of ALD films can occur in several steps which is evident from different impedance responses with time. Therefore, equivalent electrical circuits were used to fit the experimental EIS data to understand the nature of degradation. The equivalent circuits, used to explain the experimental data for this study are shown in Figure 27.

Circuit #1, as shown in Figure 27(a), represents the impedance response from a perfectly deposited film that is free from pinholes and defects. Constant phase element (CPE) in the circuit indicates non-ideal capacitive behavior of the ALD material which could be the result of non-uniformity in the surface of the deposited film resulting from surface roughness and variation in thickness. This circuit also fits the impedance response from a bare electrode. Circuit #2, as shown in Figure 27(b), has an additional capacitance 'C1' as compared to circuit #1 which represents the presence of pin-hole like defects in the ALD film.[140] Along with pinholes, if the film consists of regions with variable thickness, then the impedance response from such a system is represented by circuit #3, as shown in Figure 27(c), which is formed by the addition of two equivalent circuits represented by circuit #2. The variation in thickness of the film can result from non-uniform degradation due to inhomogeneity of the ALD film. Figure 27(d) shows the fitting of experimental data for HfO_2 in sea water with different circuit models. Circuit #1 fits the data for bare electrode (black), circuit #2 fits HfO_2 on first day (red) and circuit #3 fits HfO_2 on 21st day (green).

It is clear from these curve fits that the equivalent circuits used fit well at different stages of the sample.

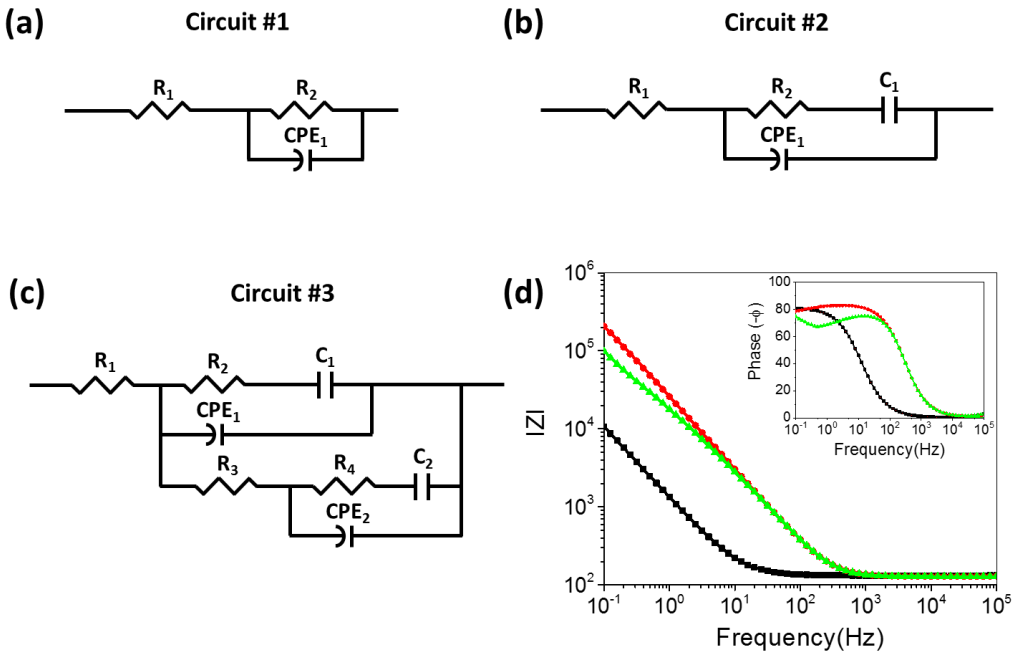

Figure 27 - Equivalent circuits used to explain the data (a) Circuit #1, (b) Circuit #2, (c) Circuit #3. R_1, R_2, R_3 and R_4 represent resistances, C_1 and C_2 represent capacitors, and CPE_1 and CPE_2 represent constant phase elements in the equivalent circuits. (d) Fitting of EIS data with different circuit models. The dots represent experimental data and solid lines represent fitted data using corresponding equivalent circuit for ZrO_2 in sea water. Color code: bare electrode (black), ZrO_2 on 1st day (red) and ZrO_2 on 21st day (green) in sea water.

In this dissertation, the EIS measurements were taken for 4 ALD materials in different solutions using the procedure described above. For current system, the resistance of solution dominates the impedance response at higher frequency ranges whereas properties of the ALD material dominate the impedance response in lower frequency

ranges. Thus, any change in lower frequency range can be directly correlated to the change in properties, and therefore, the stability of ALD material.

3.5 Residual Stress Measurement

ALD and PECVD films have residual stresses as a result of the deposition process.[63, 65, 141-144] Studies have shown that the performance of ultrathin barrier films can significantly get affected by the magnitude of residual stresses.[20, 145] Minimizing overall stress in the barrier structures have proved to be beneficial for improved performance. High value of cracks can result in the formation of cracks leading to high permeation rates for atmospheric gases. This calls for the determination of residual stresses in ALD and PECVD deposited films. It this study, wafer curvature method has been used which is based on Stoney equation.[146-148] The ALD and PECVD films were deposited on 4 inch Si wafers for stress measurement. The thickness of the deposited films (<150 nm) were much smaller than the thickness of Si wafer (~0.5 mm). The residual stress of the films were calculated using the following equation

$$\sigma_f = -\frac{1}{6}\frac{E_s}{(1-\vartheta)}\frac{t_s^2}{t_f^2}\left(\frac{1}{R_1}-\frac{1}{R_0}\right) \qquad 3.13$$

where, E_s is Young's modulus and ϑ is the Poisson's ratio of the substrate. t_s and t_f are the thicknesses of the substrate and deposited film, respectively. R_0 and R_1 are the radii of curvatures of the substrate before and after deposition of thin films, respectively. The radii of curvatures were measured using BowOptic 208.

3.6 Efficiency measurement of perovskite solar cells

To study the applicability of barrier encapsulations for improving the lifetime of perovskite solar cells, $MAPBI_3$ based perovskite cells (PSCs) were used. These cells were obtained from Dr. Joseph Berry's group at National Renewable Energy Laboratory (NREL). The structure of the devices used for encapsulation is shown in Figure 28. PSCs are unstable in open atmospheric conditions which limits their practical application. Therefore, to improve their lifetime and stability, hybrid barrier films were encapsulated on them using indirect encapsulation method. For determining the effectiveness of the barrier encapsulations for PSCs, the power conversion efficiency (PCE), η, of the PSCs were monitored with time while storing them in open atmospheric conditions. The PCE of a solar cells is calculated using various parameters extracted from the current density (J) vs. voltage (V) curves, as shown in Figure 29. The parameters that are extracted from the JV curves include short-circuit current density (J_{SC}), open-circuit voltage (V_{OC}), fill-factor (FF), current density at maximum power point (J_{max}), and voltage at maximum power point (V_{max}). FF is calculated using the following equation.

$$FF = \frac{V_{max} \cdot J_{max}}{V_{OC} \cdot J_{SC}} \tag{3.14}$$

The PCE of the solar cell is, therefore, expressed by the following equation.

$$\eta = \frac{V_{OC} \cdot J_{SC} \cdot FF}{P_{in}} \tag{3.15}$$

where, P_{in} is the power of incident radiation.

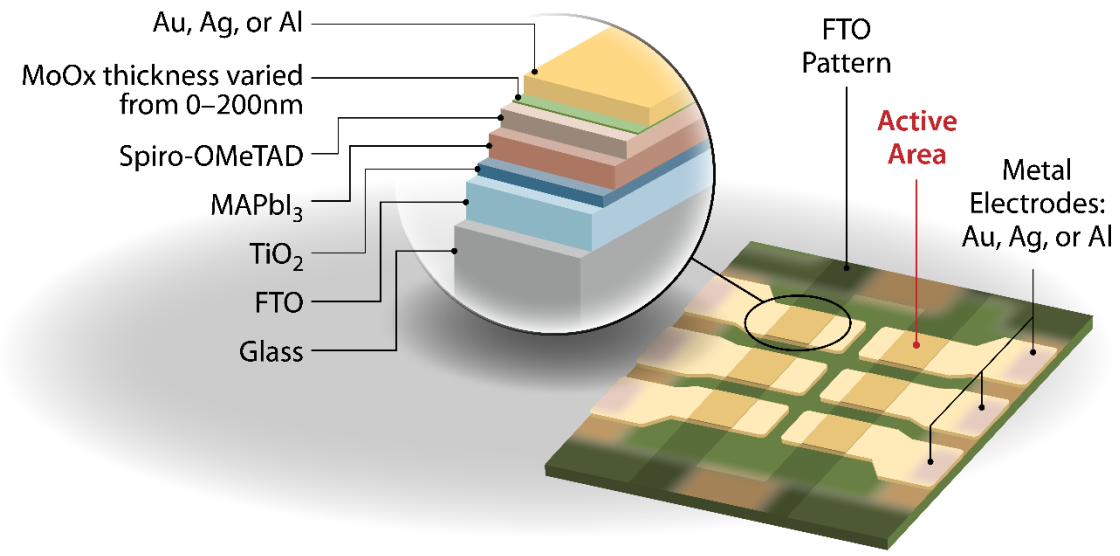

Figure 28 - Structure of the perovskite cells used in this study (Obtained from Dr. Joseph Berry's group, NREL).

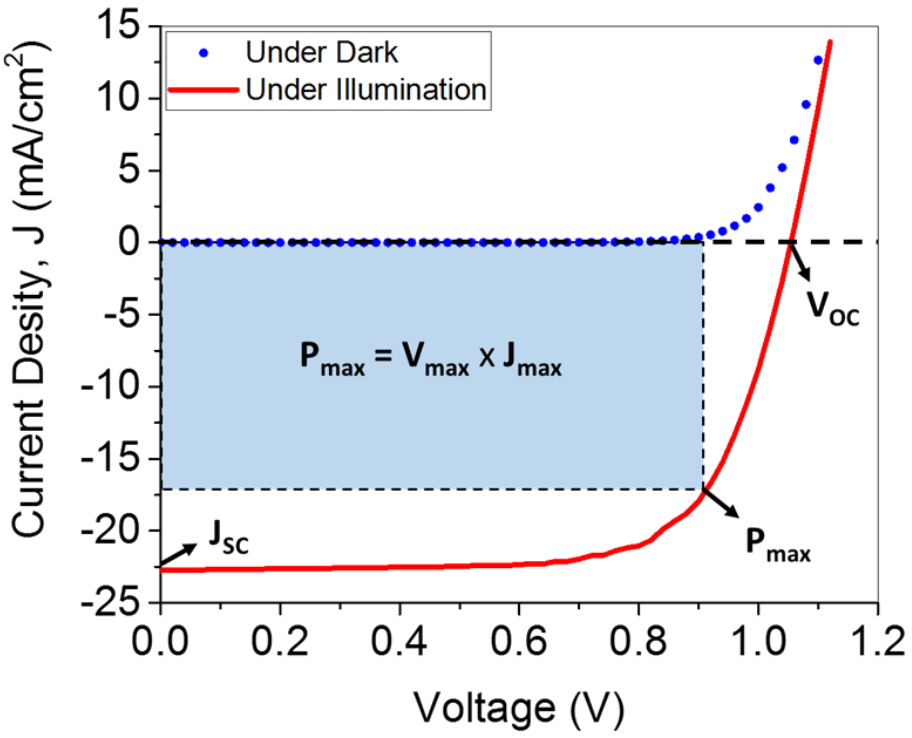

Figure 29 - A typical JV curve for a perovskite solar cell demonstrating the performance of the cells under dark and illumination conditions.

CHAPTER 4. TOWARDS PARTICLE DEFECT TOLERANT ULTRABARRIER FILMS

4.1 Introduction

This chapter deals with the issue of particle contamination in barrier encapsulation for organic electronic devices and the question of whether it is possible to create ultrabarrier films that are tolerant of particle defects. The overall performance of an ultrathin barrier film is governed mainly by the external factors like contamination and defects. The most significant cause for the contamination in the barrier encapsulations are the particles that get incorporated into the barrier structures from variety of sources like an unclean environment, unclean substrate surfaces, and even anti-block particles.

Although most of the studies conducted in the related areas have concentrated mostly on the intrinsic permeation rates of the barrier encapsulations. Some studies have focused on the effect of particle contamination in the barrier films, but there has not been a study conducted primarily on the nature of particles involved in the failure of barrier films.[20, 131, 149] As it appears almost impossible to get rid of the particle contamination completely within practical constraints, knowing the effect of particles with different origins can help in isolating the portions of the deposition processes which need additional attention. In addition, if the interaction between the particles and barriers are better understood, it may be possible to better engineer a defect tolerant barrier film.

To better understand how to create a pathway towards particle defect tolerant barrier films, this chapter first concentrates specifically on the nature of particle

contamination which results in the formation of defects. Using two types of particles, polymer (soft) and inorganic (hard), with huge differences in their mechanical properties, the effect of nature of particle on the performance of barrier film was determined using Ca corrosion test. Since the incorporation of particle contamination often leads to the formation of cracks under intrinsic stresses, mechanical tests were conducted with particle contamination in the ALD layer to determine properties such as crack growth rates and onset crack strains for each type of particle. After determining the impact of the type of particle on crack formation, issues of crack healing and the architecture of the barrier film that may lead to particle defect tolerance are covered.

4.2 Experimental methods and modeling

4.2.1 Thin-film deposition

In this study, ALD Al_2O_3 and PECVD SiNx films were deposited on polyethylene naphthalate (PEN) substrates using a Cambridge Nanotech Plasma ALD system and a Unaxis PECVD tool, respectively. The PEN substrates (Teonex, Q65HA) were obtained from DuPont Teijin Films. For the deposition of ALD Al_2O_3, tri-methyl aluminum (TMA) and oxygen were used as precursors with a plasma power of 300W at 100°C. The flow rates of the precursors were 20 sccm, and Ar was used as the carrier gas with the flow rate of 200 sccm. PECVD SiNx films were deposited at a temperature of 110°C, pressure of 1 Torr and 20 W RF plasma power. The precursor flow rates used were 200 sccm for 5% silane (SiH_4) in He and 14 sccm for ammonia (NH_3). The thickness of the films were

measured using a Wollam M2000 ellipsometer after depositing the ALD and PECVD layers on Si substrates.

4.2.2 Ca corrosion test

Ca corrosion tests were conducted to determine the effect of particle inclusions on the performance of barrier films. Two kinds of particles were used for inclusions in the barrier films, alumina and polymer (poly(styrene-b-methyl methacrylate)), representing particles having different mechanical properties. For Ca corrosion tests, samples were prepared using indirect encapsulation method. For the preparation of barrier films with particle inclusions, the particles suspended in isopropyl alcohol (IPA) were spin coated on PEN substrates followed by the deposition of 100 cycles (12.69 nm) of ALD Al_2O_3 at 100°C. The Ca substrates were prepared by depositing 100 nm of Ca in a 4 x 4 matrix with the dimensions of 5 mm x 5 mm on a glass substrate using a Spectros thermal evaporation system (Kurt J. Lesker). The Ca substrates were then encapsulated with the barrier films containing particle inclusions, as shown in Figure 30, using a double-sided UV-curable barrier adhesive (Tesa tape) in a glove box. After encapsulation, the Ca samples were exposed to a controlled environment of 60°C/90% RH in a Cincinnati Subzero Micro-Climate System. The images of the Ca samples were taken at regular intervals by scanning them using an optical scanner with the resolution of 2400 dpi. These images were analyzed using the procedure described in the section 3.2.[131]

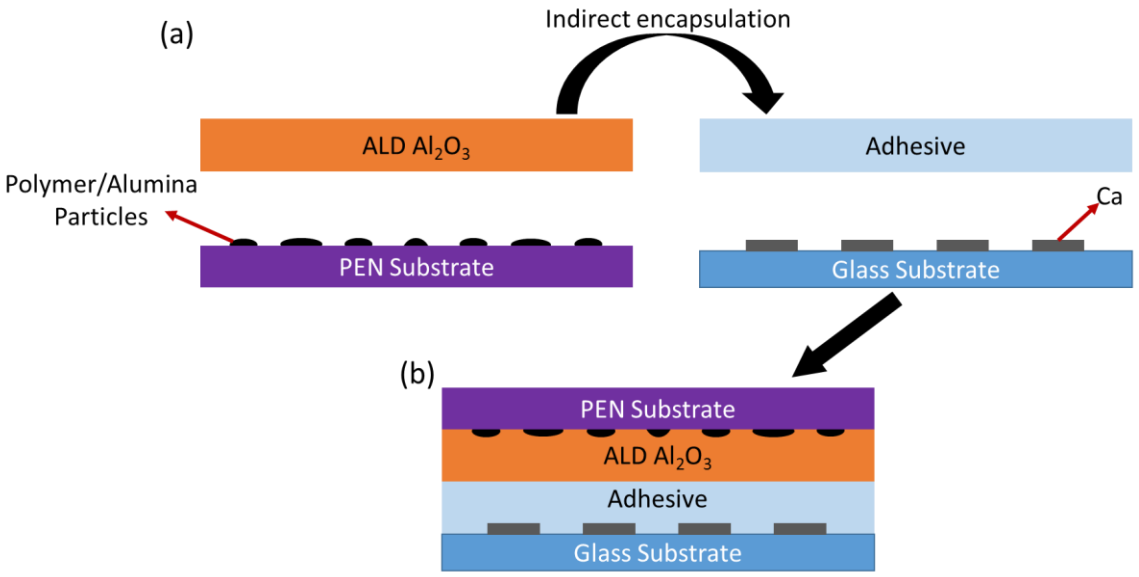

Figure 30 - (a) Schematic demonstrating the inclusion of particles followed by the deposition of ALD and PECVD layers on PEN substrate. This barrier is used for the indirect encapsulation of glass substrate with Ca devices using a double sided adhesive. (b) Final structure of the samples having particle inclusions.

4.2.3 In situ optical microscopy tensile tests

For tensile stress testing, the PEN substrates were laser-cut into rectangular strips with the dimensions of 5 mm x 50 mm. Both types of particles, alumina and polymer were dispersed on the surface of these strips using their suspensions in IPA. The ALD Al_2O_3 films with 50 nm thickness were deposited on PEN strips with and without particles on their surface. The residual stress in the ALD Al_2O_3 film was determined by the wafer curvature method using a BowOptic Stress measurement tool.

Tensile tests were conducted on the samples to determine their critical onset strain. Tensile strains were applied on the PEN strips using a microtensile testing stage (Linkam Scientific Instruments, TST350) which has the displacement resolution of 10 µm, as shown

in Figure 31. The cracks formed in the ALD Al_2O_3 layer were observed in situ using a confocal microscope (Olympus LEXT, OLS4100). Tests were performed in open air laboratory conditions. The samples were stretched by continuously increasing the applied strain at the rate of 0.05 %/s, and the value of strain at which the first crack appeared was considered as the crack onset strain, ε_c.

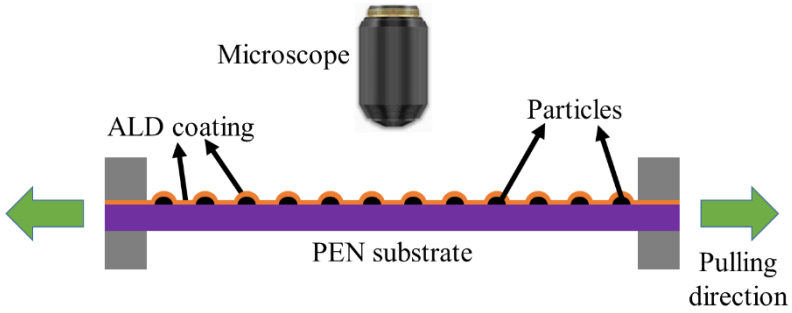

Figure 31 - Schematic for tensile testing showing that the particles are embedded in the ALD layer while tensile strain is being applied in the horizontal direction. Formation of cracks on the surface of the strip is monitored using a microscope.

4.2.4 Driving force for crack propagation

Cracking in thin films can be the result of either the residual stress or applied external load.[57, 150, 151] The strain energy release rate 'G' or driving force for crack propagation is used to determine the potential for the growth of cracks. The strain energy release rate becomes independent of the crack length once the crack is long enough with respect to the thickness of the film.[152] The driving force becomes a function of film thickness and its amplitude is governed by the constraint effect of substrate beneath the

film on the elastic energy in a volume of material around the crack.[153] Therefore, the strain energy release rate becomes a function of elastic mismatch between the film and the substrate which is given by [153]

$$G_{ss} = \frac{Z\sigma^2 h_f}{E_f^*} = \frac{Z\left(\sigma_{appl} + \sigma_{res}\right)^2 h_f}{E_f^*} = ZE_f^*\left(\epsilon_{appl} + \epsilon_{res}\right)^2 h_f \qquad 4.1$$

where σ, σ_{appl} and σ_{res} are the total, applied and residual stresses in the film, respectively. ϵ_{appl} and ϵ_{res} are the applied and residual strains in the film. E_f^* and h_f are the plane strain elastic modulus and thickness of the film. Z is the dimensionless strain energy release rate which depends on the elastic mismatch α between the film and substrate.[154]

$$\alpha = \frac{E_f^* - E_s^*}{E_f^* + E_s^*} \qquad 4.2$$

where E_s^* is the plane strain substrate elastic modulus. The Z value can be obtained using numerical models as a function of α.[154-156] Equation 4.1 assumes linear elastic behavior of both the film and substrate, and dictates the driving force for channel cracking of an isolated crack on a semi-infinite substrate.[153] The stress intensity factor 'K' for the crack can be calculated further using the following equation.[157]

$$K = \sqrt{G_{ss} E_f^*} \qquad 4.3$$

4.2.5 Simulation Model

The strain energy release rate for a crack around a particle was evaluated using finite element modeling (Abaqus). As the magnitude of the applied strain was quite small (1%), linear elastic models for ALD Al_2O_3, PEN and particle were adopted. Figure 32 shows schematic of the finite element model used for evaluating the steady state strain energy release rate 'G_{ss}' of a channel crack in the ALD Al_2O_3 layer on PEN substrate. In this model, the ALD Al_2O_3 film with the thickness of 50 nm is perfectly bonded to a 2 μm thick PEN substrate. The in-plane dimensions for the ALD film and PEN substrate are 5 μm x 5 μm. Due to symmetry, only half of the width (2.5 μm) was considered while modeling. The tensile residual stress in ALD Al_2O_3 film with the value of 548 MPa was also taken into account. A seam line representing the crack was assigned in the lower part of particle, along the thickness of the ALD Al_2O_3 layer. The thickness of the crack was the same as that of the ALD film and its length was equal to the outer diameter of the particle. The crack passes through the diameter of the particle and perpendicular to the applied strain. A displacement controlled load was imposed on the system and the strain energy release rate 'G_{ss}' was evaluated using the J-integral approach.[158] A very fine mesh was used in the regions near the particle to get accurate values of G_{ss}.

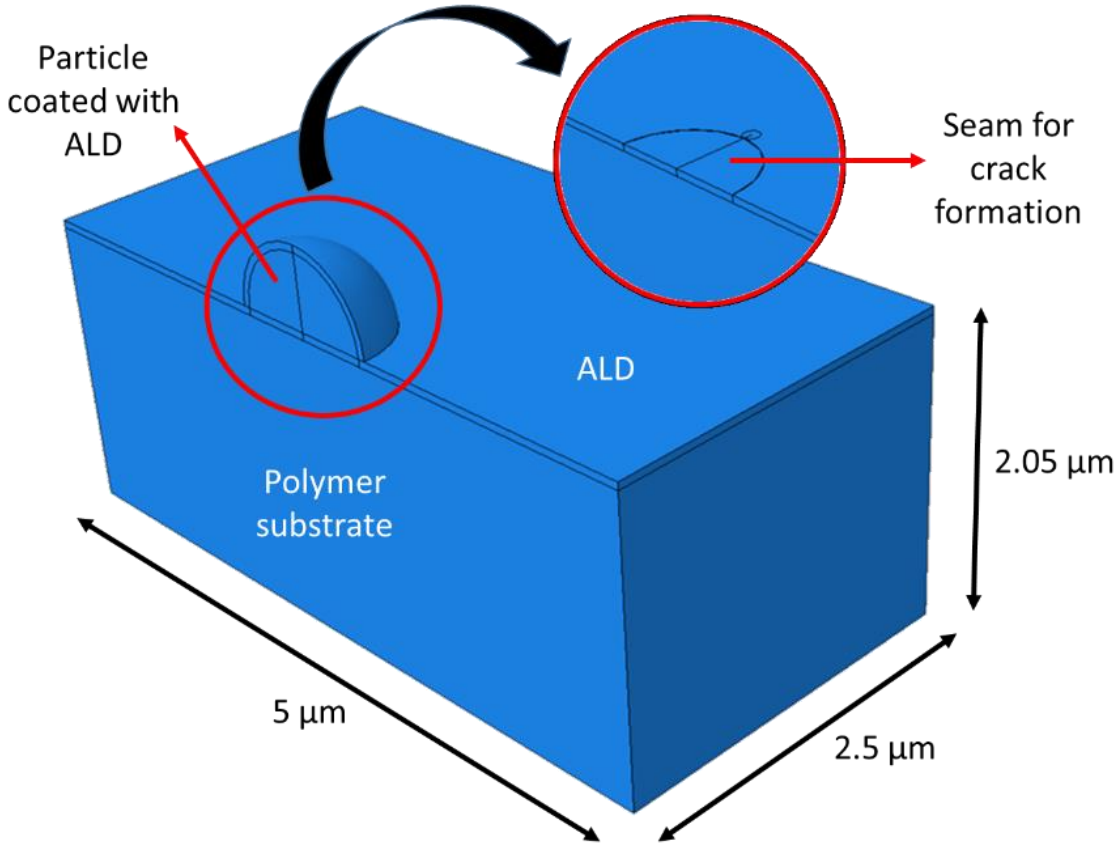

Figure 32 - Structure and dimensions of the sample used for FEM modeling. Inset in the figure shows assignment of seam for crack formation located at the lower portion of particle.

4.2.6 Barrier film architectures for crack healing test.

Four different barrier film architectures were tested to determine the healing effect of PECVD SiNx on the cracks generated in the ALD Al_2O_3 layer, as shown in Figure 33. As shown in Figure 33(a), barrier HE-1 was prepared by depositing 12 nm of ALD Al_2O_3 on a PEN substrate. Barrier HE-2 was prepared by bending the ALD Al_2O_3 coated PEN substrate over a cylinder of 6.25 mm diameter which resulted in the application of 2% tensile strain in the ALD layer, as shown in Figure 33(b). The barrier HE-2 with cracks

formed in the ALD Al_2O_3 layer due to the application of 2% tensile strain while bending is represented in Figure 33(c). Barriers HE-3 and HE-4 were prepared by depositing 50 nm PECVD SiNx on the PEN substrate and on top of the cracked ALD Al_2O_3 as shown in Figure 33(d) and (e), respectively. Barrier HE-3 was prepared to determine the performance of an individual layer of PECVD SiNx with the thickness of 50 nm. By the deposition of 50 nm PECVD SiNx on the cracks in the ALD layer in case of barrier HE-4, crack healing by the PECVD layer was investigated. It is expected that the gaps created by the formation of cracks are filled up by the PECVD SiNx. These barrier films were encapsulated on Ca substrates and were exposed to humid conditions of 60°C/90% RH to determine their performance.

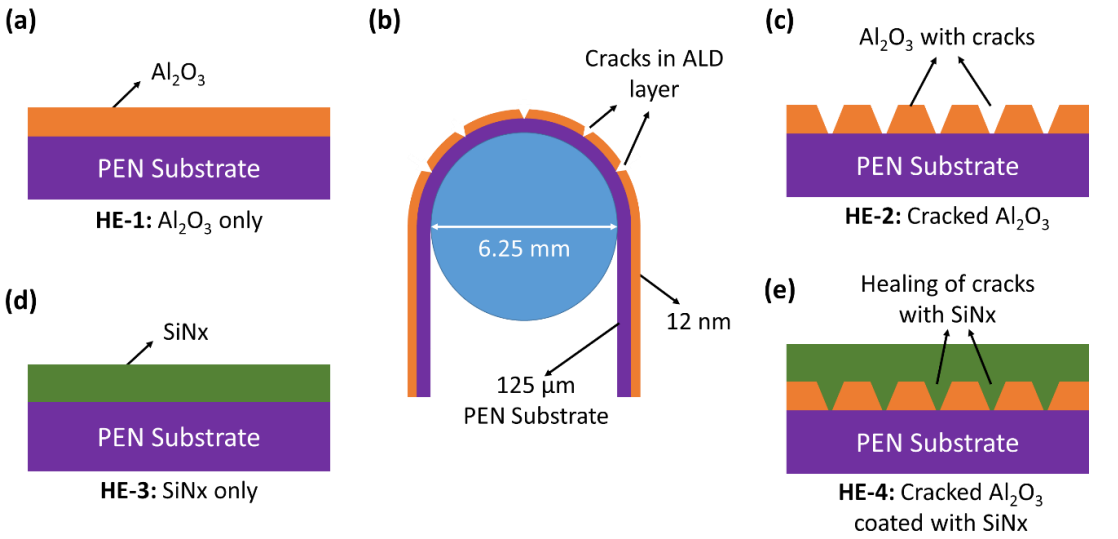

Figure 33 - (a) Cross-section of ALD Al_2O_3 deposited on PEN substrate. (b) Schematic showing the bending method for applying of 2% tensile strain on ALD Al_2O_3 films deposited on PEN substrates leading to the formation of cracks. (c) Schematic of the cross-section ALD Al_2O_3 layers consisting of cracks after bending. (d) Cross-section of PECVD SiNx deposited on PEN substrate. (e) Healing of cracks in ALD Al_2O_3 by SiNx.

4.2.7 Barrier film architectures for the influence of sequence of layers.

To further explore the impact of crack healing, hybrid barrier architectures which involved ALD and PECVD layers were studied. In this case, the order of deposition was explored where ALD followed by PECVD would allow crack healing and PECVD followed by ALD may not be as effective. The architectures are shown in Figure 34. The details of the structures used for this study are given in Table 1.

Table 1 - Structure of Barrier films.

Sample #	Structure
A1	PEN/500 nm SiNx/100 cyc Al_2O_3/Adhesive
B1	PEN/100 cyc Al_2O_3/500 nm SiNx/Adhesive
A2	PEN/1000 nm SiNx/100 cyc Al_2O_3/Adhesive
B2	PEN/100 cyc Al_2O_3/1000 nm SiNx/Adhesive

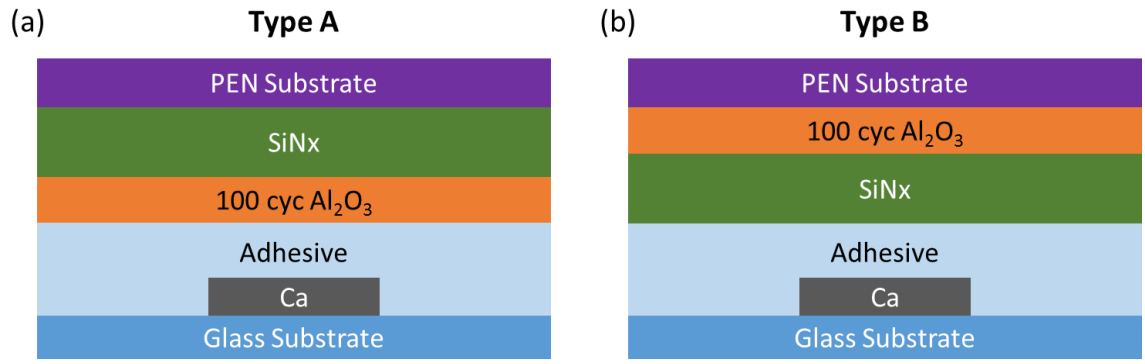

Figure 34 - Schematic of samples depicting difference in barrier film architectures.

4.3 Results and discussion

4.3.1 Performance of the barrier films containing particle inclusions of different composition.

Ca corrosion tests were conducted for the barrier films consisting of particles of different compositions, alumina and polymer, in the barrier matrix using indirect encapsulation method. The average size and density of the alumina particles were 1.81 ± 0.03 μm and 522 ± 65 particles/cm^2. Whereas, the average size and density of the polymer particles were 1.71 ± 0.46 μm and 606 ± 88 particles/cm^2. The images of the Ca samples before and after exposure to humid conditions of 60°C/90% RH are shown in Figure 35. Figure 35(a) represents the initial image of the Ca samples with all four Ca devices having uniform contrast, sharp edges, and no defect. Figure 35(b) shows the image of the Ca sample consisting of the barrier with alumina particle inclusions. It can be noted from Figure 35(b) that there is appearance of few spots in the Ca devices which is indicative of the defects created due to particles in the barrier film.[59, 60, 131] However, in case of

encapsulation with the barrier film consisting of polymer particle inclusions, the Ca sample degraded completely within 15 hours of exposure to humidity. Within these 15 hours, several particle defects appeared in the sample (not shown) leading to the rapid degradation of the sample. This points out that the polymer particle inclusions are much more detrimental to the barrier films as compared to the alumina particle inclusions. This observation indicates that the possibility of defect formation in the form of cracks in the proximity of particles is higher for those with polymeric origin. To confirm this, tensile tests were conducted on ALD Al_2O_3 coated samples which is discussed in the following section.

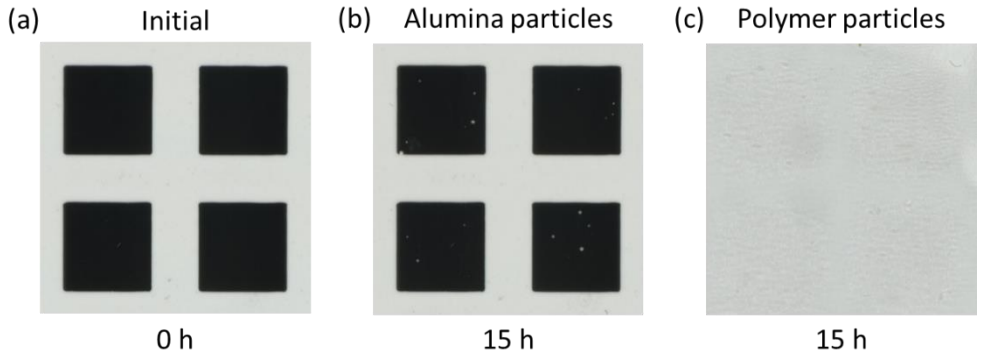

Figure 35 - Ca samples demonstrating the effect of nature of particle contamination on performance of barrier films.

4.3.2 Tensile test

Tensile tests were conducted to understand the effects of particle inclusions of different compositions on the crack onset strain of ALD Al_2O_3 films deposited on the PEN substrate. The list of samples used for tensile testing and their crack onset strains are shown in Table 2. The average size and density of alumina particles were 1.43 ± 0.16 μm and 1604 ± 233 particles/cm^2. Whereas, the average size and density of polymer particles were 1.12 ± 0.15 μm and 1591 ± 241 particles/cm^2. The images of first crack in these samples at crack onset strain are shown in Figure 36. The crack onset strain is determined to be the highest for Type I samples which consists of an ALD Al_2O_3 layer on PEN substrate with the value of 0.96 ± 0.07%. For Type II samples consisting of alumina particle inclusions in the ALD Al_2O_3 layer, the crack onset strain is slightly reduced to 0.92 ± 0.05%. This shows that even after the addition of alumina particles in the thin film matrix, there is not a huge change in the crack onset strain. However, for Type III samples consisting of polymer particle inclusions in the ALD Al_2O_3 layer, the crack onset strain is found to be minimum with the value of 0.72 ± 0.02%. Thus, polymer particles resulted in the decrease of critical onset strain by 25% as compared to the initial Type I samples.

The values of fracture energy and fracture toughness, i.e. strain energy release rates and stress intensity factors for all the three samples at their crack onset strains, are shown in Table 2. These values were calculated using equation (1) and the parameters of the films were same as those used for the modeling as shown in Table 3. It should be noted that the channel crack equation assumes the crack propagation ideally free from particles, which may not be the case for our results since the measurements also contain particle initiated cracks. However, the rough calculation based on equation (1) can still be valuable to build

guidance for what to expect concerning the fracture energy values of the cases considered in this work.

The highest fracture energy with the value of 15.84 ± 1.57 J/m^2 was measured for Type I samples which is slightly reduced to 15.11 ± 1.25 J/m^2 with the addition of alumina particles. However, with the addition of polymer particles, the value goes down to 10.85 ± 0.40 J/m^2. This means that cracks can propagate with much smaller amount of strain energy in case of polymer particle inclusions as compared to that of alumina particle inclusions. This implies that the thin films containing soft particles with polymeric origin are more prone to crack formation as compared to those having hard particles with ceramic origin. This supports the data obtained from the Ca corrosion test which showed that the barrier films with polymer particle inclusions degraded completely within 15 hours. Polymer particle inclusions must have led to the formation of large number of defects which resulted in high water permeation thereby leading to the rapid degradation of Ca.

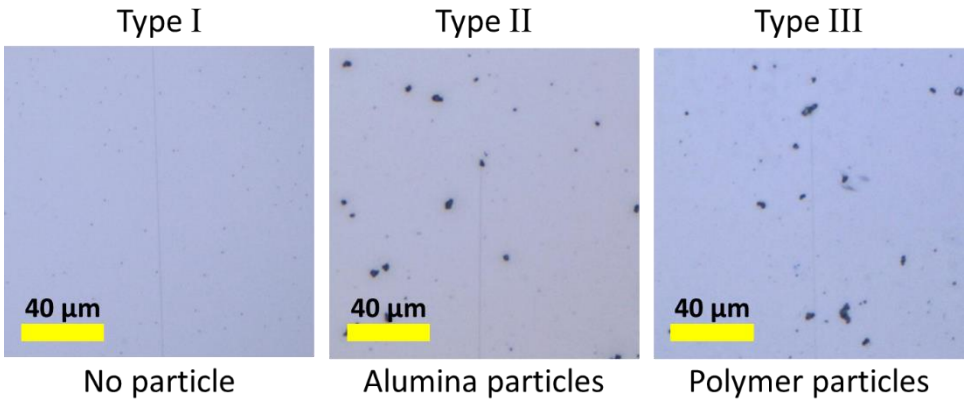

Figure 36 - Images of first cracks in the samples at the crack onset strain.

Table 2 - List of samples used for tensile test with their crack onset strain, fracture energy and fracture toughness.

Sample name	Structure	Crack onset strain (%)	Fracture Energy, Γ (J/m^2)	Fracture toughness, K ($MPa.m^{1/2}$)
Type I	50 nm Al_2O_3/PEN	0.96 ± 0.07	15.84 ± 1.57	1.53 ± 0.08
Type II	50 nm Al_2O_3/Alumina particles/PEN	0.92 ± 0.05	15.11 ± 1.25	1.50 ± 0.06
Type III	50 nm Al_2O_3/Polymer particles/PEN	0.72 ± 0.02	10.85 ± 0.40	1.27 ± 0.02

4.3.3 Finite Element Modeling

To understand the effect of modulus of elasticity of particle inclusions on the crack onset strain barrier films on a polymer substrate, finite element modeling is employed. Although the value of strain energy release rate is directly related to the crack onset strain as depicted in equation (1), this channel crack equation is not accurate for particle included structures where the crack tip is located right at the edge of particle. Therefore, we calculated the value of strain energy release rate 'G' using J-integral in the model for comparison between different conditions. In the model, higher G value at the same applied strain with the same dimensions of particle inclusion system would reach to the initiation of crack propagations earlier if the same fracture energy values are assumed for all cases.

For the experiments described in the previous section, the particles were seeded on the PEN substrates using their dispersions in IPA. These particles have random shapes and

sizes which cannot be replicated while modeling. Therefore, for modeling the effect of particles on crack onset, we have considered a hemispherical particle located on top of the PEN substrate as shown in Figure 32. ALD film conformally covers the top surfaces of the polymer substrate and particle. Using the simulation model, a parametric study was conducted by varying the elastic modulus of the particle from 4.07 GPa to 250 GPa. A strain of 1% was applied in the direction perpendicular to the crack to determine the value of energy release rate in each case. This gives the trend of energy release rate with variation in the elastic modulus of the particle. All other parameters and properties of the materials in the model are kept constant. The mechanical properties used for different components in the model are shown in Table 3. The role of residual stress in the ALD Al_2O_3 films was also considered, either by assuming that the film was free of residual stress or that the film contained a residual stress value of 548 MPa.

The values of strain energy release rate 'G' determined from the model for both cases of residual stress are plotted against the change in elastic modulus of the material, as shown in Figure 37. The value of 'G' goes from 2.21 J/m^2 to 0.33 J/m^2 for particles with elastic modulus changing from 4.07 GPa to 250 GPa. In the presence of residual stress of 548 MPa in the ALD layer, the value of 'G' becomes higher and varies from 2.96 J/m^2 to 0.47 J/m^2 for particles with similar change in the elastic modulus from 4.07 GPa to 250 GPa. Increase in G is expected since the tensile residual stress is added to the applied stress. From Figure 37, it is observed that the value of strain energy release rate 'G' is the highest for particles having the lowest elastic modulus i.e., with polymeric origin. Its value goes down exponentially with an increase in the elastic modulus of the particle. It is, therefore, still valid to say that particles of polymeric origin (with low elastic modulus) reach an onset

crack strain in thin film coatings at much lower values of applied stress/strain as compared to particles of ceramic origin (with high elastic modulus). The particle inclusions can get incorporated into the thin film matrix through different sources. Current results suggest that additional care must be taken when there is a possibility of contamination with particles of polymeric origin. It also suggests that the anti-blocking particles of ceramic nature would be less harmful as compared to those of polymeric origin.

Table 3 - Mechanical properties used for modeling.

Mechanical Properties	**ALD Al_2O_3**	**Polymer Substrate**	**Particle**
E (GPa)	140 [65]	4.07 [57]	4.07-250
ν	0.24 [65]	0.3 [57]	0.3
σ_{res} (MPa)	548	0	0

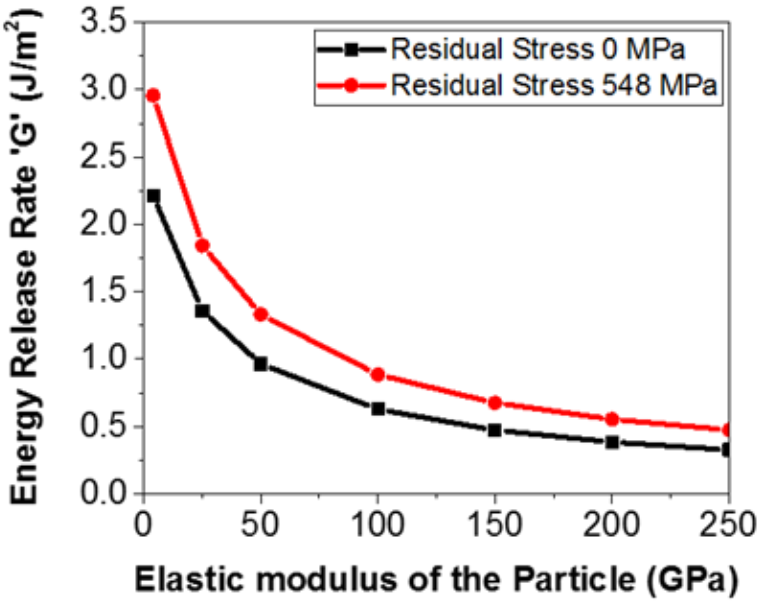

Figure 37 - Effect of change in modulus of particles on energy release rates with and without residual stresses in ALD layer.

4.3.4 Healing of cracks with PECVD SiNx

The performance of all the four barrier architectures shown in Figure 37 were determined using Ca corrosion test. Figure 38 shows the scanned images of Ca samples encapsulated using these barriers and exposed to humid conditions of 60°C/90% RH at various time intervals. From Figure 38, it can be seen that the HE-1 barrier, which consists of only ALD Al_2O_3 on PEN substrate, shows minimal degradation after 216 hours. There is an appearance of defects in the sample which is the result of particle contamination. The second sample that was encapsulated with the HE-2 barrier degraded completely within 3 hours of exposure to humidity. The barrier, HE-2, was prepared by the application of 2% tensile strain on the ALD Al_2O_3 layer. This strain value is higher that the critical onset

strain value of 0.96 ± 0.07% for ALD Al_2O_3 as discussed in the previous section. The applied strain of 2%, therefore, results in the formation of larger number of cracks in the ALD Al_2O_3 layer. The complete degradation of the sample encapsulated with HE-2 within 3 hours means that the cracks created in the ALD Al_2O_3 layer allowed the permeation of water through them at a very fast rate. Ca sample encapsulated with HE-3 barrier structure, which consists of 50 nm of PECVD SiNx, degraded completely after 39 hours of exposure. This means that the pristine PECVD SiNx layer, which is free from cracks or any other intentional defect, is not a good barrier. The sample encapsulated with HE-4 barrier structure degraded completely after 216 hours in humidity. The barrier HE-4 was prepared by the deposition of 50 nm of PECVD SiNx on cracked ALD Al_2O_3 on PEN. Individually, samples coated with HE-2 and HE-3 barrier structures lasted for only 3 hours and 39 hours, respectively. However, degradation of sample coated with HE-4 after 216 hours shows a huge improvement in the performance of cracked ALD Al_2O_3 (HE-2). This shows that the defects in the ALD Al_2O_3 layer were filled up with PECVD SiNx which resulted in the slowdown of water permeation through the defects. Since, the SiNx is not as good of a permeation barrier as that of ALD Al_2O_3, even after filling up the defects, it extends the lifetime of the Ca sample but does not perform better than the pristine ALD Al_2O_3 layer. This, however, shows that the PECVD SiNx, as thin as 50 nm, can be used to heal the defects in the ALD layer. For better performance, however, thicker layers of PECVD SiNx should be used. Thus, PECVD SiNx has the potential to be used as a healing material for cracks or defects in the ALD layers used for the fabrication of barrier films.

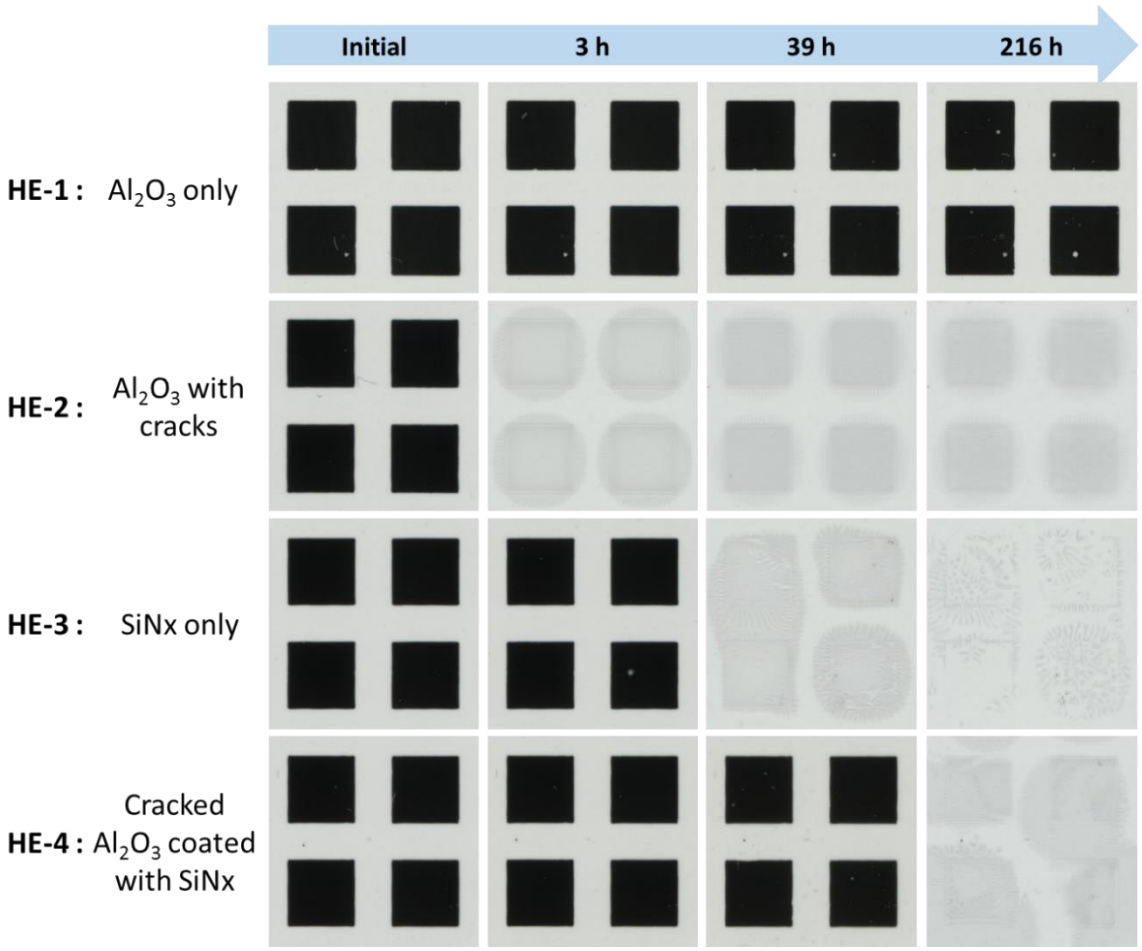

Figure 38 - Scanned images of Ca samples after exposure to humid conditions of 60°C/90%RH. These images demonstrate the degradation of Ca at different intervals representing the quality of different barriers used for their encapsulation.

4.3.5 Influence of the sequence of layers in barrier films.

Figure 39 shows the scanned images of Ca samples encapsulated with Type A and Type B barrier architectures at different time intervals of exposure to 60°C/90% RH. It is observed from Figure 39 that the Type A samples (with 500 nm or 1000 nm thick SiNx layers) have degraded at a much faster rate as compared to the Type B samples. Figure 40(a) and (b) show the degradation of Ca samples by presenting the total Ca area consumed

with time. It can be observed that until about 400 hours, there is ~1% decrease in the Ca area for both Type A and Type B samples. However, after 400 hours, Type A samples start showing an increase in the consumed Ca area. Beyond this time, localized defects actually start to appear in the Type A samples at a faster rate resulting in a rapid decrease in the Ca area. The delay in the appearance of defects can be attributed to the absorption of water by the getter materials present in the adhesive layer. However, the area degradation of the Ca in Type B samples is less than 1% throughout the testing period. While measuring the intrinsic barrier performance through the reduction in the Ca layer thickness, as shown in Figure 40(c) and (d), it was observed that a similar decrease in the Ca layer occurred for both Type A and Type B samples for the initial ~400 hours. After 400 hours, the Ca thickness also degrades much more rapidly for Type A samples. This effect can be attributed to the presence of large number defects in Type A samples. The appearance of large number of defects is indicative of the fact that the getter material in the adhesive layer is saturated completely which allows additional water to rapidly enter and degrade the Ca layers. The last column of images of Ca samples in Figure 39 shows the degradation of samples after 750 hours. It can be observed that the Type A samples have degraded almost completely whereas the Type B samples are still well protected. This is a clear evidence of the contrast in the performance of two barriers prepared using same inorganic layers but having different ordering of the ALD and PECVD layers.

Figure 41 shows the number of defects appearing in Type A and Type B samples during the testing period. It can be observed that the number of defects appearing in Type A samples is much larger than that of Type B samples. The defects appearing in the samples can be directly correlated to the defects present in the ALD Al_2O_3 layer because of lower

permeability of water through it as compared to the PECVD SiNx. Thus, the defects appearing in Type A samples could be the result of localized cracks around the particle contamination which appears in the Ca images. However, a significantly lower number of defects appear in case of Type B samples. This is because the cracks in the ALD layer are filled during the deposition of PECVD SiNx. The filling or healing of cracks with PECVD SiNx results in the reduction of defects in the ALD layer which is reflected by the appearance of smaller number of defects in Type B samples. This advocates that the ALD layers in the barrier films should always be followed by the deposition of PECVD SiNx as it can heal the defects in the ALD layer.

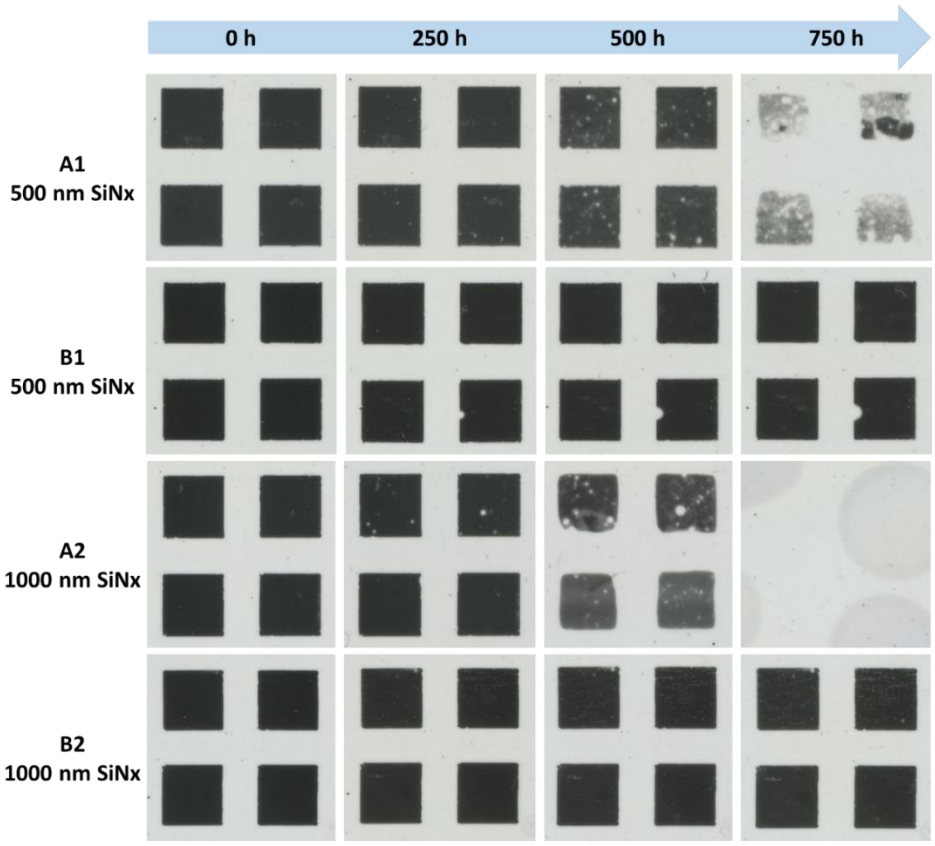

Figure 39 - Scanned images of Ca samples with time after exposure to humid environment at 60°C/90% RH.

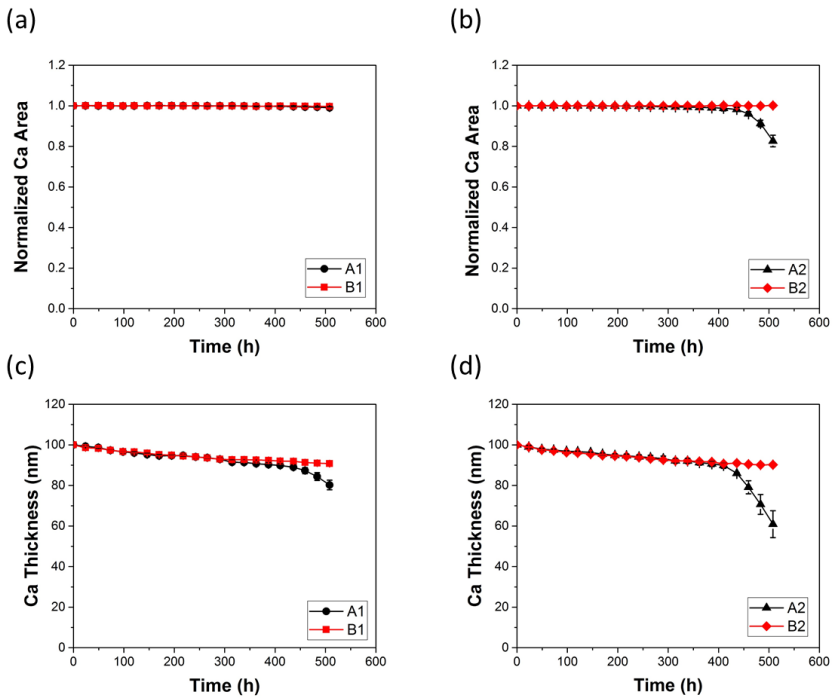

Figure 40 - Degradation of Ca samples on exposure to humidity at 60°C/90% RH. (a) and (b) change in Normalized Ca Area of samples with 500 nm SiNx and 1000 nm SiNx, respectively. (c) and (d) show changes in the Ca thickness for 500 nm SiNx and 1000 nm SiNx, respectively. All data show that the Ca samples show some level of degradation for Type A samples at a much earlier time than Type B samples.

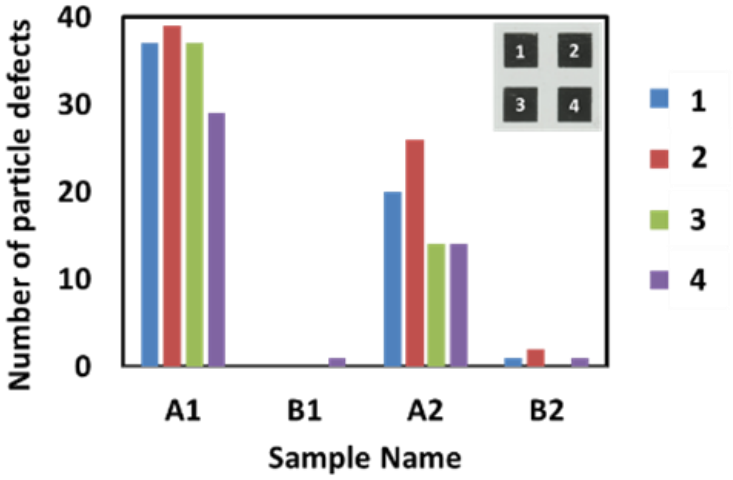

Figure 41 - Distribution of particle defects appearing in different samples. Inset in the figure shows the numbering of devices in the Ca sample.

4.4 Conclusions

This chapter demonstrates the effect of particle inclusions in thin film barrier matrix. Two kinds of particles with different origins were used, polymer particles and alumina particles. Using Ca corrosion test, the inclusions of polymeric origin were shown to have more detrimental effect on the performance of barrier films as compared to the alumina particle inclusions. The rapid degradation of Ca sample in case of barrier film with polymer particle inclusions was linked to the formation of large number of cracks in the proximity of polymer particles. Tensile stress tests were conducted using the same particles coated with ALD Al_2O_3 on PEN strips. The crack onset strain was found to be highest for ALD Al_2O_3 film without particles which decreased with the presence of particles in the matrix. Lowest value of crack onset strain was observed for ALD Al_2O_3 film containing polymer particles which confirmed the assertion that soft and more compliant particles (polymer) can lead to formation of larger number of cracks in thin film barriers as compared to hard and least compliant particles (ceramic). A parametric simulation study was further conducted by varying the elastic properties of particles embedded in the thin film matrix. It revealed that the value of strain energy release rate 'G' for crack propagation is highest for particles with the smallest value of elastic modulus. The strain energy release rate value decreases exponentially with an increase in the elastic modulus of the particles. It is therefore concluded that particles with polymeric origin in thin films can lead to crack formation at much lower value of stresses as compared to the ceramic particles. Thus, special care must be taken when there is a chance of polymer particle contamination. This study also suggests that anti-blocking particles with high elastic modulus should be used if the polymer rolls are going to be used as substrates for making thin-film barriers. It has

also been experimentally demonstrated that the order of inorganic layers in the encapsulation is extremely important. Since PECVD SiNx has been shown to have healing effect on the cracks in the ALD layer, it should always follow the ALD layer during the fabrication of barrier films.

CHAPTER 5. SIDE PERMEATION IN BARRIER ENCAPSULATION

5.1 Introduction

With the use of protective encapsulation like glass and ALD based ultrathin barrier films, moisture ingress can be significantly reduced.[21, 55, 68, 159] However, moisture can still diffuse into the devices through the sides of the barrier encapsulations. If indirect encapsulation is used.[160] While using barrier encapsulation, edge seals are used along the perimeter of the devices to prevent moisture ingress from the sides. Commonly used edge seal materials include polyisobutylene (PIB) and epoxies. These edge seal materials are often the weak link since their permeation rates are higher than most ultrabarrier films. Therefore, these materials are often incorporated with desiccants to improve their efficiency.[160]

When barriers are applied on devices using an indirect encapsulation, the application of edge seal between the device and the barrier leads to the formation of two interfaces. The first interface is between the device and the edge seal material, and the second interface is between the edge seal and the barrier. Due to the imperfect nature of the contacts, there is the formation of small pores or voids at the interfaces. A connected network of these pores can act as a new pathway for water permeation in the form of capillaries, in addition to the permeation of water through the bulk of the sealant material. Although water is present in the atmosphere in the form of water vapor, under the conditions of high humidity and relatively low temperature of the device as compared to

the surroundings, condensation of water can take place on the device. Under such condition, liquid water can also ingress through the capillaries formed by the pores. Since the movement of water in the capillaries is governed by the surface energies of capillary walls, changing the materials at the interfaces can play a significant role in controlling the permeation rates. Studies conducted on the development of barrier films have been focused only on the quality of barriers in terms of water vapor transmission rate (WVTR) through the barrier structures as discussed in the previous chapters. However, the effect of permeation through the sides along the interfaces of encapsulation has not received significant attention. When the capillaries are formed at the interface and have water permeation through them, then the performance of the edge seal is governed by the faster permeation mechanism, which is either through the interface or through the bulk of the sealant material.

In this chapter, the effect of materials at the interfaces of edge seal and the barriers on side permeation during indirect encapsulation of devices has been demonstrated. Three types of samples were prepared using PECVD SiNx, ALD Al_2O_3 and ALD TiO_2. The first structure of the barrier encapsulation consists only PECVD SiNx and ALD Al_2O_3 with SiNx at the interface. For the other two structures, the first barrier is modified by depositing 10 cycles of ALD (~1 nm thickness) to change the interface material without significantly changing the intrinsic properties of the barriers. This provided similar barrier films with different materials at the interface. Using these samples, we experimentally demonstrate the significance of interface materials on side permeation. Through mathematical modeling, the rate of water permeation through the capillaries and bulk of a polymer has also been compared to show the contrast in their respective water permeation rates.

5.2 Experimental Methods

Barrier films were prepared by depositing ALD Al_2O_3, ALD TiO_2 and PECVD SiNx on 125 µm thick PEN substrates. As shown in Figure 42(a), Type A barrier structure was prepared by the deposition of 100 cyc ALD Al_2O_3 on PEN substrates at 100°C using a plasma enhanced atomic layer deposition (PEALD) system (Cambridge Nanotech, Fiji) followed by the deposition of 500 nm PECVD SiNx using Unaxis PECVD tool at 110°C. The outer surface of Type A barrier was modified by the deposition of 3 cycles of ALD Al_2O_3 followed by 7 cycles ALD TiO_2 to make Type B barrier architecture, as shown in Figure 42(b). Similarly, for Type C, 10 cycles of ALD Al_2O_3 was deposited on outer surface of Type A, as shown in Figure 42(c). For PEALD depositions, trimethyl aluminum (TMA) and tetrakis(dimethylamido) titanium (TDMAT) were used as metal precursors, and oxygen plasma was used as an oxidizer with plasma power of 300 W for the deposition of Al_2O_3 and TiO_2, respectively. The thicknesses of the films deposited were measured using a Woollam M2000 ellipsometer.

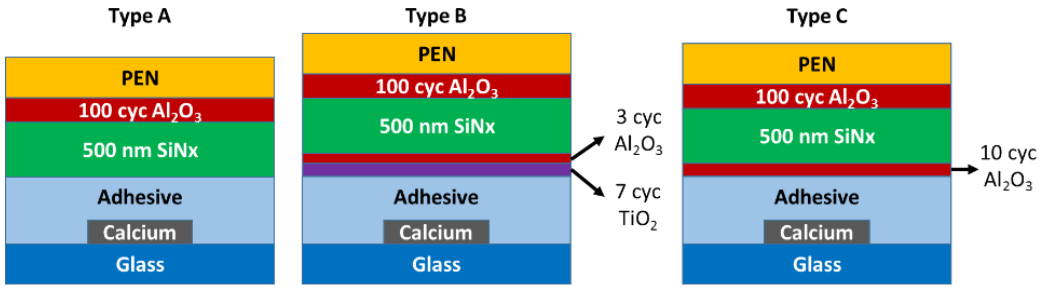

Figure 42 - Schematic of samples representing encapsulation using different barrier architectures (inverted barrier structure) on Ca substrates using a double-sided adhesive.

Optical Ca tests were used to determine the performance of barrier films. The Ca square sensors were deposited with the dimensions of 5 mm x 5 mm and 100 nm thickness, on a detergent solvent cleaned glass substrate. The deposition of these Ca sensors was carried out using an EvoVac thermal evaporator (Angstrom Engineering, Inc.) connected to a nitrogen glove box at a base pressure of 10^{-7} Torr with deposition rate of 2 Å/s. The sensors were deposited in a 4 x 4 array for a total of 16 sensors. The barrier films were attached to the Ca sensors using a 25 μm thick, double sided UV-curable adhesive (Tesa tape) in a glove box. The structures of samples are shown in Figure 42. The list of the specific barrier architectures is shown in Table 4.

For testing, the barrier coated Ca samples were placed in a controlled environment of 60°C/90% RH in Cincinnati Subzero Micro-Climate System for ~360 hours. The samples were taken out of the humidity chamber at ~24 hours interval and optical images were taken using an optical scanner with the resolution of 2400 dpi to observe any change in the area of Ca sensors. Further details of the scanning method can be found in the work by Kim *et al*.[131]

Table 4 - Structure of Barrier films.

Sample	Structure
Type A	PEN/100 cyc Al_2O_3/500 nm SiNx/Adhesive
Type B	PEN/100 cyc Al_2O_3/500 nm SiNx/3 cyc Al_2O_3/ 7 cyc TiO_2/Adhesive
Type C	PEN/100 cyc Al_2O_3/500 nm SiNx/10 cyc Al_2O_3/Adhesive

5.3 Theoretical Model Development

It is important to understand the origin of capillary forces to properly develop the model for capillary flow along the interface. Fundamentally, the capillary forces originate from surface or interfacial energy. The molecules or atoms located in the bulk of a material experience equal forces from all the directions. However, the molecules or atoms, that are present at the surface, experience unequal forces from the bulk and the surroundings leading to the formation of surfaces or interfaces with excess energy, called as interfacial energy (γ). In case of interactions between a solid body and a liquid media, the surface tension of liquid tries to minimize the total energy of the fluidic system which basically is the origin of capillary forces.[161] Therefore, the interaction of forces at the tri-junction of a liquid, solid and air interface is described by Young's law as

$$\gamma_{sa} = \gamma_{sl} + \gamma_{la} cos\theta_c \qquad 5.1$$

where, θ_c is the contact angle between the solid and liquid surfaces as shown in the Figure 43. When the liquid is present between two parallel solid surfaces, a capillary is created as shown in Figure 44. The velocity of the capillary meniscus in this capillary is governed by the surface energies of the liquid and the solid surfaces. In case of edge seals, the interface materials are different and therefore, can have different contact angles with the liquid (water). Figure 44 represents a partially filled capillary of length 'L', width 'b' and surface separation 'h'. The contact angles of water with the surfaces of the capillary are θ_1 and θ_2. The total surface energy of the system can be divided into four parts. First is the surface energy of filled portion of the capillary of length 'x' where water is in contact with both

the surfaces. Second is the empty region of the capillary of length 'L-x'. Third is the surface energy of meniscus and fourth is the surface energy at both the ends of the capillary along the width 'b'. Since the thickness 'h' of the capillary is extremely small compared to its length and width (for edge seals), all surface energies associated with it can be ignored. Thus, the total surface energy 'E' of the capillary can be expressed as

$$E = 2(L - x)b\gamma_{sa} + xb\left(\gamma_{sl_1} + \gamma_{sl_2}\right) \qquad 5.2$$

where, γ_{sa} is the surface energy at solid-air interface and, γ_{sl_1} and γ_{sl_2} are the surface energies at both the solid-liquid interface.

Using Young's law for both the surfaces, equation 5.2 can be written as

$$E = 2Lb.\gamma_{sa} - xb.\gamma_{la}(cos\theta_1 + cos\theta_2) \qquad 5.3$$

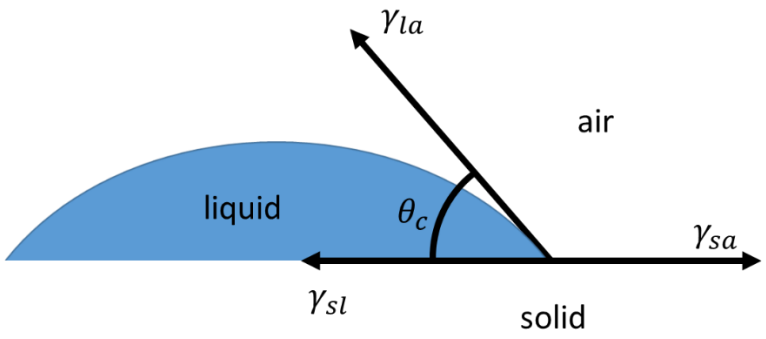

Figure 43 - Surface forces acting at different interfaces for a droplet.

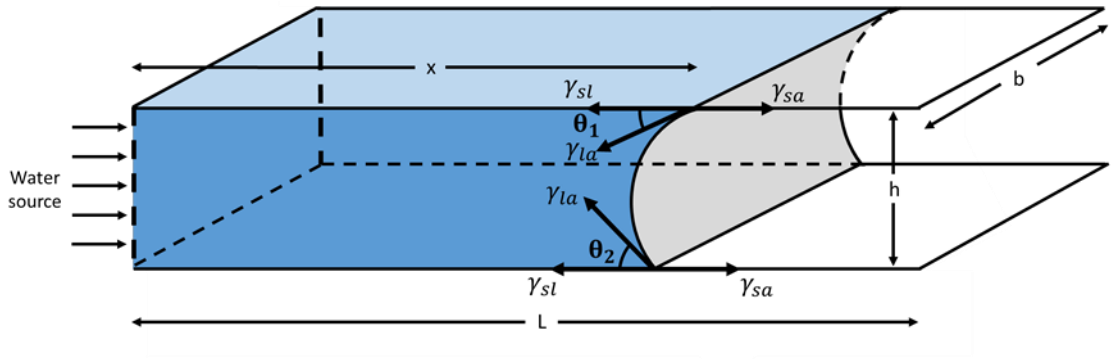

Figure 44 - Configuration of capillary meniscus formed by the presence of water between two surfaces with different contact angles.

The derivative of equation 5.3 with respect to 'x' gives the equivalent capillary force F applied on the fluid column along x-direction.

$$F = -\frac{dE}{dx} = \gamma_{la} b(cos\theta_1 + cos\theta_2) \qquad 5.4$$

Thus, the pressure drop 'ΔP_{la}' across the meniscus is determined as following:

$$\Delta P_{la} = \frac{F}{hb} = \frac{\gamma_{la}(cos\theta_1 + cos\theta_2)}{h} \qquad 5.5$$

As shown in Figure 44, with the supply of water without any external pressure, the movement of the water front is solely driven by the pressure drop across the meniscus. To derive the relation for the movement of meniscus front in the capillary, incompressible Navier-Stokes equation is used.[161] The current system is treated as a one-dimensional time-variant fluid field where velocity '$u = u(y,t)$' varies along the vertical direction and

with time. The instantaneous position ‘x’ of the capillary meniscus can be described by the following equations:

Continuity equation (conservation of mass) can be written as following.

$$\frac{\partial u}{\partial x} = 0 \tag{5.6}$$

Momentum equation (conservation of momentum) can be written as following.

$$\frac{\partial u}{\partial t} = -\frac{1}{\rho}\frac{dP}{dx} + \frac{\mu}{\rho}\frac{\partial^2 u}{\partial y^2} \tag{5.7}$$

$$-\frac{dP}{dx} = \frac{1}{x}\frac{\gamma_{la}(cos\theta_1 + cos\theta_2)}{h} \tag{5.8}$$

Equation (5.8) shows that the driving force for the movement of meniscus is only due to the surface tension between water and capillary surfaces.

Velocity of meniscus can be written as following.

$$u(0,t) = \frac{dx}{dt} \tag{5.9}$$

Velocity with no-slip boundary conditions can be written as following.

$$u\left(\frac{h}{2}, t\right) = u\left(-\frac{h}{2}, t\right) = 0 \tag{5.10}$$

Initial condition at time t = 0 and x = L_0 can be written as following.

$$u(y, 0) = 0 \tag{5.11}$$

where, L_0 is initial length of the capillary filled with water. Assuming the profile of meniscus to be parabolic, the velocity distribution across the thickness of the meniscus can be represented by the following equation.

$$u(y, t) = x'.[ay^2 + by + c] \tag{5.12}$$

Equation 5.12 can be written as equation 5.13, where the parabolic term satisfies the initial condition and no-slip boundary conditions with surfaces having different contact angles.

$$u(y, t) = x'.\left[-\frac{4}{h}y^2 - \frac{4}{h}\left(\frac{\tan\theta_1 + \tan\theta_2}{\tan\theta_1 - \tan\theta_2}\right)y + 1\right] \tag{5.13}$$

Putting the values from equation 5.8 and 5.13 in the momentum equation 5.7, we get

$$x''.\left[-\frac{4}{h}y^2-\frac{4}{h}\left(\frac{\tan\theta_1+\tan\theta_2}{\tan\theta_1-\tan\theta_2}\right)y+1\right]+\frac{8\mu}{\rho h}x' = \frac{2\gamma_{la}(cos\theta_1+cos\theta_2)}{\rho h x} \quad 5.14$$

Averaging of equation 5.14 through the thickness of the capillary

$$\left[x''.\left[-\frac{h}{3}+1\right]+\frac{8\mu}{\rho h}x'\right].x=\frac{2\gamma_{la}(cos\theta_1+cos\theta_2)}{\rho h} \quad 5.15$$

Neglecting the double derivative in equation 5.15,

$$x'.x=-\frac{1}{A\mu}\frac{\gamma_{la}(cos\theta_1+cos\theta_2)}{h} \quad 5.16$$

For an initial condition of $x'(0) = 0$; $x(0) = L_0$;

$$x=\sqrt{L_0^2+Dt} \quad 5.17$$

where,

$$D=\frac{h\gamma_{la}}{4\mu}(cos\theta_1+cos\theta_2) \quad 5.18$$

where, D is the diffusion coefficient [161] of fluid in a capillary attached to a liquid source, without any effect from gravity.

5.4 Results and discussion

The Ca substrates were encapsulated with barrier films having three different architectures, Type A, Type B and Type C, as shown in Figure 45. After encapsulation, the samples were exposed to the controlled environmental conditions of 60°C/90% RH. Figure 45(a) shows the typical image of the sample before exposure to the humid environment. Figure 45(b), (c) and (d) are the images of Ca samples exposed to the humid conditions for ~360 hours with Type A, Type B and Type C barrier architectures, respectively. It can be seen from Figure 45(a) that the edges of Ca devices are straight and sharp before exposure to the humid conditions. However, after exposure to the humid conditions for ~360 hours, the edges of Ca devices, which are on the outer side of the samples, become blunt and have moved receded from the edges, whereas the edges of all 4 central Ca devices, which are located at the center of each sample, remain intact. This indicates that there is permeation of water from the sides of the samples which results in partial degradation of Ca devices from the sides. It can be noted from Figure 45(b), (c) and (d) that the extent of side permeation is different in all the three samples with Type A having largest displacement of the edges while Type C having the smallest displacement of the edges.

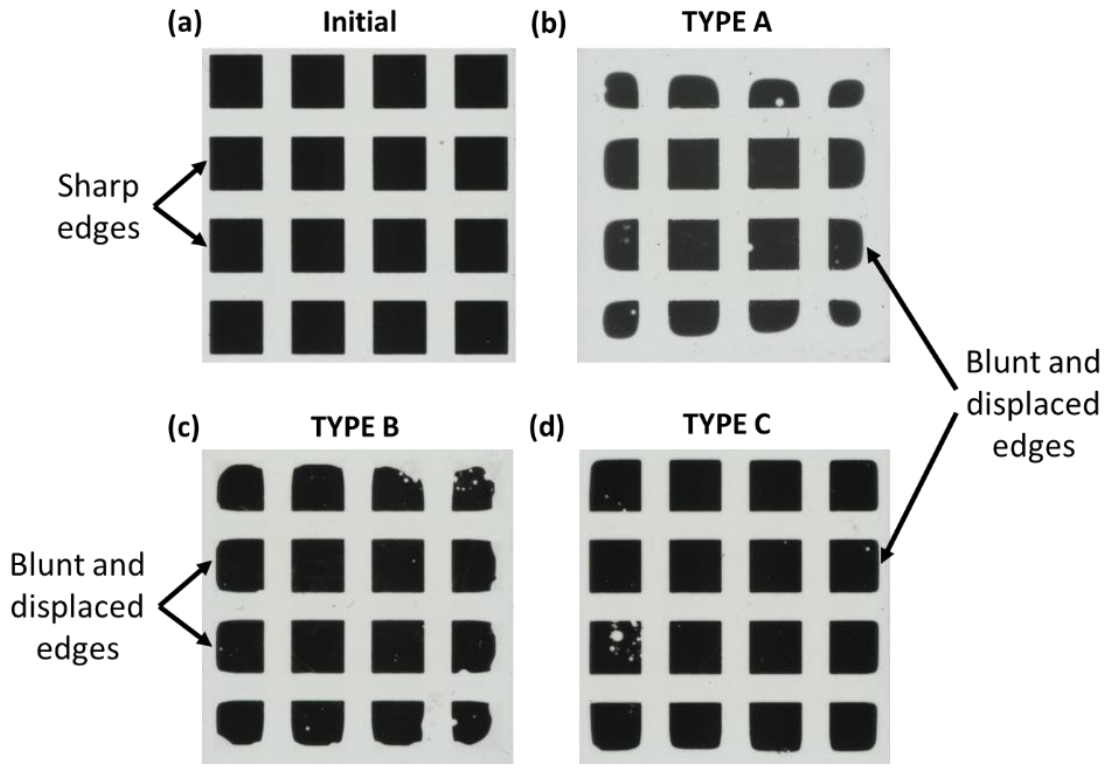

Figure 45 - Optical images of Ca samples at different durations in humid environment (60°/90% RH).

The side permeation rates for the encapsulated samples were determined by measuring the distance moved by the outer edge of each Ca device with respect to its initial condition as shown in Figure 46(a). The Ca devices, that are located at the corners of the samples, have higher and uneven permeation due to their proximity to two ends of the sample. Therefore, such Ca devices were not considered for measuring the rates of side permeation. However, the Ca devices, that are located at the center of the sides of the samples, have water permeation only from one direction due to which the permeation is uniform. Therefore, for determining the rates of side permeation, only the Ca devices that are located at the center of each side have been used as indicated by the device numbers

from 1 to 8 in Figure 46(a). Plots in Figure 46(b), (c) and (d) show the distance moved by the outer edges of all 8 Ca devices along the sides of the samples. These plots consist of two regions. First is the horizontal part indicating that there is no change in position of the edge of Ca devices, and second is the slope indicating movement of respective outer edges. From these plots, lag time is determined by the slope of constant permeation rate and thereby, effective diffusivity is calculated for each Ca device using the following equation.[162]

$$\text{Effective diffusivity, } D_{eff} = \frac{l^2}{6L} \qquad 5.19$$

where, l is the initial distance of Ca edge from outer edge of the sample, L is the lag time, and D_{eff} is the effective diffusivity from the outer edge of the sample. Effective diffusivity calculated from the slopes in Figure 46(b), (c) and (d) for all the Ca devices are shown in Figure 47. It is clearly seen from Figure 47 that Type A sample has the highest rate of side permeation with the effective diffusivity of 3.14×10^{-11} m^2/s, whereas, Type C sample has the least rate of side permeation with the effective diffusivity of 3.69×10^{-12} m^2/s. Effective diffusivity of Type B sample is intermediate of the two with the value of 1.36×10^{-11} m^2/s. The only difference in the barrier architectures of Type A samples used for the encapsulation of Ca devices from Type B and Type C samples is the deposition of 10 cycles of ALD coating as shown in Figure 42. The overall thickness of ALD coatings is about 1 nm and has been used to change the surface properties of the barrier material at the interface with the adhesive without significantly changing any other parameter like surface roughness. All other parameters of the samples are kept constant. Thus, an order of

magnitude difference between the effective diffusivity of Type A and Type C samples indicates that the material at the interface with the adhesive plays a significant role in the rate of side permeation.

In the encapsulated device structures, water can permeate through different paths as shown in the Figure 48. The first path is the permeation from the top through the barrier film, called as intrinsic permeation. This kind of permeation would decrease the thickness of the Ca devices uniformly and would not specifically etch the sides of the Ca devices. Second is the permeation through the sides of the encapsulation. Water can permeate through the bulk of the adhesive layer or through the interfaces formed on either side of the adhesive during encapsulation as indicated in Figure 48. Since the thickness of the adhesive layer and one of the interfaces of the adhesive with the glass substrates are same for all the three samples, the permeation of water through these two will also be same. The only difference in all the three architectures is the interface material between the adhesive layer and the barrier. Therefore, the interface materials could be the reason for any difference in side permeation for all the samples. In the insets of Figure 46, contact angles for the materials at the interfaces of barriers are shown. It is observed from the values for effective diffusivity that smallest contact angle material (SiNx) at the interface has the highest value of diffusivity (3.14×10^{-11} m^2/s) whereas largest contact angle material (Al_2O_3) at the interface has lowest value of diffusivity (3.69×10^{-12} m^2/s). This data clearly indicates that the contact angle of the materials at the interfaces can significantly impact side permeation.

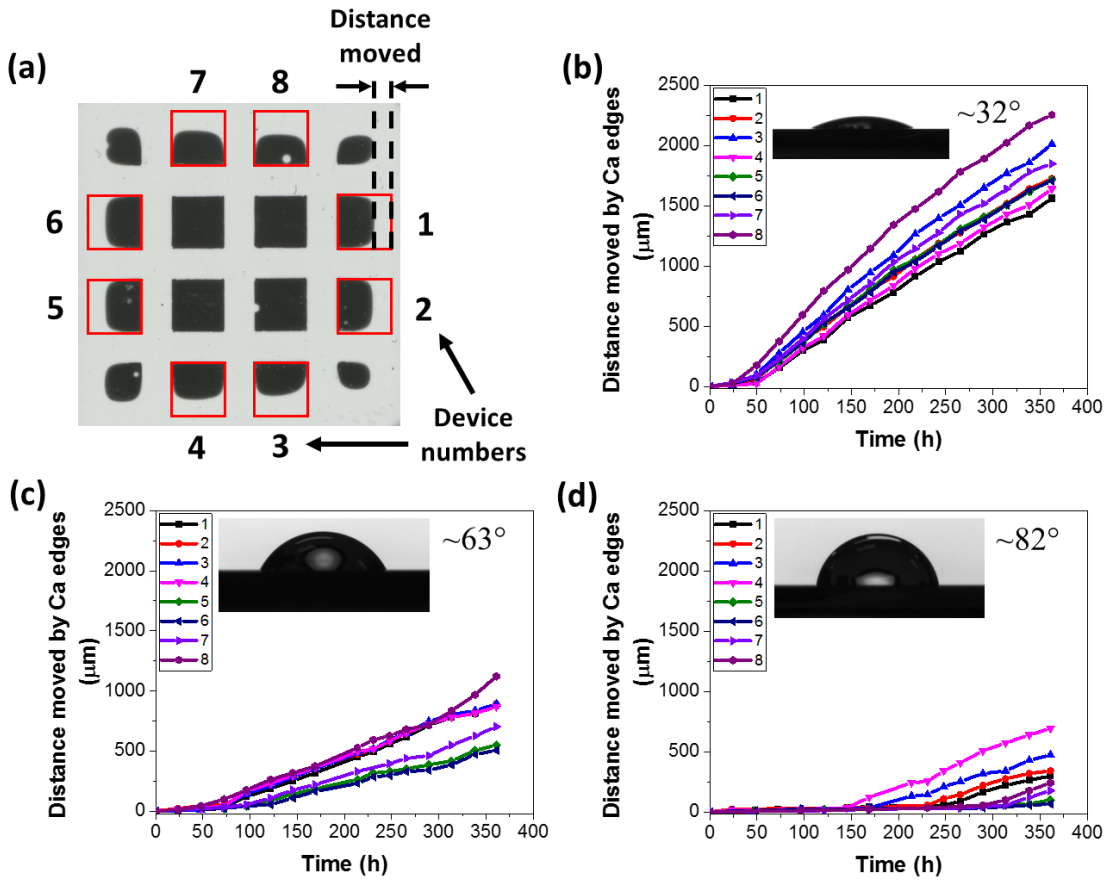

Figure 46 - (a) Image of Ca sample representing distance moved by the edge of a Ca device from its original position represented by red square box. The device numbers represent the Ca devices used for determining the movement of device edges. (b), (c) and (d) Plots of distance moved by the edges of 8 Ca devices with time for samples with PECVD SiNx, ALD TiO_2 and ALD Al_2O_3 as the interface materials, respectively. Insets in the figure represent contact angles of materials at the interface with water.

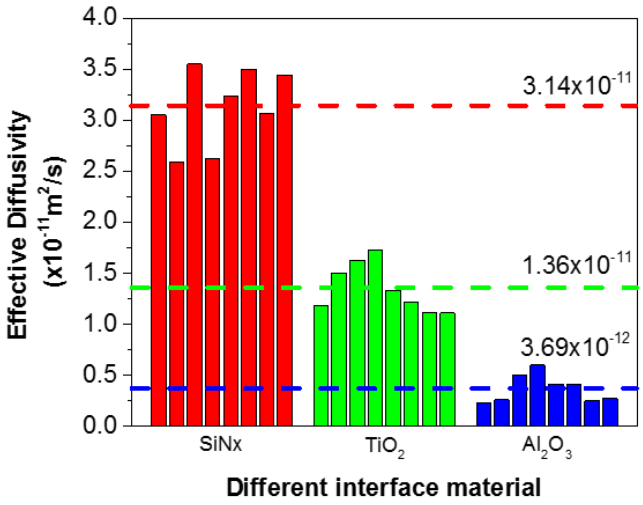

Figure 47 - Side permeation rates for samples with different interface materials between the barrier and the adhesive.

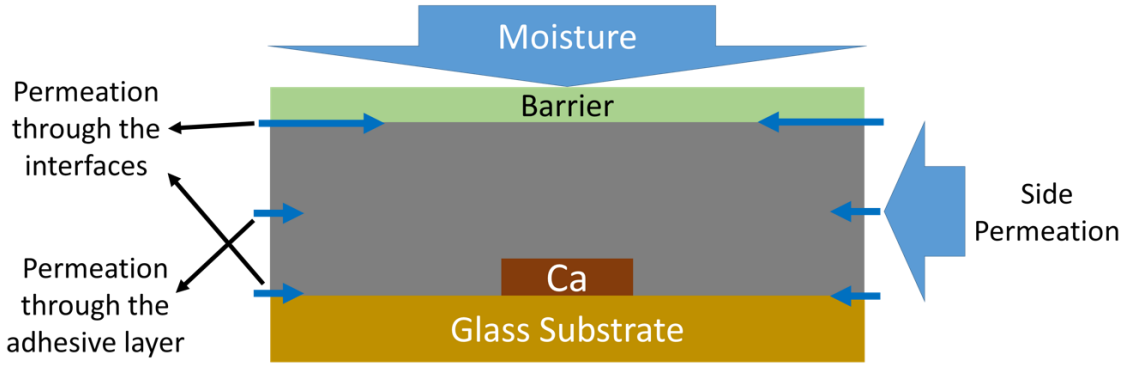

Figure 48 - Various permeation pathways possible for water ingress in an encapsulated device.

5.5 Comparison of diffusivity through the bulk and capillaries

The materials used as edge seal and adhesives are polymeric in nature and can contain desiccant materials.[160, 163] Typically, the diffusion coefficient of a polymer material is in the order of 10^{-10} m^2/s or less. Because of better quality of the adhesive material and presence of desiccants in them, the diffusion coefficient of water vapor through the bulk of the adhesive can be much lower. Therefore, for comparison of diffusion coefficient of water through the bulk of the adhesive with that of the capillaries at the interface, the value of 10^{-10} m^2/s can be used as a conservative upper limit estimate.

At room temperature, the surface energy of water-air interface is 71.99×10^{-3} $N.m^{-1}$ and the dynamic viscosity of water is 8.90×10^{-4} Pa.s.[164] The values of diffusion coefficients for a capillary with the thickness of 10 nm and different contact angles on both the sides are shown in Figure 49. Equation (5.18) has been used for the calculation of diffusion coefficient of water through the capillaries. It can be seen from the plot in Figure 49 that the value of diffusion coefficient 'D' reduces with an increase in contact angle. This means that the permeation rate through the capillaries can be reduced by using materials with lower contact angles.

From the plots in Figure 49, it is also observed that for all the values of contact angles ($\theta_1, \theta_2 < 88.5°$) of the capillary surfaces, the magnitude of diffusion coefficient of water through capillaries is higher than the diffusion coefficient of water vapor through the bulk of the polymer material by at least 3 orders of magnitude. This shows that the rate of water diffusion through the capillaries can be significantly higher in certain conditions. This can result in the preferential permeation of water through the interfaces due to

capillary forces acting between the surfaces of the adhesive and the barrier. As a result, water front through the capillaries along the interface can move ahead to that of the bulk of the adhesive and then, it can permeate from the capillaries into the bulk of the adhesive leading to early saturation of the adhesive as compared to that due to permeation from the bulk alone. However, if the contact angles of both the interface materials increase beyond 88.5°, there is a rapid decrease in the value of diffusion coefficient of water through the capillary and it approaches 0 m^2/s at 90°. Under such conditions, the permeation rate through the capillaries is reduced significantly, and when the contact angle is 90° and beyond, the side permeation rate is solely governed by the bulk of the adhesive material. This indicates that it would be beneficial to have a material with higher contact angles at the interface.

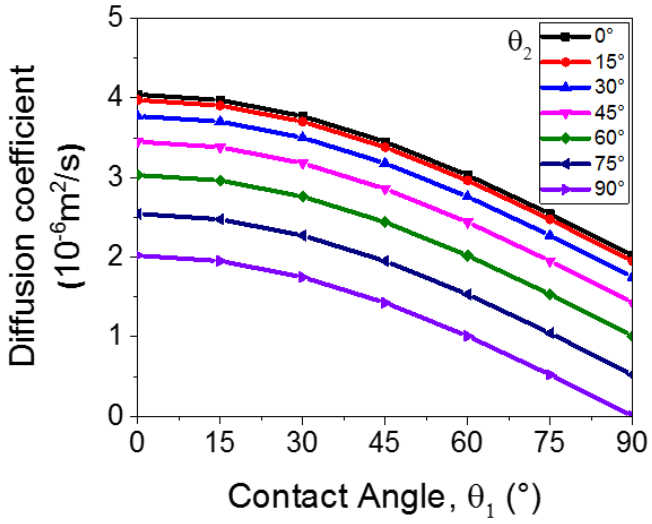

Figure 49 - Diffusion coefficient of a capillary of thickness 10nm with varying contact angles on both the surfaces of a capillary. Contact angles (θ_1) for first surface are represented along x-axes. Different plots represent different values of contact angles (θ_2) for second surface.

5.6 Conclusions

In this chapter, the impact of interface materials on side permeation in barrier encapsulations has been demonstrated. When devices are encapsulated using barriers and adhesives or sealants, due to imperfect nature of the contact, pores or voids may be formed at the interface. Such features can be the result of surface roughness and porous nature of the adhesive material. It has been experimentally demonstrated that the surface property of the materials at the interfaces can significantly affect the rates of water permeation, which in turn affects the quality of barrier film. The barrier with material having lowest contact angle at the interface had highest diffusivity whereas the barrier with highest contact angle at the interface had lowest diffusivity. It is, therefore, recommended to use the materials with higher contact angles at the interfaces between the adhesive/sealants and the barriers to achieve lower rates of side permeation.

CHAPTER 6. STABILITY OF ALD FILMS IN BIOLOGICAL SOLUTIONS

6.1 Introduction

Miniaturized medical and wearable electronic devices have recently gained significant popularity for their new capabilities and ease of application.[73-77] During their application, these devices are exposed to harsher conditions when compared to conventional electronics. As an implant or a wearable device, they are exposed to various bodily fluids with varying pH and salt concentrations. Exposure to such an environment can lead to the rapid degradation of the devices leading to their untimely failure. To avoid such a condition, a robust protective barrier for these devices is required which protects them from getting exposed to various species present in the surrounding media.

Thin film metal oxides deposited using ALD can be a potential candidate for application as a protective barrier for various electronic devices like sensors and implants in biological environment. Therefore, in this chapter, the cytocompatibility and chemical stability of several ALD metal oxides has been explored in different biological solutions. First, the cytocompatibility of the four ALD metal oxides, Al_2O_3, HfO_2, TiO_2 and ZrO_2, using the MTT cell proliferation test was determined. After confirming the cytocompatible nature of all these ALD metal oxides, their chemical stability in 3 biological solutions, namely phosphate buffered saline (PBS), saliva and sweat solutions has been investigated. PBS is a simplified biological environment. Simulated sweat (artificial perspiration) most closely resembles human eccrine perspiration. Simulated saliva (Fusayama/Meyer

artificial saliva) was chosen based on its primary use for testing biodegradability of dental metal alloys. All the ALD materials were deposited at 100°C on a glass substrate that contained a gold electrode for electrochemical impedance spectroscopy (EIS) analysis. The chemical stability or corrosion of the ALD films was determined using EIS over a 21 day period. Equivalent electrical circuit models were employed to characterize the mechanism of degradation at different stages of exposure.

6.2 Experimental

6.2.1 Atomic layer deposition

ALD films were deposited using a plasma enhanced atomic layer deposition (PEALD) system (Cambridge Nanotech, Fiji) at 100°C. For PEALD deposition, trimethyl aluminum (TMA), tetrakis(dimethylamido) hafnium (TDMAH), tetrakis(dimethylamido) titanium (TDMAT), and tetrakis(dimethylamido) zirconium (TDMAZ) were used as precursors for the deposition of Al_2O_3, HfO_2, TiO_2 and ZrO_2, respectively. Oxygen plasma was used for 20 seconds as an oxidizer with plasma power of 300 W. The thicknesses of ALD films were measured using a Woollam M2000 ellipsometer by depositing them on silicon substrate. The number of ALD cycles used for deposition of different materials and their final thickness is shown in Table 5.

Table 5 - ALD material, precursors, pulse times, number of cycles and final thickness.

Material	Precursor	Pulse (s)	ALD Cycles	Thickness (nm)
Al_2O_3	TMA	0.06	100	12.69
HfO_2	TDMAH	0.25	100	13.66
TiO_2	TDMAT	0.20	200	13.14
ZrO_2	TDMAZ	0.25	100	13.75

6.2.2 MTT Test

(3-(4,5-Dimethylthiazol-2-yl)-2,5-Diphenyltetrazolium Bromide) (MTT) crystals were purchased from Biotium (Cat:30006). Dulbellcco's Modified Eagle's Media (DMEM) and calf serum were purchased from ATCC. Penicillin Streptomycin was purchased from VWR Life Science (Cat: 97062-806). The cytotoxicity evaluation of ALD materials was performed with the MTT assay. Glass coverslips coated with Al_2O_3, HfO_2, TiO_2 and ZrO_2 were sterilized under UV for 30 min and then carefully moved to 24 well plates. NIH-3T3 cells (passage 100) were seeded on top of the coated coverslips at density of 50,000/well in complete medium (DMEM with 10% calf serum and 1% antibiotics Penicillin Streptomycin). Cell media was removed after culturing for 18 h at 37˚C (humidified, 5% CO_2). 180 µl fresh medium with 20 µl of MTT reagent was added to each well. After 2 h incubation, 200 µl of DMSO was added to each well and pipetted several times to dissolve the formazan salt. Upon mixture, the absorbance signal was measured on

a plate reader (BioTek Synergy H4) at 570 nm (signal) and 630 nm (background). Normalized absorbance values were obtained by subtraction of background absorbance (630 nm) from signal absorbance (570 nm). Dunnett's statistics test was performed with one-way ANOVA multiple comparison to compared the experimental groups (cells cultured on ALD coated slides) with control group (cells cultured on plain tissue culture plates).

6.2.3 Electrochemical measurements

Electrochemical impedance spectroscopy (EIS) measurements were performed using the customized setup and sample structure as described in section 3.4 with ALD Al_2O_3, HfO_2, TiO_2 and ZrO_2. The setup and sample used for EIS testing are shown in Figure 24 and Figure 25, respectively. The thickness of each ALD layer is mentioned in Table 5. EIS measurements were conducted in PBS, simulated saliva and sweat solutions by applying a frequency range from 10^{-1} to 10^5 Hz and an amplitude of 10 mV. The measurements were taken at regular intervals over a period of 21 days. PBS was obtained in powder form from Amresco and the PBS solution with strength of 1x was prepared by dissolving 9.88 g of powder in 1 L deionized water. The composition of 1X PBS solution is 137 mM NaCl, 2.7 mM KCl and 9.8 mM Phosphate buffer. Both the simulated sweat and simulated saliva solutions were provided by Pickering Laboratories, Inc. Simulated saliva (Fusayama/Meyer Artificial Saliva) consisted of 0.4g/L KCl, 1.0 g/L urea, 0.4 g/L NaCl, 0.69 g/L sodium phosphate monobasic dihydrate, 0.906 g/L calcium chloride dihydrate, and 0.005 g/L sodium sulfide nonahydrate in deionized water. Simulated sweat

(Artificial Perspiration, DIN 53160-2:2010/BS EN 1811:2011) consisted 5.0 g/L NaCl, 1.0 g/L urea, and1.0g/L lactic acid in deionized water.

6.2.4 Chemical characterization

Chemical characterization of the ALD films were conducted with X-ray photoelectron spectroscopy (XPS) on a Thermo Scientific K-Alpha X-ray photoelectron spectrometer system with a monochromatic Al K_α X-ray source ($h\nu$ = 1486.6 eV). The chemical state of the ALD materials was determined before and after exposure to the solutions for 21 days. To compensate for charging effects, all the XPS spectra were shifted with respect to adventitious carbon (C1s) peak at 284.8 eV.

6.3 Results and discussion

6.3.1 Cytocompatibility of ALD materials

To test the cytocompatibility of ALD materials, a MTT based *in vitro* cytotoxicity study was performed with NIH-3T3 murine fibroblast cells cultured on ALD coated slides for 18 hours. To compare each of the experimental groups (cells cultured on ALD coated slides) with control group (cells cultured on plain tissue culture plates), Dunnett's statistics test was performed with one-way ANOVA multiple comparison. No significant difference in cell viability was observed, as shown in Figure 50, indicating no cytotoxicity effect for all 4 ALD materials used for coating. Therefore, all of the ALD coatings chosen for this

study demonstrate cytocompatibility for use in devices exposed to biological environments for short time frames.

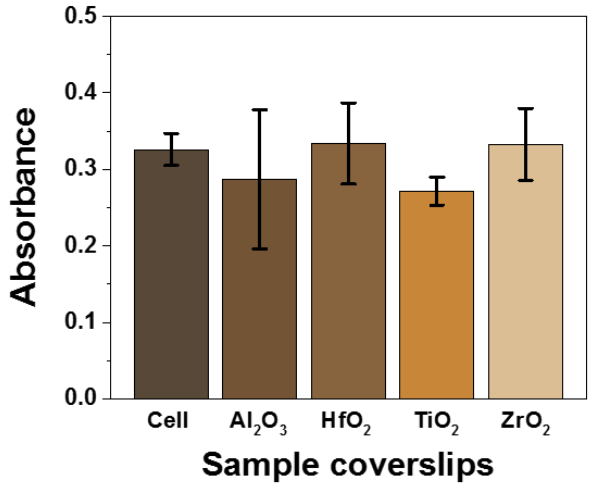

Figure 50 - Normalized absorbance intensity of 570 nm wavelength through the control and ALD coated coverslips. No significant difference (Dunnett's statistic test) in absorbance was observed between control group and each different sample coated coverslips, indicating ALD coatings were cytocompatible.

6.3.2 ALD films in PBS solution

The bode plots of ALD films in PBS solution are shown in Figure 51. The inset in the figures represent phase change plots of first and last measurement for the respective materials. In case of ALD Al_2O_3, there is high impedance in low frequency region as seen in the Figure 51(a). The inset in this figure shows a nice capacitive behavior for ALD Al_2O_3 film initially. At this stage, the impedance response from ALD Al_2O_3 film tends to follow circuit #2. This means that the initial ALD Al_2O_3 film is uniform with the presence of some pinholes in it. With time, on exposure of ALD Al_2O_3 to the PBS solution, it was observed that there is a continuous decrease in the impedance of the film in lower frequency regime,

approaching towards that of the bare electrode. The minimum value was obtained on 21st day of measurement. Similar tendency was observed for phase shift as well. The phase response of the ALD Al_2O_3 shifted towards that of the bare electrode on last day of measurement. This indicates that there is a continuous thinning of the ALD Al_2O_3 layer due to dissolution of the material into the PBS solution. The XPS data for ALD Al_2O_3 in PBS solution is shown in Figure 52(a). It is clear from the XPS data that the intensity of Al2p peak has reduced significantly and only traces of Al_2O_3 remain on the electrode surface. The peaks from the electrode material, i.e. Ti and Au (not shown), were clearly visible, confirming the removal of ALD Al_2O_3 from the electrode surface. Throughout the measurement period for ALD Al_2O_3, only one time constant was observed in the phase response of the system and circuit #2 could fit all of them. This means that the dissolution of ALD Al_2O_3 into the PBS solution was uniform throughout.

Figure 51(b) shows the bode plots for ALD HfO_2 in PBS solution. It can be seen that there is not much difference in the initial and final impedance plots of the ALD HfO_2 layer. However, in the encircled region of Figure 51(b), there is some widening in the gap between impedance plots in low frequency region (below ~50 Hz). From the inset in the Figure 51(b), it is seen that there is no significant change in the initial time constant for the system. However, as compared to the first measurement, there appears an additional time constant in the low frequency region. The widening in the impedance response at lower frequencies and appearance of an additional time constant indicate towards the formation of a new capacitive area in the sample. On fitting the equivalent circuits to the impedance data, it was observed that the impedance response of first measurement followed circuit #2, whereas the last measurement data followed circuit #3. This indicates that ALD HfO_2

was, initially, a uniform film. However, after exposure to the PBS solution, degradation started in the material. The XPS data revealed that there is a peak shift in the binding energy of Hf4f indicating towards chemical change in the ALD material, as shown in Figure 52(b). This is consistent with the results from EIS where there some change in the material was observed. While broadening in the low frequency region, the impedance data shift towards that of the bare electrode indicating that the newly formed region is thinner than other regions of ALD HfO_2. This means that the degradation of the ALD HfO_2 is not as uniform as that of ALD Al_2O_3. Instead, localized degradation or thinning occurred in the HfO_2 layer which could be the result of selective etching of the material near the defect sites.

Figure 51(c) shows the bode plots for ALD TiO_2 in PBS solution. It can be seen in the plots that there is no significant change in impedance response of the sample with time. All the impedance plots appear to overlap indicating that there is no significant change in the material with time. The equivalent circuit used to fit the EIS data was circuit #2 throughout the experiment duration. The phase plot of ALD TiO_2 taken after 21 days overlaps with the first measurement plot indicating that ALD TiO_2 is quite stable in PBS solution. This is also supported by overlap in binding energy peaks for Ti2p before and after exposure to PBS for 21 days, as shown in Figure 52(c).

Figure 51(d) shows the bode plots for ALD ZrO_2 in PBS solution. The impedance response from the ALD ZrO_2 material has changed with time. As compared to ALD HfO_2, there is more widening between the impedance plots in the low frequency region. The data fitting shows that the first measurement followed circuit #2 whereas last measurement followed circuit #3 indicating towards the formation of second region of thickness different from rest of the material. This is also supported by the appearance of second time constant

in the phase response of ALD ZrO_2 as shown in the Figure 51(d). This means that there is localized degradation of the material. XPS data revealed that there is a shift in binding energy for Zr3d peaks, as shown in Figure 52(d), resulting from change in chemical state of Zr in ALD ZrO_2.

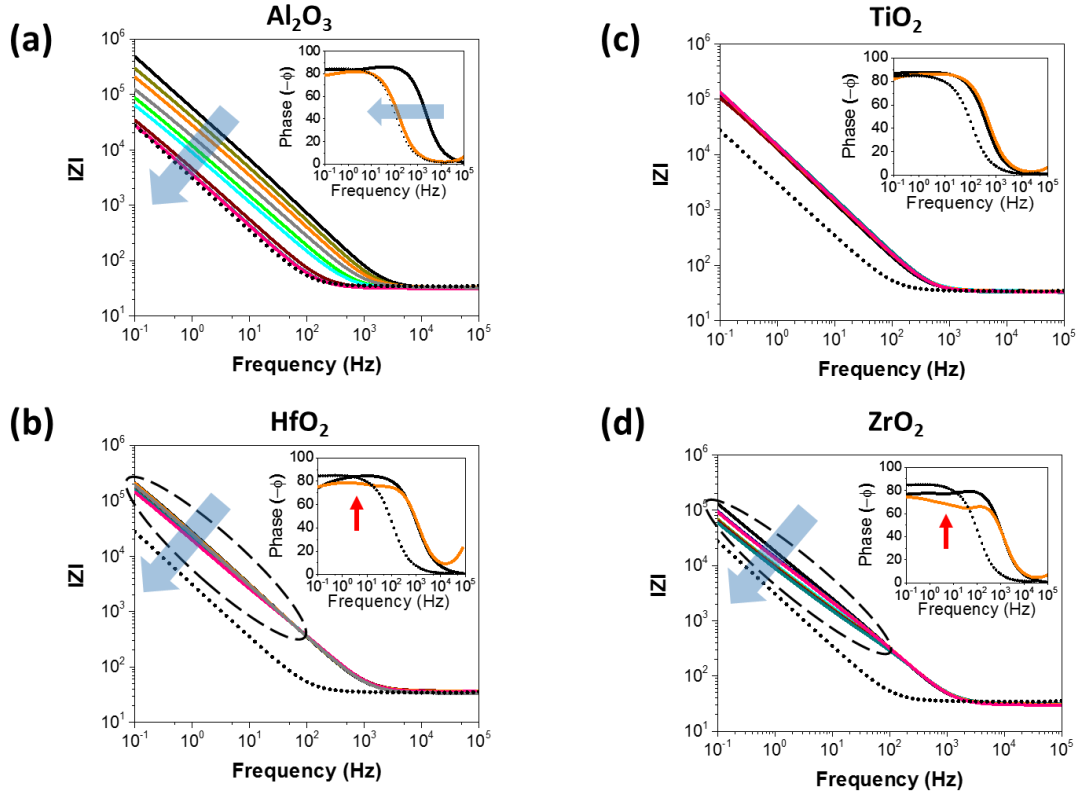

Figure 51 - EIS response in PBS for (a) Al_2O_3, (b) HfO_2, (c) TiO_2, and (d) ZrO_2 over a time period of 21 days. Dotted line represents impedance response from bare electrode. Blue arrows point towards the direction of measured data. Insets in the figure represent phase response for first and last measurement. Red arrow point towards the appearance of second time constant in the phase plots.

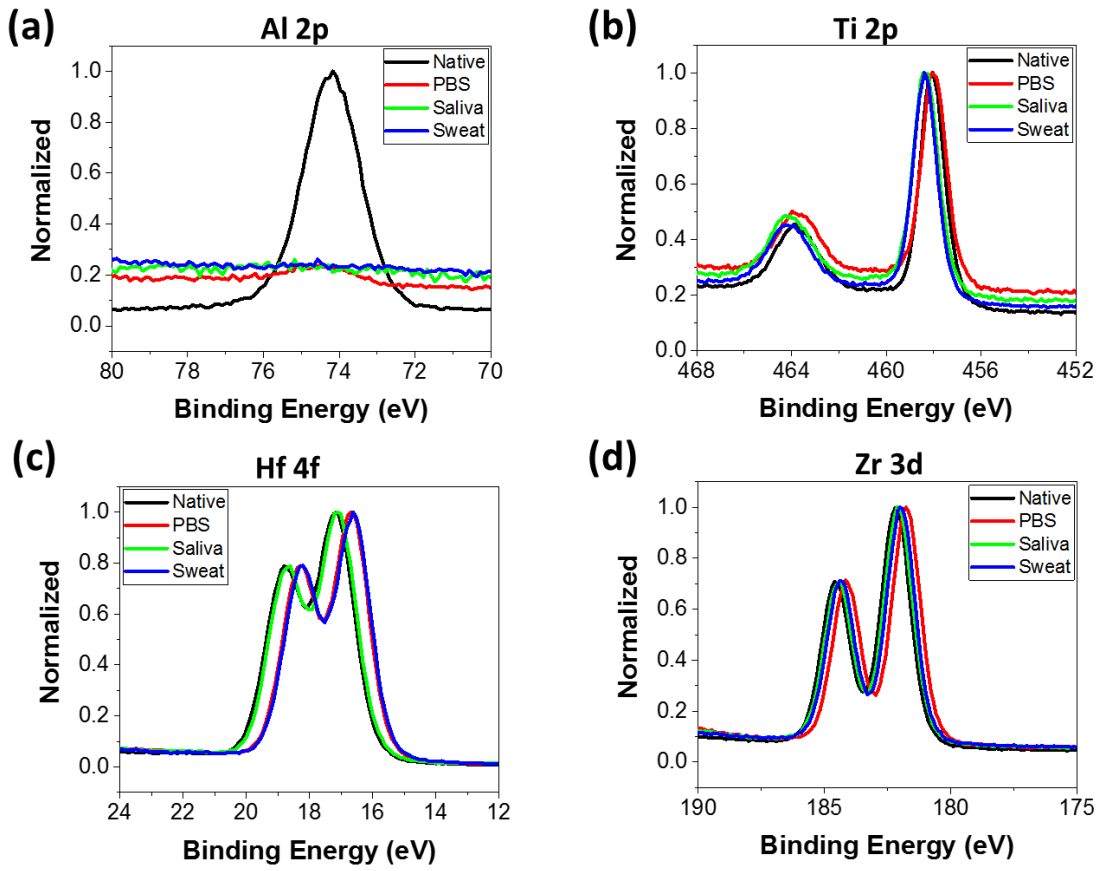

Figure 52 - XPS spectra of metallic elements. Color code: Black represents binding energy for native samples (before exposure) to biological solutions. Red, green and blue represent binding energy for samples in PBS, saliva and sweat after exposure for 21 days, respectively.

6.3.3 ALD films in Saliva solution

The bode plots for the ALD films in saliva solution are shown in Figure 53. The inset in the figures represent phase change plots of initial and last measurement for respective materials. In case of ALD Al_2O_3, there is high impedance in low frequency region as seen in the Figure 53(a) similar to what it was in the case of PBS solution. The inset in this figure shows a nice capacitive behavior for ALD Al_2O_3 film initially. At this

stage, the impedance response from ALD Al_2O_3 film tends to follow circuit #2 which means that the initial ALD Al_2O_3 film is uniform. However, after 1 day, there is sudden change in the impedance response of the ALD Al_2O_3 material. The impedance from the sample matches to that of the bare electrode indicating that ALD Al_2O_3 was completely removed from the substrate surface. As shown in the inset of Figure 53(a), the phase change plot for ALD Al_2O_3 after 21 days overlaps to that of the electrode. The equivalent circuit that fits the data from 1 day onwards is circuit #1. This clearly indicates that there is no ALD Al_2O_3 remaining on the substrate surface. The XPS spectra taken for this sample after 21 days show that there is no trace of Al on substrate surface as shown in Figure 52(a). Only the peaks for Ti and Au from the electrode were obtained which is consistent with the observation from EIS data. Thus, ALD Al_2O_3 was completely dissolved into the saliva solution within a day, such that no intermediate step could be detected. This means that ALD Al_2O_3 is highly unstable in saliva solution.

Figure 53(b) shows the bode plots for ALD HfO_2 in saliva solution. The EIS data for first measurement fits to circuit #2 indicating towards uniform deposition of the film. However, on exposure of the film to saliva solution, there is a change in impedance response indicating towards degradation of the material. On comparing the data taken for the period of 21 days in the middle region of frequency (~100 Hz), the impedance plots overlap throughout the measurement period as shown in the Figure 53(b). However, there is a continuous widening in the gap between the impedance plots at lower frequency region. From the inset in the Figure 53(b), it is seen that there are two time constants as opposed to only one in case of first measurement. At this stage, circuit #3 fits well to the EIS data indicating that there is formation of second region in the material such that the two regions

have different thicknesses. The XPS spectra taken for ALD HfO_2 after 21 days of exposure to saliva solution shows that there is a shift in peak of Hf4f towards lower binding energy. This means that HfO_2 is not entirely stable, chemically, in the saliva solution. However, the rate of chemical degradation of the material is not as fast as that of ALD Al_2O_3. As indicated by the EIS and XPS data, ALD HfO_2 is dissolved into the solution resulting into the thinning of the ALD layer. However, non-uniform decrease in thickness of the material means that there is selective etching or removal of ALD HfO_2. This could be the result of presence of highly vulnerable sites near the proximity of pinholes and other defects.

Figure 53(c) shows the bode plots for ALD TiO_2 in saliva solution. It can be seen in the plots that there is a slight change in impedance response of the sample with time. On comparing the impedance response of the material for 21 days, it can be seen from the Figure 53(c) that there is widening in impedance response on either side of ~5 Hz frequency. This indicates towards the formation of two different regions in the sample which should have two different time constants. This is confirmed by the phase change plot in the inset of Figure 53(c) where there is appearance of two time constants. Thus, the EIS data measured on first day followed circuit #2 whereas last measured data followed circuit #3, indicating towards formation of two regions in the sample with different thicknesses. This could be the result of slow degradation of ALD TiO_2 at some selective regions in saliva solution. XPS data reveals that there is an increase in binding energy of Ti2p on exposure to saliva indicating towards the chemical interaction between the ALD TiO_2 and components of saliva solution. Thus, XPS data supports the conclusion from EIS data of having change in the state of TiO_2 material. Since there is formation of two regions with different thicknesses, as indicated by the presence of two time constants and data fitting to

equivalent circuit #3, the decrease in thickness of the sample in certain regions could be due to the rapid degradation at highly vulnerable sites near the defects in the layer.

Figure 53(d) shows the bode plots for ALD ZrO_2 in saliva solution. The impedance response from the ALD ZrO_2 material has no noticeable change with time. From inset in the Figure 53(d), it can be seen that there is no significant change in the time constant for last measurement as compared to the initial measurement. Same equivalent circuit #2 could fit all the data for ALD ZrO_2 throughout the experimental period. This indicates that there is no apparent dissolution of ALD ZrO_2 into the surrounding media. However, as per XPS data, there is a change in peak position for binding energy of Zr3d towards lower value indicating a change in chemical state of ZrO_2 at the surface. But, consistent impedance response from the material throughout the experiment duration indicates that the newly formed material does not get dissolved into the saliva solution and thus get removed from the substrate surface. Thus, ALD ZrO_2 can be considered to be a highly stable material in saliva solution.

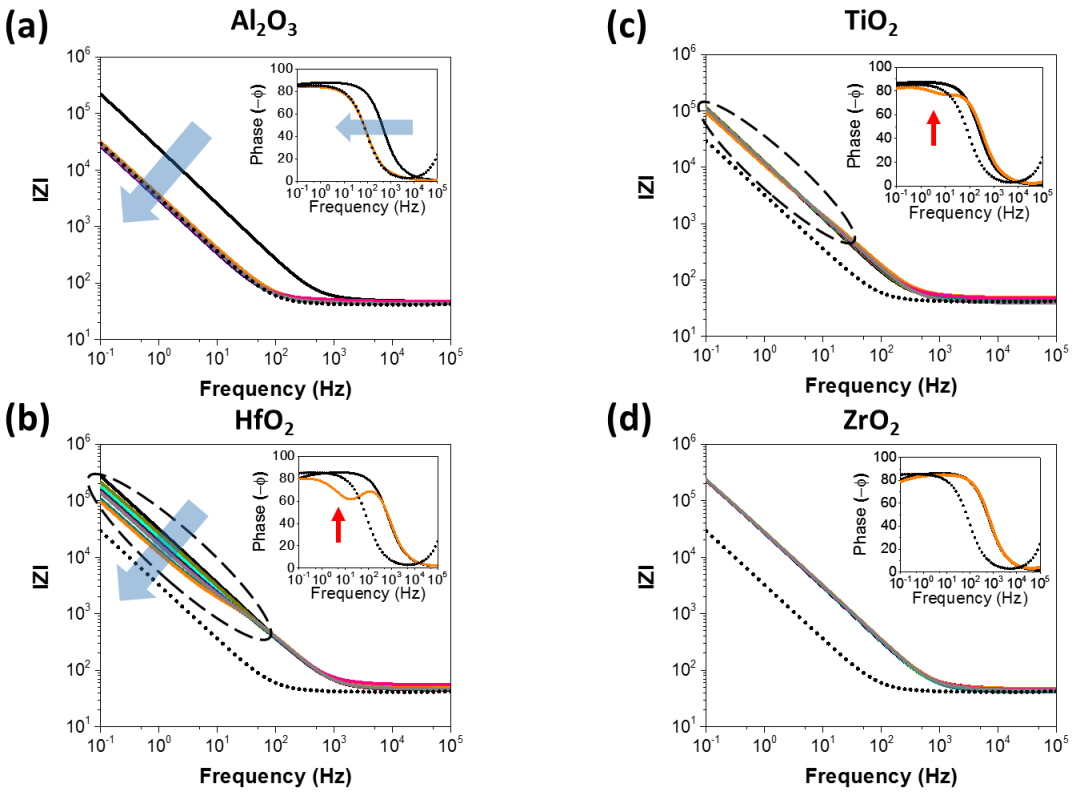

Figure 53 - EIS response in saliva solution for (a) Al_2O_3, (b) HfO_2, (c) TiO_2, and (d) ZrO_2 over a time period of 21 days. Dotted line represents impedance response from bare electrode. Blue arrows point towards the direction of measured data. Insets in the figure represent phase response for first and last measurement. Red arrow point towards the appearance of second time constant in the phase plots.

6.3.4 ALD films in Sweat solution

The bode plots of the ALD films in sweat solution are shown in Figure 54. For ALD Al_2O_3, similar to that of other two solutions, there is high impedance in low frequency region as shown in the Figure 54(a) with inset showing a nice capacitive behavior of the film during first measurement. Circuit #2 fits the EIS data at this stage of the sample indicating towards uniform deposition of ALD Al_2O_3 on the substrate surface. However,

on exposure of ALD Al_2O_3 to the sweat solution, a sudden change in impedance behavior of the film, similar to that in the saliva solution, was observed. The second impedance measurement that was taken after 1 day of first measurement shifted significantly towards lower frequency overlapping with that of the bare electrode. This means that there was complete removal of ALD Al_2O_3 within a day. From second measurement onwards, all the impedance data overlapped. From second measurement onwards, circuit #1 fits all the impedance data indicating the absence of Al_2O_3 from substrate surface. XPS data, as shown in Figure 52(a), shows that there is no trace of Al on the substrate which is consistent with the observation from EIS that the complete removal of ALD Al_2O_3 has taken place. It can, therefore, be concluded that ALD Al_2O_3 dissolved completely into the surrounding media within a day. After this, there was no material remaining on electrode surface for further dissolution and hence, no change in the impedance response from the sample was observed after 1 day onwards. Thus, ALD Al_2O_3 is highly unstable in sweat solution.

Figure 54(b) shows the bode plots for ALD HfO_2 in sweat solution. The first set of impedance measurement fits well with circuit #2 indicating towards uniform deposition of the film. However, on exposure of the film to sweat solution, its impedance response changes indicating towards degradation of the material. On comparing the data taken for the period of 21 days, it can be seen that, in the middle to low frequency regime (below ~100 Hz), as indicated by the encircled region, the impedance plots start to diverge more and more throughout the measurement period. The impedance data at this stage fits well with circuit #3 implying that there is formation of a region in the sample which has different thickness than rest of the sample. This is supported by the presence of two time constants for the sample after 21 days as shown in the inset of the Figure 54(b). The thinning in the

HfO_2 layer could be the result of dissolution of material into the solution. XPS analysis of the surface after 21 days, as shown in Figure 52(b), revealed that there is a shift in binding energy for Hf4f, indicating change in chemical state of the ALD material. This indicates that there could be dissolution of HfO_2 into the solution as a result of chemical interaction with the surrounding species. Thus, HfO_2 is not stable in sweat solution.

Figure 54(c) shows the bode plots for ALD TiO_2 in sweat solution. The first impedance measurement fits well with circuit #2 indicating towards uniformly deposited film. However, on exposure of the material to sweat solution, the impedance response from the ALD material changes in the lower frequency region. In the region below the frequency of ~10 Hz, widening in the gap between impedance plots can be observed with time, as shown in the Figure 54(c). This indicates that there is formation of a region with thickness other than rest of the material, similar to that of ALD HfO_2. This is supported by the presence of second time constant in the inset of the Figure 54(c). As the impedance plot in low frequency region tends to shift towards that of the bare electrode, it can concluded that there is thinning in the material thickness in some parts of the sample. During this stage, the impedance data fits well with circuit #3. The decrease in thickness of the sample could be due to the formation of defects and removal of material from the ALD layer. The XPS spectra, as shown in Figure 52(c), shows that there is a peak shift in the binding energy of Ti2p peaks. This implies that there is chemical interaction between ALD TiO_2 and the surrounding species which could have resulted in dissolution of the material into the solution, leading to thinning of the ALD layer. As per impedance data, the change in thickness of TiO_2 is not uniform throughout the sample. This means that the rate of decrease in thickness of the TiO_2 layer is higher at sites in the proximity of defects. Since the

broadening in the impedance peak in case of TiO_2 was smaller than that of HfO_2, it can be concluded that TiO_2 is more stable in sweat.

Figure 54(d) shows the bode plots for ALD ZrO_2 in sweat solution. Similar to other ALD films, the first impedance data shows a nice capacitive behavior of the film while fitting well with circuit #2. However, on exposure of the ALD film to sweat solution, a continuous change in the impedance spectra was observed with time. From Figure 54(d), it can be seen that there is widening in the gap between the impedance plots for the frequencies below ~10 Hz. This indicates towards the formation of a region which has thickness other than rest of the sample, similar to that of HfO_2 and TiO_2. During this stage, the impedance data fits well with the circuit #3 which represents existence of two regions with different thicknesses. This is supported by the presence of second time constant for impedance data on the 21st day. Since the impedance response of the ALD material in lower frequency regions tends to approach towards that of the bare electrode, it can be concluded that the new region formed has a thickness smaller than the initial thickness of the sample. The XPS data revealed that there is a change in peak position for the binding energy of the Zr3d on exposure to sweat solution for 21 days. This means that there is some chemical interaction between ALD ZrO_2 and the surrounding solution leading to dissolution of the material into the solution. This results in thinning of the ALD layer as indicated by the impedance data. As the decrease in thickness is not uniform throughout the ALD layer, localized thinning in selective regions of the sample could be suspected. This localized thinning in the ALD layer can be associated to the defects in the film which make the areas of the film in their proximity to be highly vulnerable to attack from the solution. Although,

ZrO_2 might have shown some degradation in sweat solution, it is found to be more stable than the other three ALD materials under consideration for this study.

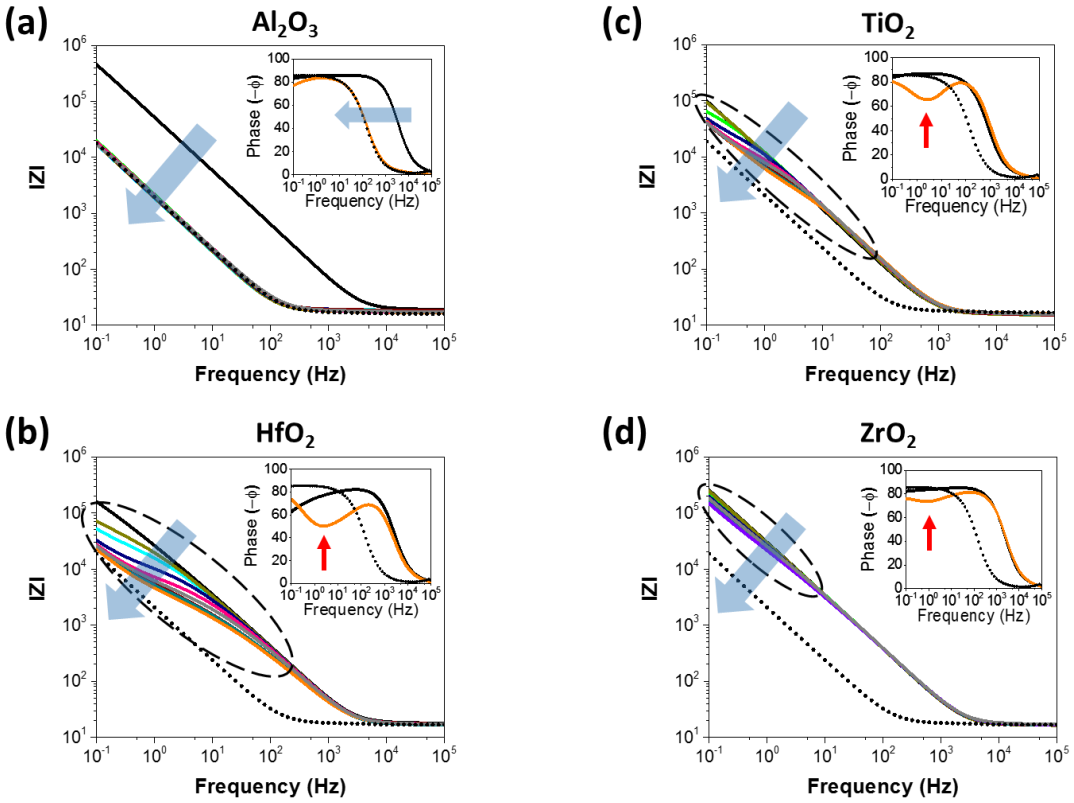

Figure 54 - EIS response in sweat solution for (a) Al_2O_3, (b) HfO_2, (c) TiO_2, and (d) ZrO_2 over a time period of 21 days. Dotted line represents impedance response from bare electrode. Blue arrows point towards the direction of measured data. Insets in the figure represent phase response for first and last measurement. Red arrow point towards the appearance of second time constant in the phase plots.

6.4 Conclusions

In this chapter, the potential of ALD films as an encapsulation material for bioimplants and wearable devices has been explored. Four ALD metal oxides, Al_2O_3, HfO_2, TiO_2 and ZrO_2, were used for testing. The cytocompatibility study, conducted using MTT cell proliferation test, on these materials established that all these materials are cytocompatible in nature in the short term, while the coatings are intact. Further, the chemical stability tests of the ALD films were conducted in PBS, saliva and sweat solutions using EIS. ALD Al_2O_3 was found to be unstable in all of the testing media as it tends to dissolve into the solution. ALD TiO_2 was found to be most stable in PBS solution, where no significant change in the material was observed after 21 days of exposure. ALD HfO_2 and ZrO_2 were not entirely unstable in PBS solution and had developed some defects with time. In saliva solution, ALD ZrO_2 was found to be most stable with no apparent degradation. ALD TiO_2 was also found to have good stability in saliva solution, however, it had shown few signs of degradation in the form of thinning of the ALD layer. ALD HfO_2 on the other hand degraded at much faster rate. In case of sweat solution, none of the ALD materials demonstrate complete stability. All the ALD films had some degradation. However, ALD ZrO_2 had the least degradation when compared to other ALD films, followed by ALD TiO_2. ALD HfO_2 had a much higher rate of degradation as compared to these two films. Based on the full assessment of ALD films in all the three biological solutions, the use of nanolaminate architecture consisting of alternating layers of TiO_2/ZrO_2 may provide long term stability for the implanted barrier material. Thus, this study further enhances the application of conformal ALD coatings with excellent dielectric properties for bio-MEMS applications in sensors, actuators, microfluidic, and wearable

devices. It must be noted that the cytocompatibility tests were conducted for a short time period, therefore, longer term in vitro and in vivo studies are required in future to confirm the use of ALD materials for aforementioned applications.

CHAPTER 7. STABILITY OF ALD FILMS IN IONIC SOLUTIONS

7.1 Introduction

As demonstrated in chapter 6, the use of ALD thin films can provide protection for electronics in harsh biological environments. This protection can also be extended to electronics placed in aqueous solutions that may have low pH or ionic species that are corrosive. Several studies have shown that ALD based barrier films can be used as a protective barrier in aqueous media for various materials.[70-72] However, most of the studies conducted regarding the same are limited by their short duration of testing. Although a material may appear to be corrosion resistant, and therefore a good barrier material over a short duration test, it may not actually be stable under long durations of exposure to the aqueous conditions. Consequently, it becomes critical to test the chemical stability of the barrier material itself and monitor any changes in the material with time. Another possibility is that the material may be completely stable in a particular solution, but due to the presence of pores in the material, it allows the permeation of ionic species through it leading to the corrosion of the underlying material. This calls for the use of techniques which give information into the rate of chemical degradation or that have the ability to detect slight changes in the barriers in order to yield insight into the stability of ALD barriers. It would also be beneficial to have insight into the nature of corrosion such as the etching of the film, induced porosity, cracking and formation of localized pinholes.

In this chapter, the chemical stability of low temperature (100°C) PEALD deposited metal oxides in different ionic solutions including NaCl, sea water, H_2SO_4 (pH4) and HCl (pH4) has been explored. These ionic solutions were chosen to cover a variety of conditions of exposure for the barrier films such as Cl^- ions, SO_4^{2-} ions and low pH. Metal oxides used for this study include Al_2O_3, HfO_2, TiO_2 and ZrO_2. EIS was employed to study the chemical stability while monitoring the changes in the ALD films soaked in different ionic solutions for 21 days. Equivalent electrical circuits were used to understand the mechanism of degradation at different stages. A complimentary technique to EIS to detect the corrosion stability of ALD films was used which involved the use of photoluminescence (PL) test of ALD coated ZnO samples. SEM and XPS analysis were conducted on the samples to determine any changes in their physical and chemical state while EIS models were used to help understand the degradation mechanism.

7.2 Experimental

7.2.1 EIS and ZnO photoluminescence test

ALD films were deposited on electrode and ZnO coated substrates as described in section 6.2.1. The setup and electrode used for EIS testing are shown in Figure 24 and Figure 25, respectively. For testing the chemical stability of ALD films in ionic solutions, EIS tests were conducted as described in section 3.4. The samples were soaked in 3.5 % NaCl, sea water, H_2SO_4 (pH4) and HCl (pH4) solutions. Lab grade NaCl and sea water were purchased from The Science Company and Top Fin, respectively. HCl and H_2SO_4 were purchased from J. T. Baker.

The capacity of ALD materials to protect against the diffusion of species through the coated barrier material can be determined using ZnO photoluminescence (PL) test. ZnO PL tests have been used previously in the study for improving lifetime of ALD Al_2O_3 films in aqueous media.[67] In this technique, ZnO, a wide bandgap semiconductor material, which shows PL on exposure to UV radiation is used as a sensor.[165] ALD ZnO is extremely unstable in aqueous solution and tends to dissolve in it.[166] For this test, the barrier material is coated on ZnO which is deposited on a Si substrate and dipped into the testing media. Thus, if a barrier layer is able to protect the ZnO, then a PL signature is detected from the ALD coated ZnO sample. The degradation of the ZnO PL intensity or the absence of the PL peak tends to indicate that corrosion of the ZnO is occurring and thus the failure of the barrier film.

The samples for PL measurements were prepared on silicon substrates. Three cycles of ALD Al_2O_3 were first deposited on silicon followed by the deposition of 100 cyc of ZnO at 250°C. Diethyl zinc (DEZ) was used as a precursor for ZnO. The initial layer of Al_2O_3 acts as a nucleation layer for the deposition of ZnO. After this, ALD metal oxides were deposited on top of ZnO at 100°C with the thickness and parameters shown in Table 5. PL from the samples was detected using JY Horiba LabRAM HR800 system with excitation source of 325 nm He-Cd Laser. Schematic of the setup used to measure the PL from ZnO samples is shown in Figure 55(a). PL measurements were taken at regular intervals of 3 days for a total of 21 days. In between measurements, the samples were soaked in the testing media as shown in Figure 55(b).

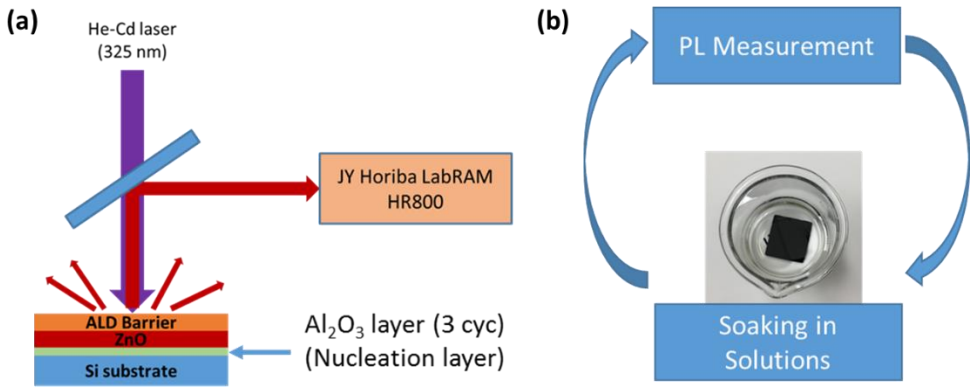

Figure 55 - (a) Schematic of setup for PL measurement from ZnO, (b) Exposure of ZnO samples to different solutions.

7.2.2 Materials characterization

Surface images of the samples were taken using a Hitachi SU8230 scanning electron microscope (SEM). Chemical characterization of the ALD coated ZnO samples used for PL measurements were conducted with X-ray photoelectron spectroscopy (XPS) on a Thermo Scientific K-Alpha X-ray photoelectron spectrometer system with a monochromatic Al Kα X-ray source (hν = 1486.6 eV). Depth profiles were taken by etching the top surface with Ar^+ ion sputtering for 10 s in each step. The total number of etching steps was determined by the appearance of Si as it was the last layer in the samples. All XPS spectra were shifted with respect to the adventitious carbon (C1s) peak at 284.8 eV found on the samples.

7.3 Results and discussion

7.3.1 ALD films in NaCl solution

Bode plots for the ALD films in 3.5% NaCl solution are shown in Figure 56. Phase change plots for initial and final measurements are presented in the insets of the figures. In case of ALD Al_2O_3, the inset in the Figure 56(a) for initial measurements shows capacitive behavior with high impedance in the low frequency region. At this stage, the impedance response from ALD Al_2O_3 follows circuit #2 as shown in Figure 27(b), indicating uniform deposition of the film. However, there is a gradual shift in the impedance response from the ALD Al_2O_3 material towards lower frequency with increase in exposure time. The gradual shift in impedance towards that of the bare electrode signifies that there is dissolution of ALD Al_2O_3 into the solution. As the last measurement still does not overlap with that of the bare electrode, and all the impedance measurements following circuit #2 as shown in Figure 27(b), it means that there is still some ALD material remaining on the substrate surface. This implies that ALD Al_2O_3 is not chemically stable in NaCl solution.

Figure 56(b) shows bode plots for ALD HfO_2 in the NaCl solution. The impedance measurement data initially fits well with circuit #2, as shown in Figure 27(b), indicating uniform deposition of the film. However, with continued exposure of the film to the NaCl solution, the impedance response of ALD HfO_2 changes with time. In the frequency range below ~10 Hz, there is a continuous widening in the impedance response with lower frequency impedance moving towards that of the bare electrode. From the second measurement onwards, the impedance data follow circuit #3, as shown in Figure 27(c), implying that there is non-uniform thinning in the ALD layer. This is supported by the

appearance of a second time constant in the phase plot when compared to the initial measurement. Thus, ALD HfO_2 gets partially dissolved into the solution, resulting in the thinning of the ALD layer in some localized regions. This non-uniform decrease in the thickness of the material means that there is selective etching or removal of ALD HfO_2 which could result from the presence of highly vulnerable sites near the proximity of pinholes and other defects.

Figure 56(c) and (d) show bode plots for ALD TiO_2 and ZrO_2 in the NaCl solution, respectively. There is no significant change in the impedance response of both of these materials throughout the testing period. The impedance response of both of these materials followed circuit #2, as shown in Figure 27(b), indicating uniform deposition of the ALD films on the substrate. The phase response of the materials for the initial and final measurements overlap with each other indicating that there is minimal degradation in the materials during the testing period. This implies that both, ALD TiO_2 and ZrO_2 are quite stable in the NaCl solution.

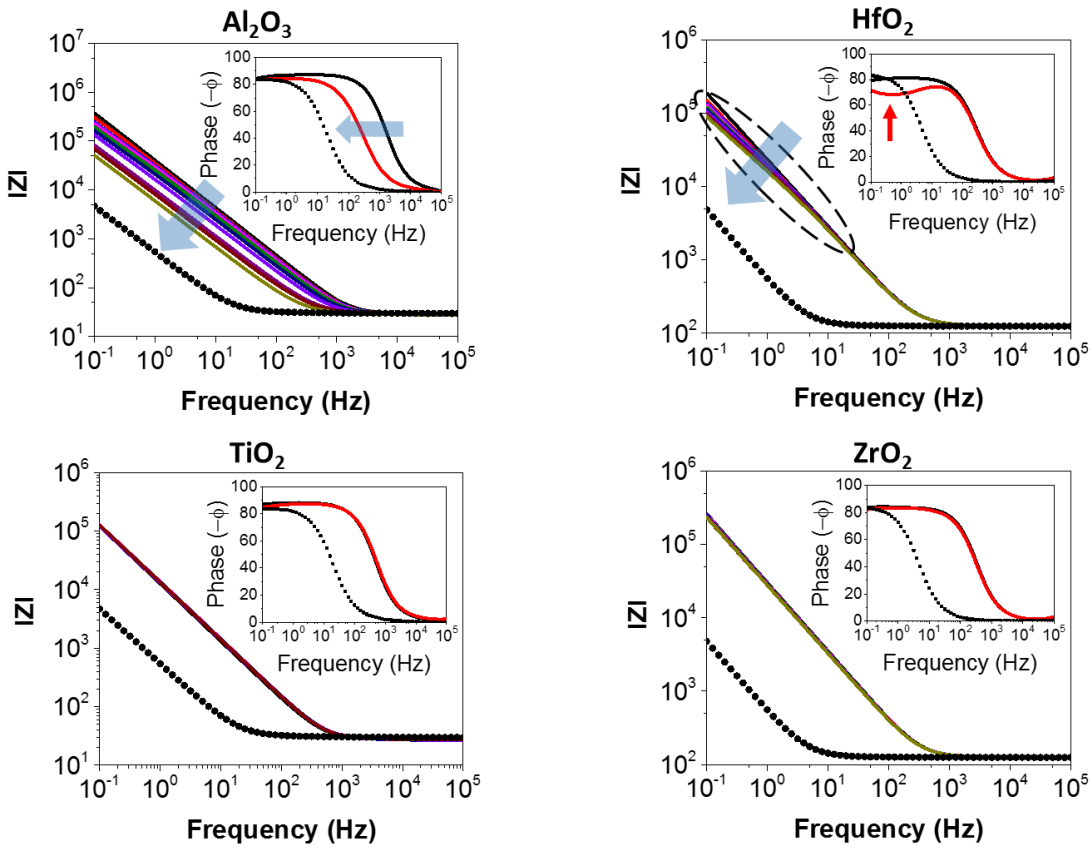

Figure 56 - EIS response in 3.5% NaCl solution for (a) Al_2O_3, (b) HfO_2, (c) TiO_2, and (d) ZrO_2 over a time period of 21 days. Dotted line represents impedance response from bare electrode. Blue arrows point towards the direction of measured data. Insets in the figure represent phase response for first and last measurement. Red arrow point towards the appearance of second time constant in the phase plots.

7.3.2 ALD films in sea water

Bode plots for the ALD films in sea water are shown in Figure 57 with phase change plots for initial and final measurements presented in the insets of the respective figures. For ALD Al_2O_3 and HfO_2, the impedance response in sea water is similar to that in NaCl solution. Impedance data for both of these materials fits well with circuit #2 for the initial measurements indicating uniformly deposited film. However, on exposure to sea water,

ALD Al_2O_3 tends to dissolve at a much higher rate when compared to its dissolution in NaCl solution. The impedance data and phase plots for measurements on the 21st day overlap with each other while following circuit #1, as shown in Figure 27(a), indicating that there is complete removal of ALD Al_2O_3 from substrate surface. This means that, similar to when immersed in NaCl, ALD Al_2O_3 is not stable in sea water. ALD HfO_2 on the other hand showed enhanced stability. However, similar to that in the NaCl solution, there is a continuous widening in the impedance plots in lower frequency region (~10 Hz) indicating that there is partial degradation of ALD HfO_2 film. There is the appearance of a second time constant in the phase response for measurements on the 21st day. Also, the impedance data fits well with circuit #3, as shown in Figure 27(c), indicating the formation of thinner regions as compared to initial thickness of the film. This partial degradation can be due to accelerated removal of the ALD HfO_2 material from the proximity of defect sites.

Figure 57(c) shows bode plots for ALD TiO_2 in NaCl solution. There is no apparent change in the impedance response of the material in sea water throughout the testing period. The impedance response from ALD TiO_2 overlapped following circuit #2, as shown in Figure 27(b), indicating uniformly deposited ALD film on the substrate. The phase response of the materials for initial and final measurements also overlapped indicating that there is minimal degradation in the materials during the testing period. This implies that ALD TiO_2 is highly stable in sea water.

Figure 57(d) shows bode plots for ALD ZrO_2 in sea water. The impedance response from the material reveals slight widening in the low frequency region indicating partial degradation of the ALD film near the defect sites. However, this widening is much smaller as compared to that of ALD HfO_2 in NaCl solution and sea water, implying that ALD ZrO_2

is much more stable than ALD HfO_2 in sea water. This is also supported by the appearance of gap between initial and final phase plots due to the introduction of second time constant. Since the magnitude of degradation is small, that second time constant is not clearly seen in the inset of Figure 57(d).

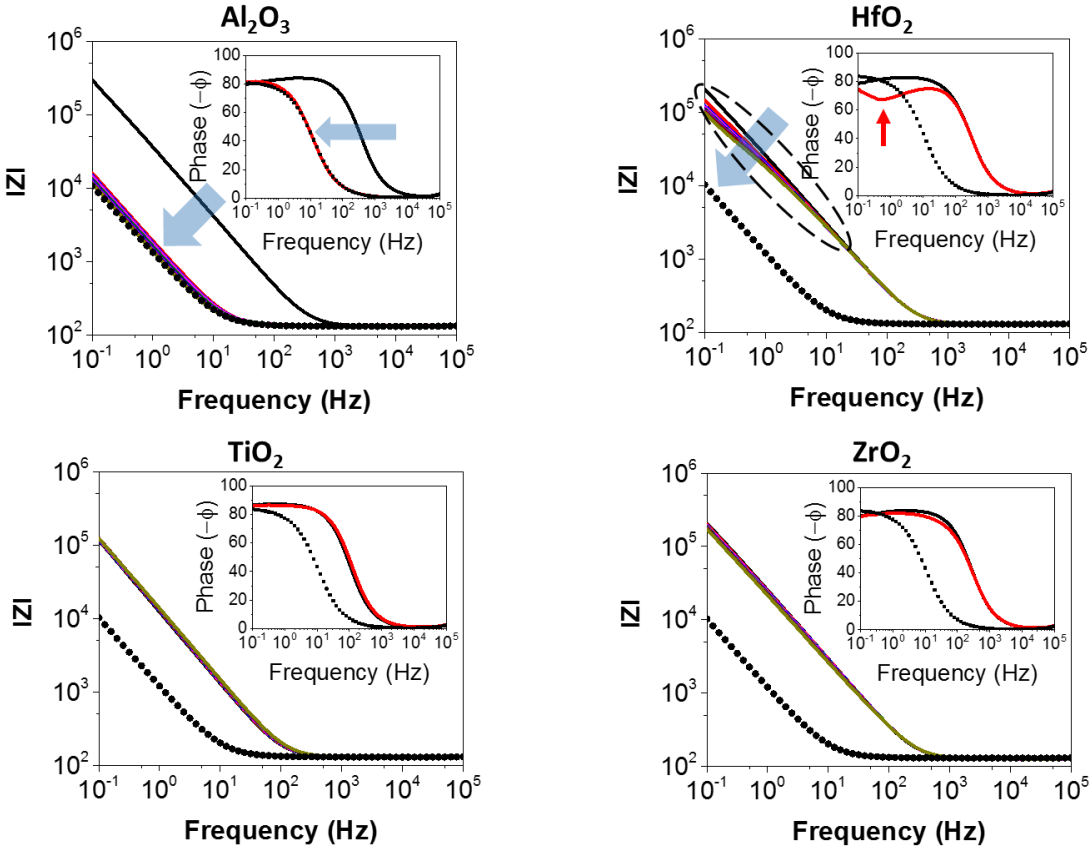

Figure 57 - EIS response in sea water for (a) Al_2O_3, (b) HfO_2, (c) TiO_2, and (d) ZrO_2 over a time period of 21 days. Dotted line represents impedance response from bare electrode. Blue arrows point towards the direction of measured data. Insets in the figure represent phase response for first and last measurement. Red arrow point towards the appearance of second time constant in the phase plots.

7.3.3 ALD films in H_2SO_4 and HCl

Bode plots for the ALD films in HCl (pH4) and H_2SO_4 (pH4) solutions are shown in Figure 58 and Figure 59, respectively. Phase change plots for the initial and final measurements are presented in the insets of respective figures. The initial impedance responses for all of the ALD materials in HCl and H_2SO_4 solutions fit well with circuit #2, as shown in Figure 27(b), indicating that all of the ALD films were uniformly deposited, initially. In the case of ALD Al_2O_3, on exposure to HCl and H_2SO_4 solutions, there is rapid degradation in the material. All measurements taken after one day of exposure to the acidic solutions demonstrate an impedance and phase response that is consistent with that of a bare electrode. This implies that there is complete removal of ALD Al_2O_3 from the substrate surface within one day of exposure to the acidic solutions indicating that ALD Al_2O_3 is highly unstable in such environment.

ALD HfO_2, TiO_2 and ZrO_2 on the other hand showed much enhanced stability. Throughout the experimental period, there is no noticeable change in the impedance response of the materials, as shown in Figure 58 and Figure 59. This is also supported by the overlapping of phase plots for first day and last day measurements. Throughout the experimental period, the impedance response from these material followed circuit #2, as shown in Figure 27(b), indicating a uniformly deposited ALD film that did not change with time. Thus, ALD HfO_2, TiO_2 and ZrO_2 can be considered as stable in acidic environments.

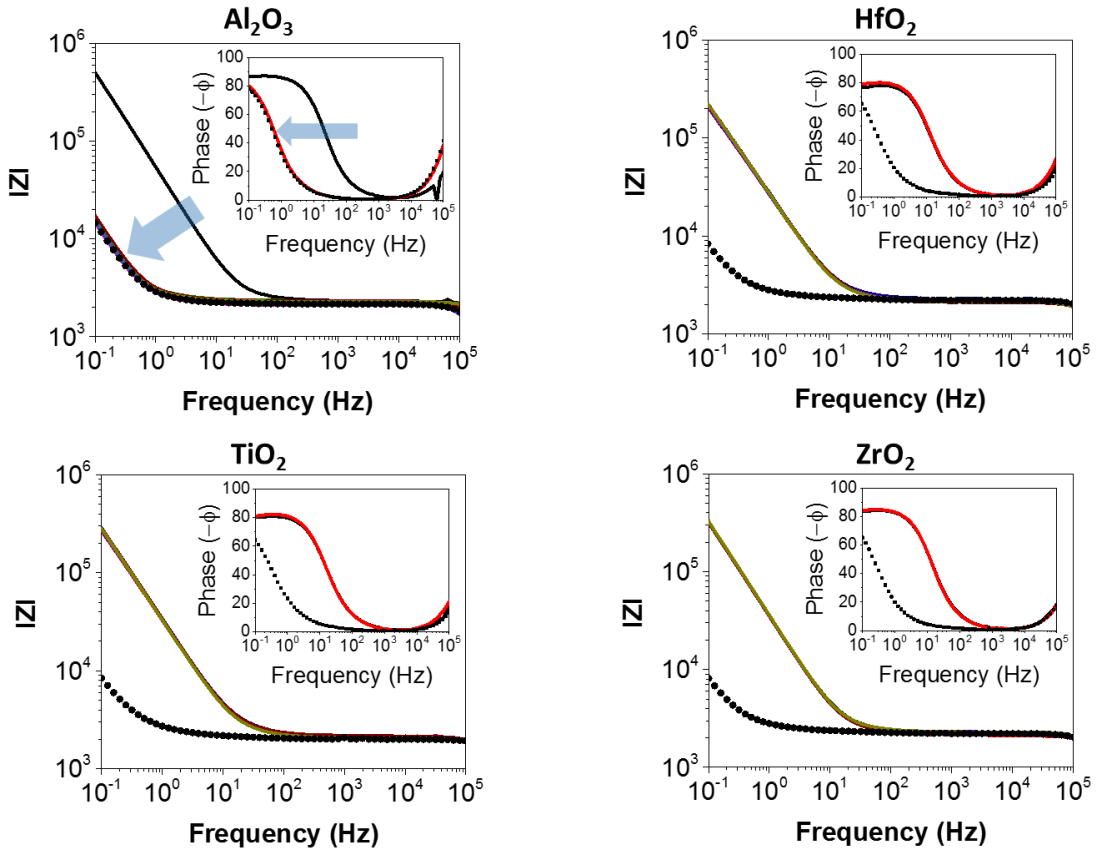

Figure 58 - EIS response in HCl (pH4) for (a) Al_2O_3, (b) HfO_2, (c) TiO_2, and (d) ZrO_2 over a time period of 21 days. Dotted line represents impedance response from bare electrode. Blue arrows point towards the direction of measured data. Insets in the figure represent phase response for first and last measurement. Red arrow point towards the appearance of second time constant in the phase plots.

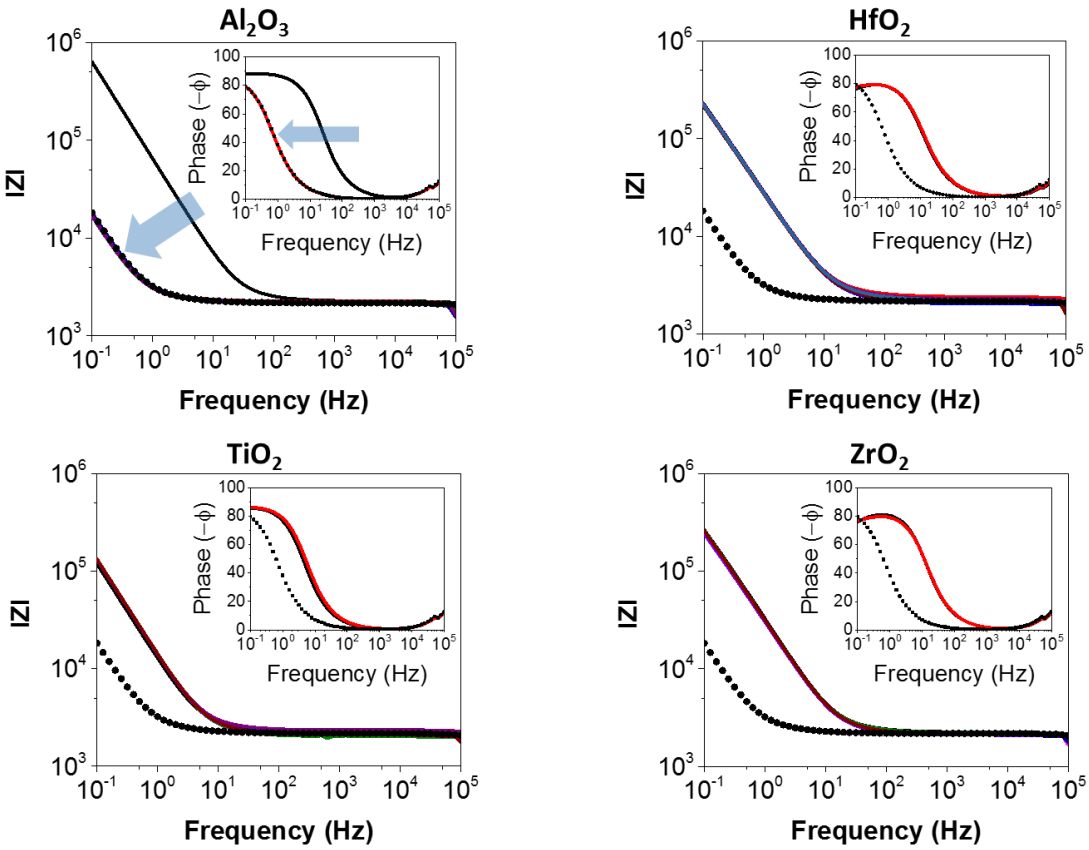

Figure 59 - EIS response in H_2SO_4 (pH4) for (a) Al_2O_3, (b) HfO_2, (c) TiO_2, and (d) ZrO_2 over a time period of 21 days. Dotted line represents impedance response from bare electrode. Blue arrows point towards the direction of measured data. Insets in the figure represent phase response for first and last measurement. Red arrow point towards the appearance of second time constant in the phase plots.

7.3.4 ZnO photoluminescence test results

Following EIS tests, ZnO PL tests were further conducted with all the ALD materials to determine their ability to protect the coated material, in this case ALD ZnO. The PL from the ALD coated ZnO samples were taken at regular intervals of 3 days for a total of 21 days. The PL spectra obtained for the samples in different solutions are shown in Figure 60. Figure 60(a) shows the PL spectra of ALD Al_2O_3 coated samples. Initial PL

measurement of the sample shows characteristic ZnO PL peak. However, no PL signal could be obtained for ALD Al_2O_3 coated samples in any of the ionic solutions after exposing them for 3 days. This shows that ALD Al_2O_3 is unable to protect ZnO. The XPS data taken for Al2p peaks for ALD Al_2O_3 coated samples in ionic solutions is shown in Figure 61(a). A clear Al2p peak was observed for the initial ALD Al_2O_3 coated samples, before exposure to any of the solutions. From the ALD Al_2O_3 coated samples exposed to NaCl solution and sea water for 21 days, a very weak intensity peak for Al2p is observed indicating that most of the material is removed from the surface with ALD Al_2O_3 remaining on in traces. However, in case of HCl and H_2SO_4 solutions, there was no Al2p signal from the sample surfaces indicating that ALD Al_2O_3 is completely dissolved into these solutions. This implies that ALD Al_2O_3 is highly unstable in ionic solutions, which is consistent with the observations from the EIS study. Therefore, ALD Al_2O_3 cannot be used as a protective barrier in such environments.

The PL spectra obtained from ALD HfO_2 coated samples soaked in different ionic solutions for 21 days are shown in Figure 60(b). The appearance of PL peaks after 21 days in the NaCl solution and sea water indicates that ZnO layer is still intact. This means that ALD HfO_2 can protect the coated layer in NaCl solution and sea water. XPS spectra of Hf4f obtained for ALD HfO_2 coated samples are shown in Figure 61(b). A shift towards lower binding energy of Hf4f is observed for all the samples which indicates that less electronegative chemical environment is created, possibly by the removal of oxide cation leading to the formation of chloride and sulfate salts of Hf. These species can be soluble in aqueous media which can ultimately lead to the removal of HfO_2 from the sample surface. EIS study conducted on ALD HfO_2 indicates that there is partial degradation of the ALD

HfO_2 layer in NaCl solution and sea water during the same testing period. Still the PL from ZnO could be obtained which indicates that the degradation in the HfO_2 was localized to certain areas leading to the formation of defects. However, the defects formed were confined within the thickness of the ALD HfO_2 layer and did not go through it. Thus, ALD HfO_2 could effectively protect the coated material in NaCl solution and sea water.

Although the EIS study indicated that ALD HfO_2 is stable in HCl and H_2SO_4, PL was not observed from ZnO samples after a few days of exposure. For both solutions, PL was observed for the first 6 days. On the 9^{th} day, some regions of the sample showed PL whereas other regions did not show any PL. SEM images reveal that there is appearance of two different regions on the sample soaked in HCl solution, as shown in Figure 62(a). Two regions appear in the sample images with different contrast. Similar regions were formed in case of HfO_2 coated sample soaked in H_2SO_4 solution as well. In the following text, the lighter regions are regions where ZnO was etched and the dark regions are regions where ZnO exists. It is seen from the SEM image that the light regions consists of large number of cracks, whereas no crack could be found in the dark region. As shown in Figure 62(b), PL could be obtained from the dark regions only, whereas there was no PL from light region. This means that ZnO was removed from the light regions indicating partial degradation of the sample at this stage. Figure 62(c) and (d) show the depth profile for dark and light regions, respectively. The presence of Zn between Hf and Si peaks in Figure 62(c) indicates that the ZnO layer is still present in the dark regions. The absence of Zn signal in the dark region shows that the ZnO layer has been completely removed from the light regions. However, the ALD HfO_2 layer deposited on top of the ZnO is still present. It can therefore be concluded that the cracks in the ALD HfO_2 layer that were seen in SEM images

must have led to the penetration of the ionic species from the solution to the ZnO layer leading to its degradation as shown in Figure 64. Thus, the mechanism of degradation of the ALD HfO_2 layer in HCl and H_2SO_4 solutions could be considered similar to pitting corrosion where there is the formation of localized pits through which solution can penetrate and go across the protective layer while damaging the coated material. These pits are formed at the region of high vulnerability of the protective coating. Consequently, the area of the light region kept on increasing with continuous exposure of samples to HCl and H_2SO_4. By the end of the testing period of 21 days, the light region covered the entire sample and no PL was observed, as shown in Figure 60(b), due to complete removal of ZnO. No specific crack formation could be observed through the SEM images. However, there might be cracks in the form nanoscale defects where there is high stress concentration due to residual tensile stress (~350 MPa) in the ALD HfO_2 layer. The EIS data have shown that ALD HfO_2 is stable in HCl and H_2SO_4 solution, still it is not able to protect the ZnO layer. This means that despite showing stability through EIS testing, ALD HfO_2 coating can still allow permeation of some ionic species through the defects created when it is soaked in these solution, and therefore, is not a good candidate to be used as a barrier in low pH conditions. This also shows that it is necessary to use more than one type of test to determine the stability and corrosion mechanisms of the ALD barriers.

Figure 60(c) and (d) show the PL spectra for ALD TiO_2 and ZrO_2, respectively, in NaCl, sea water, HCl and H_2SO_4 solutions. All the samples show the PL from ZnO indicating that these two ALD materials could very well protect the coated layer. XPS surface scans for Ti2p, shown in Figure 61(c), reveal that there is a shift towards higher binding energy which can be explained by the increase in oxide species in the TiO_2 layer.

It is possible that during the deposition of TiO_2 films using ALD, unreacted Ti attached to hydrocarbon ligands from the precursors can still remain in the layer. These species can react with the surrounding media while forming oxides and thereby increasing the concentration of oxide species in the TiO_2 layer. Since the resultant species is oxide, it is not soluble in the surrounding media as seen in case of ALD HfO_2 which makes ALD TiO_2 stable. In case of ALD ZrO_2, the XPS surface scans of Zr3d, shown in Figure 61(d), almost overlap with the initial state indicating that there is minimal change in the chemical state of the material. This implies that ALD ZrO_2 is chemically stable in the tested solutions. XPS depth profiles for ALD TiO_2 and ALD ZrO_2 coated samples in HCl solution for 21 days are shown in Figure 63(a) and (b), respectively. Both, Figure 63(c) and (d) clearly show that the ZnO layer is intact between the ALD barrier layers in HCl solution. Similar XPS depth profiles were obtained for ALD TiO_2 and ALD ZrO_2 in NaCl, sea water and H_2SO_4 solutions (not shown). The EIS study revealed that ALD TiO_2 and ZrO_2 were stable in all the ionic solutions used for this study. Thus, from the EIS study and ZnO PL test, it is concluded that ALD TiO_2 and ALD ZrO_2 are stable in the tested ionic solutions, and also, can act as excellent barriers in such environments.

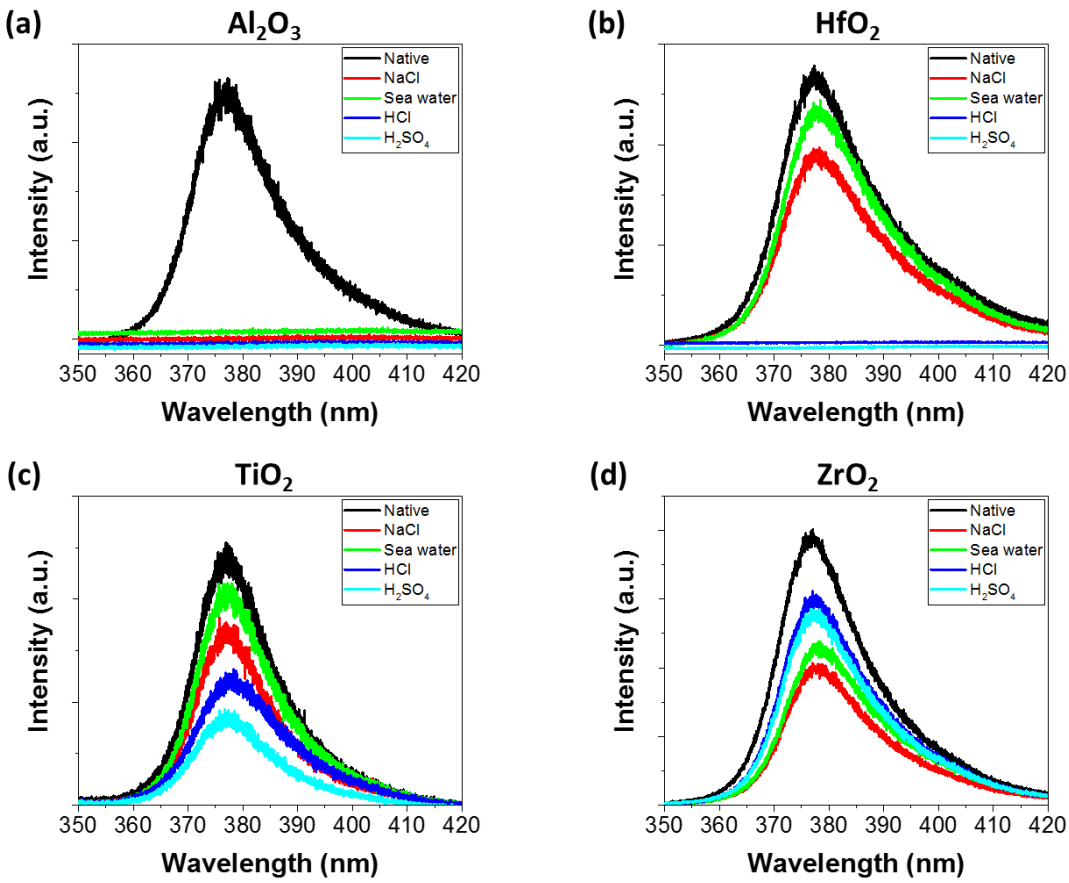

Figure 60 - PL from ZnO substrates coated with (a) Al_2O_3, (b) HfO_2, (c) TiO_2, and (d) ZrO_2 before and after soaking for 21 days.

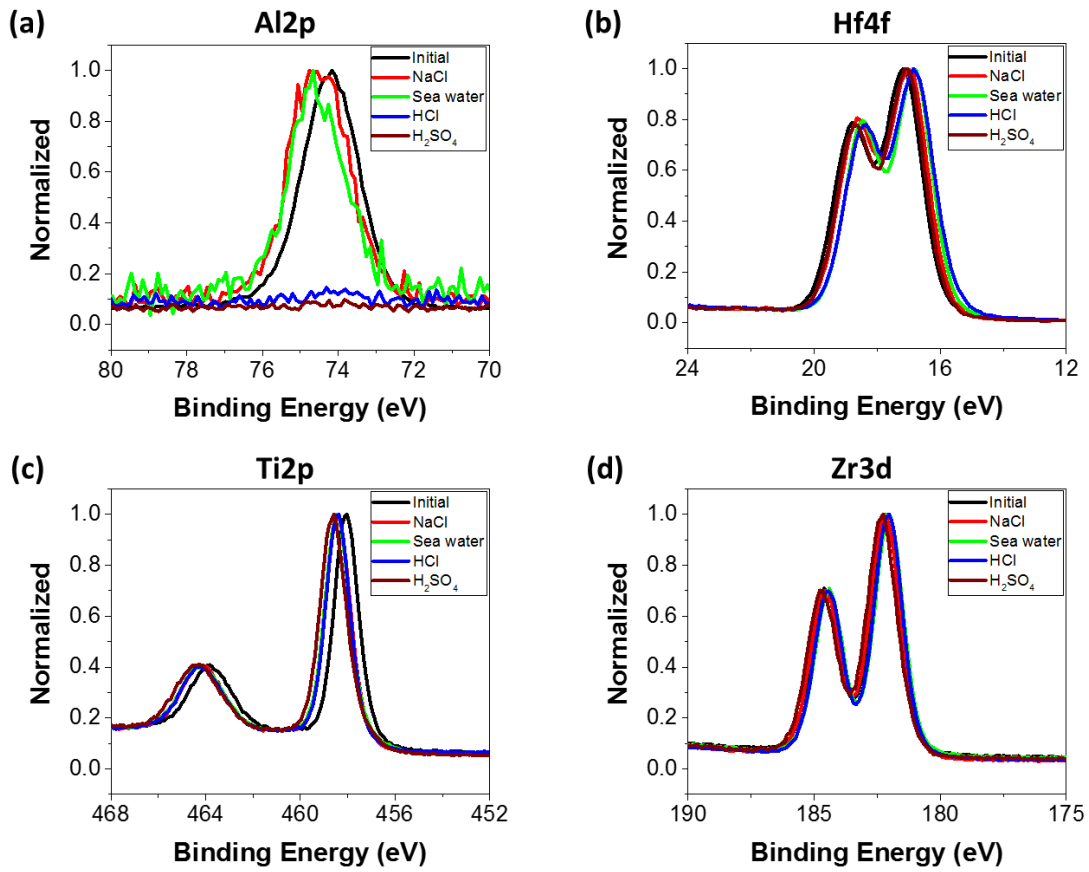

Figure 61 - Surface scan of (a) Al_2O_3, (b) HfO_2, (c) TiO_2, and (d) ZrO_2 coated samples using XPS.

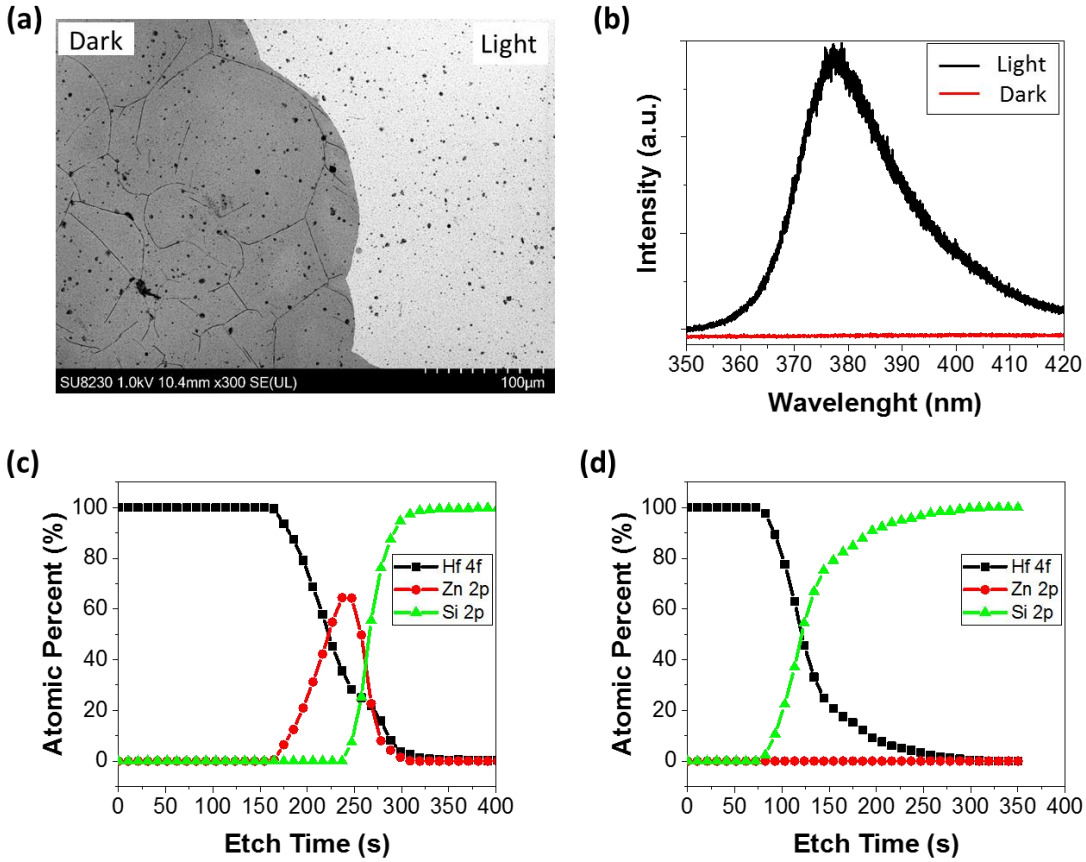

Figure 62 - (a) Optical image of HfO_2 coated ZnO sample after 10 days HCl solution, (b) PL from dark and light regions, (c) XPS depth profile of light region, (d) XPS depth profile of dark region.

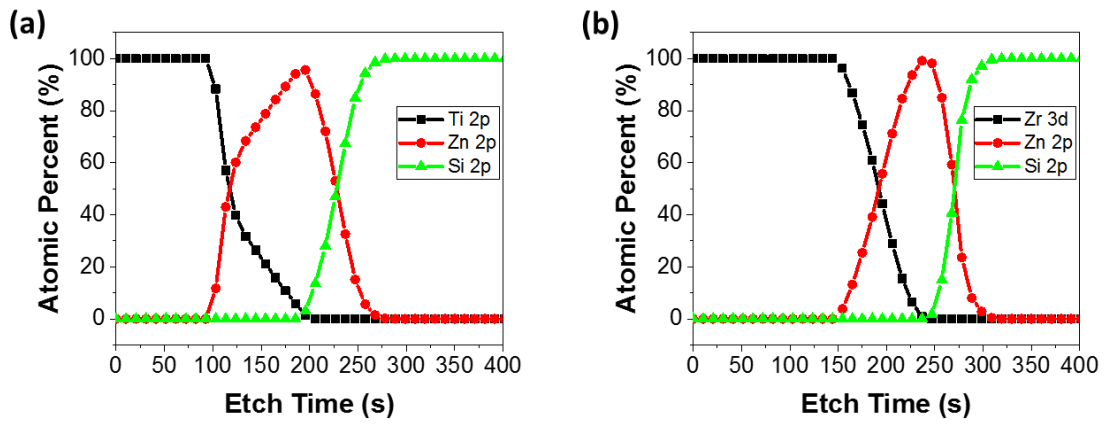

Figure 63 - XPS depth profiles for (a) TiO_2 and (b) ZrO_2 coated ZnO samples in HCl after 21 days.

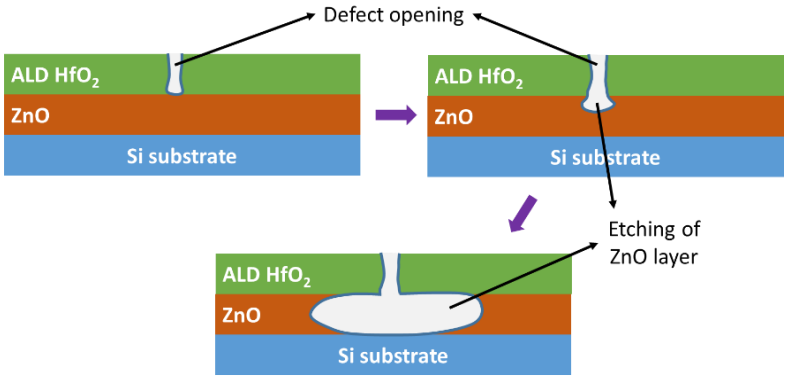

Figure 64 - Pitting type corrosion of oxide films.

7.4 Conclusions

The stability of ALD Al_2O_3, HfO_2, TiO_2 and ZrO_2 films deposited at 100°C have been explored in a variety of environments to determine their ability to be used for chemical protection and as diffusion barriers. The ionic solutions used for testing were 3.5% NaCl, sea water, HCl (pH4) and H_2SO_4 (pH4). EIS was first used to determine the stability of ALD materials in different ionic media. It was found that ALD Al_2O_3 was highly unstable in all the solutions which was also confirmed by PL experiments. ALD HfO_2 shows some degradation when exposed to NaCl and sea water due to localized attacks near defect sites. However, when exposed to HCl and H_2SO_4 solutions, no apparent degradation was observed which may seem to indicate some level of stability of HfO_2 in low pH conditions. When combined with PL measurements, it is clear that the HfO_2 films are not sufficient as a barrier film in the ionic solutions due to localized degradation that can lead to the permeation of ionic solution through localized defects. Such defects were observed in the form of cracks in the ALD HfO_2 films which enabled the corrosion of a sensitive ZnO underlayer. Finally, ALD TiO_2 and ZrO_2, showed no degradation in any of the solutions by EIS or PL, indicating that they are highly stable in the testing media. Overall, these experiments show that the testing of the chemical stability and barrier suitability of low temperature grown ALD metal oxides cannot be determined by a single method. However, the combined approach of EIS and PL experiments provide unique insights into the suitability of the films as barriers in harsh environments involving ionic solutions.

CHAPTER 8. INTEGRATION OF ENCAPSULATION WITH PEROVSKITE CELLS

8.1 Introduction

This chapter deals with the integration barrier films with the perovskite solar cells (PSCs). As described in previous sections, barrier films are used to protect the devices sensitive to the environmental conditions during their operation. Similar to organic electronic devices, PSCs are also sensitive to the atmospheric species, namely water vapor and oxygen. For any commercial application, PSCs should be able to function in open atmospheric conditions for long durations. There should not be significant degradation in their performance in their designated period of usage.

The lifetime and reliability of PSCs in open atmospheric conditions can be increased by using barrier encapsulations that can prevent the ingress of moisture and oxygen from the atmosphere to the active regions of the device. As described earlier, two kinds of methods can be used for the encapsulation of PSCs, direct and indirect encapsulations. However, device compatibility with the encapsulation processes is a major issue. For example, while using direct encapsulation method, ALD metal oxides need to be deposited directly on the PSCs. Since the PSCs are unstable at high temperatures, thermal ALD is not a viable option.[29] Plasma assisted ALD is not an option either as the PSCs are also sensitive to the plasma. With the development of ALD technology, thermal ALD depositions can be carried out at temperatures as low as 100°C. However, depositions

at this temperature often require long exposure times for the PSCs which again is detrimental to their stability.[29]

Another option for the encapsulation is the use of indirect encapsulation methods. In this process, any condition can be used for the fabrication of the barrier film since the device and barrier are prepared separately. For the encapsulation, the barrier and PSCs are sandwiched together using an adhesive. During this process, PSCs come in direct contact with the adhesive material which can react with the PSCs leading to their degradation even before being exposed to environmental species. Therefore, in this chapter, the concept of using PECVD SiNx as a chemical resistance buffer layer between the PSC and adhesive and barrier has been introduced. The performance of the PSCs first protected with the buffer layer and then encapsulated using indirect encapsulation has been investigated with time.

8.2 Experimental

In this section, the application of hybrid barrier films has been demonstrated by encapsulating perovskite cells using indirect encapsulation method. The cells were received from Dr. Joseph Berry of the National Renewable Energy Laboratory (NREL). The device architecture is FTO/TiO_2/MAPI/Spiro/MoOx (15 nm)/Al (~200 nm). The TiO_2 consists of thin compact layer followed by a mesoporous layer of ~130 nm thickness. Methyl Ammonium Lead Iodide (MAPI) films were deposited using the method described by Ahn *et al*.[167] There were several issues related to cell design and encapsulation method which have been addressed in the following section. The barrier films were prepared

separately by depositing ALD films on commercially available 3M Ultra Barrier Solar Film.

8.2.1 Protection of aluminium electrodes

As received cells contain aluminum electrodes as shown in Figure 65(a). If aluminum is exposed to atmosphere for a long time, it forms an which is insulating in nature. This leads to poor conductivity of the electrodes and eventually poor performance of the cells. To avoid this, Cr and Au were deposited on Al electrodes with a thickness of 10 nm and 50 nm, respectively, using E-beam evaporator (Denton Explorer) as shown in Figure 65(b). This thickness of Cr/Au is expected to prevent the oxidation of Al upon exposure of devices to the atmosphere or controlled environmental conditions. Also, this extra layer of metal provides strength to the electrodes against wear while making contacts during measurements.

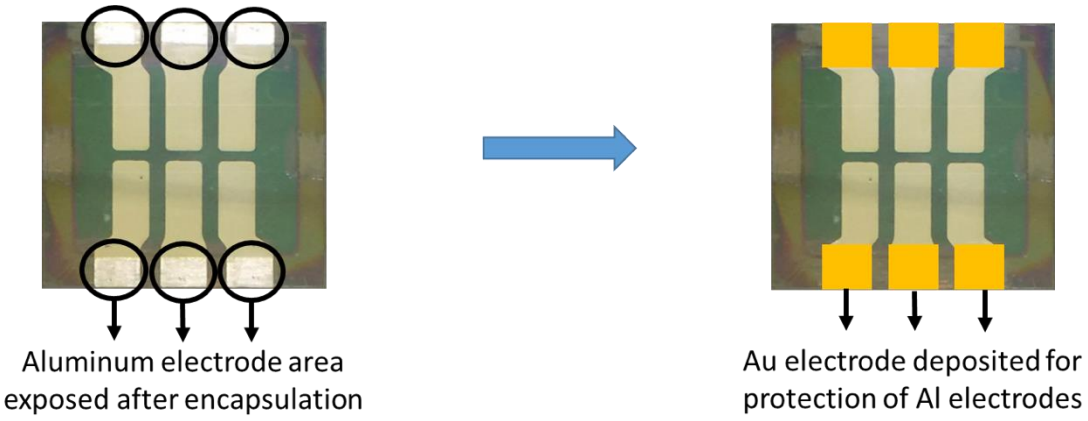

Figure 65 - Deposition of Au electrodes on exposed Al electrodes to increase the robustness and to protect them from oxidation in open atmospheric condition.

8.2.2 Extension of electrodes

As pointed out in Figure 66(a), a limited area of FTO electrode is exposed for making electrical contacts which is located along the side and middle of the devices. During encapsulation, it is very difficult to encapsulate barrier only on the active area while leaving FTO exposed for making electrical contacts. Hence, a thin strip of Cr/Au (10 nm/50 nm) was deposited along the sides of the cells such that it covers the FTO and reaches to the end on both sides of the cells, as shown in Figure 66(b). This increases accessible electrode area and leaves the center area of the cells to be encapsulated freely even after covering the FTO electrode. The contacts are made with Au exposed at all four corners of the devices.

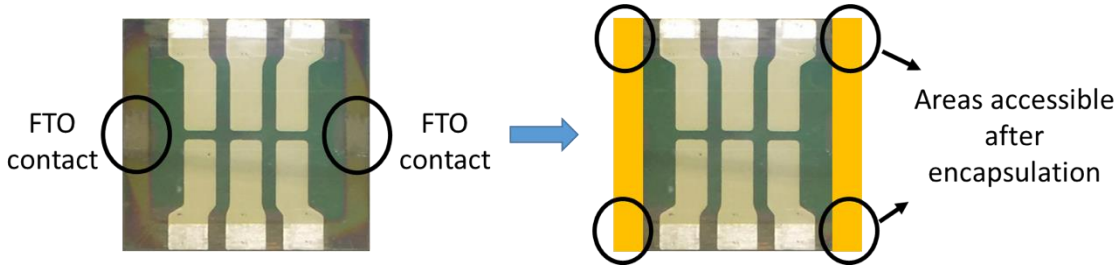

Figure 66 - Deposition of Au electrodes on FTO electrodes along sides of the devices.

8.2.3 Buffer layer before application of adhesive tape

The adhesive used is UV curable and contains getter materials. During initial measurements, the adhesive was applied directly over the devices. Due to the interaction between the adhesive and the perovskite cell material, change in color of the perovskite cells was observed and the cell degraded completely in a short while. This occurred whenever the devices were in direct contact with the adhesive. To avoid any kind of

reaction or physical interaction between adhesive and perovskite cells, a thin layer of PECVD SiNx is used in the form of buffer layer. PECVD SiNx with the thickness of 500 nm was deposited on all of the devices at 110°C prior to encapsulation. Since the deposition was carried out in a PECVD chamber, the devices were exposed to the temperature of 110°C for about 70 min. This duration of exposure to high temperature is not expected to negatively impact the devices. To confirm this, the efficiency measurements were taken before and after the deposition of PECVD SiNx. During the deposition of SiNx, the outer area of the electrodes was covered with a PET mask to protect them from SiNx deposition, as shown in Figure 67. This outer region of the electrodes is required to make electrical contacts.

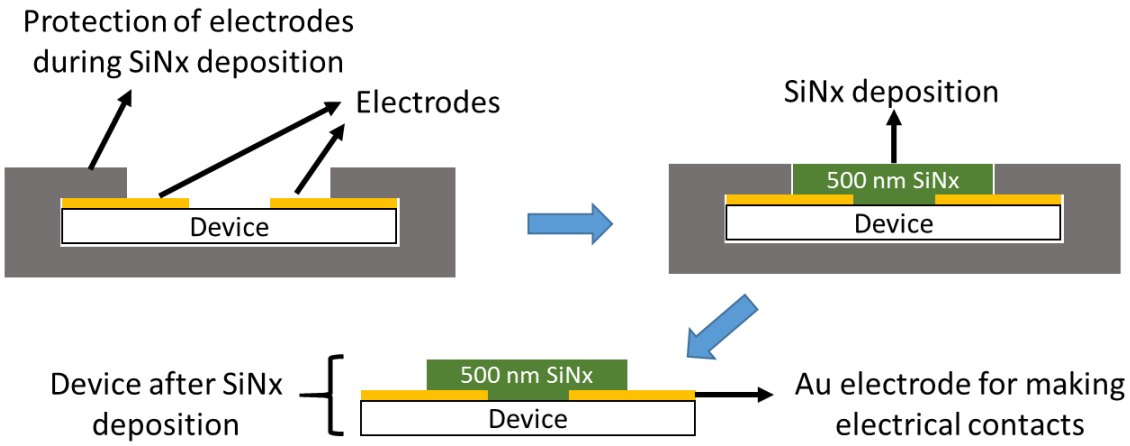

Figure 67 - Schematic of protection of electrodes during PECVD SiNx deposition.

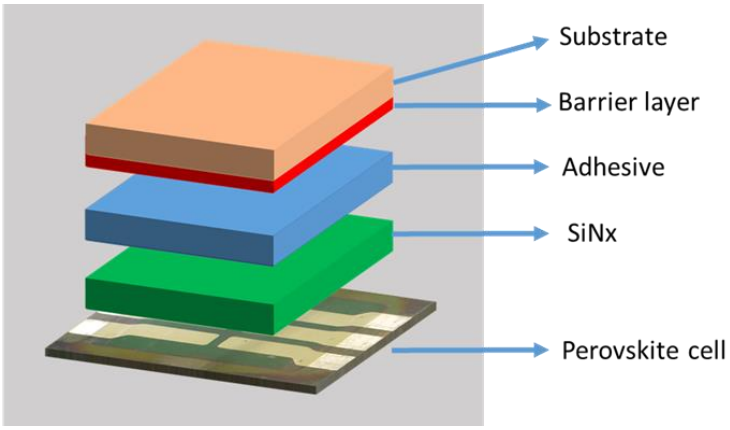

Figure 68 - Schematic of device encapsulation with different layers.

8.2.4 Device encapsulation and efficiency measurements

As described above, PECVD SiNx was deposited on the perovskite cells as a buffer layer. Barrier films were prepared separately by depositing 100 cyc Al_2O_3 followed by 100 cyc TiO_2 on PEN substrate using plasma ALD (Cambridge Nanotech Plasma ALD system) at 100°C. The total thickness of ALD films is ~20 nm. Figure 68 demonstrates the final structure used for encapsulation of perovskite cells. The efficiency was determined using 2-probe method with intensity of 1 Sun (~100 mW/cm^2). Devices were stored in open air at room temperature and in dark condition. Initial measurements were taken for the as received cells. Measurements were taken again after SiNx deposition to determine if there was any degradation or reduction in efficiency of the cells due to temperature or plasma from PECVD SiNx deposition chamber. Samples were stored in a glove box in the dark at room temperature for a few days to determine if there was any effect of the adhesive layer (Tesa tape) on the efficiency of the devices. Finally, cells were taken out of the glove box and their efficiency is monitored in open air conditions at different time intervals.

8.2.5 Results of Perovskite cell encapsulation

Figure 69 shows JV curves and efficiency measurements taken for three encapsulated devices. These devices typically had efficiency of 14-16%. Efficiency plots show the variation in efficiency of devices with time. It can be noted that the initial measurements were taken for the as received cells, whereas initial measurements were taken after complete encapsulation of devices. Also, the devices were kept in the glove box in dark conditions for 72 hours before taking any measurements after encapsulation. The initially high value of efficiency demonstrates that SiNx can be integrated with the PSC and prevent the adhesive from reacting with the solar cell.

Measurements show that there is some fluctuation in the measurement data, i.e. efficiency first goes down and then rises again. This fluctuation in efficiency could be the result of poor contacts. The electrodes are made up of Al and were deposited on polymer. This resulted in very poor adhesion of the electrodes due to which the electrodes used to get peeled of quite often while making electrical contacts for taking measurements. Hence, before taking the last reading at 4320 hours, electrodes were re-deposited on the devices to make proper contact. High efficiency of devices after exposure to such a long time demonstrates quality of barrier encapsulation and the effectiveness of PECVD SiNx as the buffer layer while protecting it from the encapsulation materials.

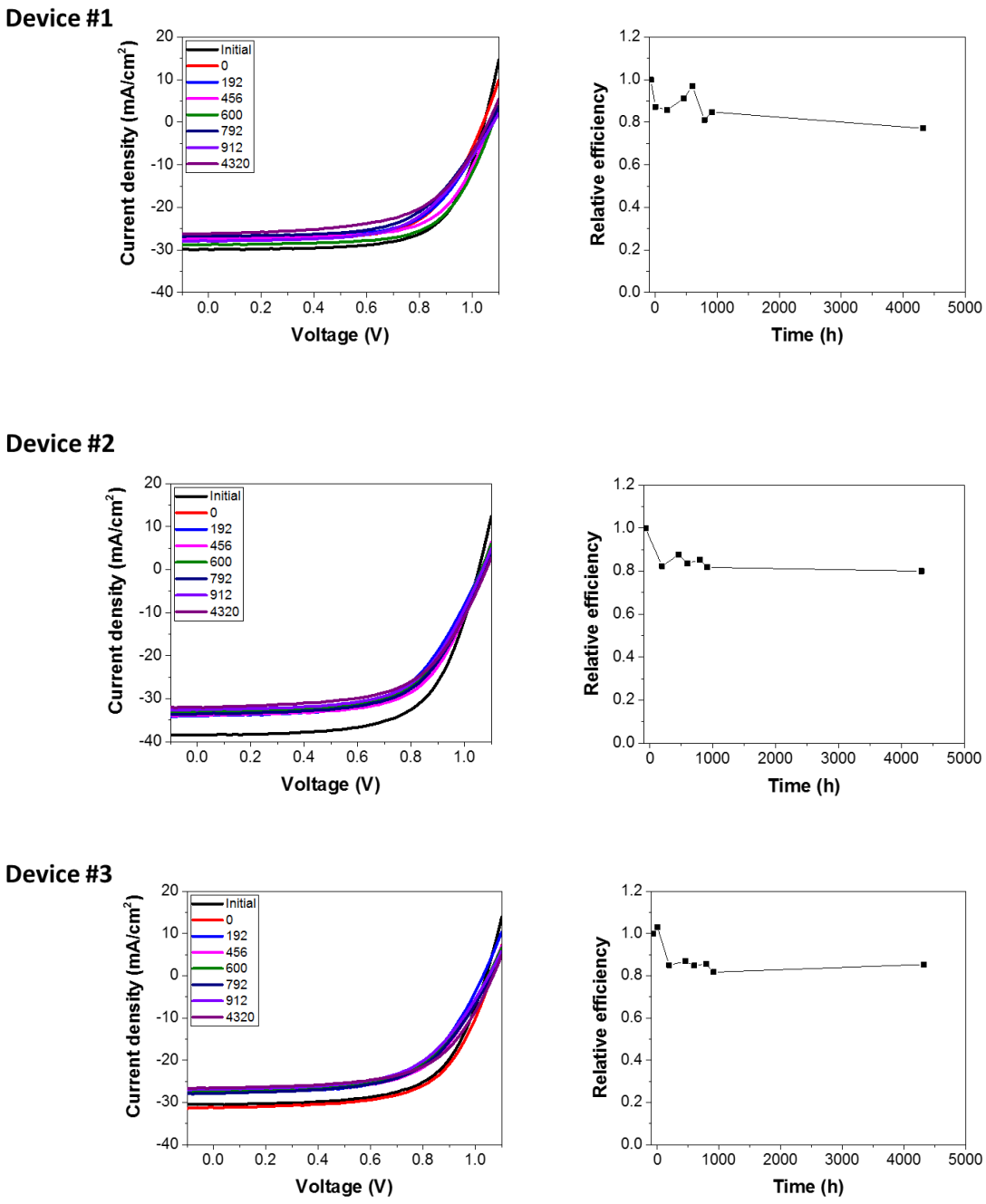

Figure 69 - JV curves and efficiency measurements of the devices.

8.3 Summary

This chapter shows that the PSCs, which are extremely sensitive to almost any kind of external condition, can effectively be made stable for several months with minimal degradation in their performance by using a barrier encapsulation. Due to their instability, use of either direct or indirect encapsulation is not possible due to chemical interaction between the PSCs and barrier material/fabrication process. However, by using a layer of PECVD SiNx, which is deposited directly on the PSCs, the use of indirect encapsulation method becomes feasible. The layer of PECVD SiNx acts as a buffer layer between the PSCs and the adhesive material, used during the indirect encapsulation, while avoiding any kind of chemical interaction between the two. This opens up a new possibility for the encapsulation of PSCs using PECVD SiNx as the buffer layer and indirect encapsulation method.

CHAPTER 9. CONCLUSIONS

9.1 Summary and Conclusions

Electronic devices are often sensitive to the surrounding media based on their application. For any viable and commercial application, the electronic devices need to be stable and perform reliably for the designated period of usage. Therefore, the electronic devices need an additional protective layer which can prevent any kind of direct interaction between the device material and the surrounding media. With the miniaturization of devices and demand for the development of flexible electronic technology, ultrathin barrier encapsulations are required. These barrier films can be prepared using the ALD and PECVD deposition techniques. Several studies have been conducted for the fabrication of barrier films using these two deposition techniques with success in obtaining the desired value of permeation rates for the defect free regions of the barrier. However, due to several external and uncontrolled reasons, defects are created in the barriers which allow permeation of unwanted species at high rates locally through the defects. These defects could be the result of particle contamination, stresses in the films, and chemical instability of the barrier material in the surrounding media. Therefore, even after achieving the desired permeation resistance, the thin film barrier technology still faces a major challenge of particle contamination and chemical stability. Lastly, even after the fabrication of high quality of barrier film, their integration with the devices faces additional challenge due to the sensitivity of the device itself, like PSCs. PSCs are sensitive to almost any kind of external interaction whether it is physical, chemical or thermal. Thus, it becomes extremely difficult to apply any kind of barrier encapsulation on this kind of devices.

The research in this dissertation is, therefore, focused mainly on improving the performance of barrier films with defects, their chemical stability and finally, integration of barrier films with the PSCs. The following are the achievements of this dissertation.

Chapter 4 deals with the issue of particle contamination and cracks formed due to particle inclusions in the ALD barrier film. Due to high density and conformal nature, ALD barrier films ideally should be sufficient to provide required level of permeation resistance against atmospheric species. However, particle contamination which get incorporated into the barrier structures during different steps of fabrication result in the formation of cracks in the proximity of the particles. Due to high permeation rates through the defects, the overall performance of the barrier encapsulation is severely affected. Due to practical and economical constraints, it is not possible to avoid such contamination. During the whole process of barrier fabrication, several kinds of particles get into the barrier matrix. With the variation in the nature of particle, their effect on the defect formation also varies significantly. It has been shown that soft and compliant particles with lower values of elastic modulus are more prone to crack formation than those with higher values of elastic modulus. This study, therefore, suggests that additional care must be taken in case of sources of particle inclusions with polymeric origin. Since the possibility of inclusion of particle contamination into the barrier structure and therefore, crack formation is not completely avoidable, this study further demonstrates the use of PECVD SiNx to heal the cracks in the ALD layer. It has been shown for the first time that the sequence of layers in the barrier structure can have huge impact on the overall performance of the barrier films, and therefore, In a barrier architecture, ALD films should always be followed by the deposition of PECVD SiNx such that the defects in the ALD layer get sealed.

Chapter 5 deals with the issue of side permeation in case of indirect encapsulations. Edge seals are often employed along the edges of the device encapsulation to prevent any kind of moisture ingress from the sides. During this process, two surfaces are brought in contact with each other leading to the formation of interfaces. Due to the imperfect nature of bonding between two surfaces, there is pores at the interfaces. A continuous chain of these pores results in the formation of capillaries at the interface which acts as an additional route for the permeation of water as opposed to just the bulk of the sealant material. Under certain conditions of high humidity and low temperature of the devices, water can condense near the ends of these capillaries and preferably permeate through them. The overall rate of permeation through the sides therefore is governed by the dominant phenomenon which is either permeation through the bulk of the sealant material or the capillaries formed at the interface. Since the capillaries are formed by the interfaces of two surfaces, the permeation rate through them is, therefore, governed by the surface energies of the materials at the interface. The study in this chapter demonstrates that the rates of side permeation can be reduced significantly by using materials with high contact angles at the interfaces. A parametric study conducted using a mathematical model suggests that with contact angles of the materials being 90° or above, the permeation through the capillaries can be completely blocked which will leave the bulk of the sealant material as the only pathway for water permeation.

In chapter 6, the stability of ALD metal oxides in biological solutions has been investigated. This study aims at increasing the domain for potential of ALD barrier films to biological environments like human body with either external or internal use. The four ALD metal oxides used for this study include Al_2O_3, HfO_2, TiO_2 and ZrO_2, which were

deposited at 100°C. First the cytocompatibility of all the ALD materials was tested to determine if the ALD materials are cytocompatible with the living cells. It was found that all the four ALD metal oxides are cytocompatible and within the time frame of the testing do not pose any threat to the living cells. On testing the materials in variety of biological solutions like PBS, saliva and sweat, it was found that ALD Al_2O_3 is the least stable material which tends to dissolve completely into the aqueous solutions. ALD HfO_2 shows some improvement over Al_2O_3 but also shows degradation in long duration of exposure. In saliva, ALD ZrO_2 is the most stable material followed by ALD TiO_2. However, in sweat solution, none of the materials was found to be completely stable with all the materials showing at least some level of degradation while ALD TiO_2 performing the best. Therefore, in conclusion, it is recommended to use the nanolaminate structure of ALD TiO_2/ZrO_2 to exploit the properties of both the materials thereby making the combined material to be most stable for biological applications. This study, therefore, enhances the scope of use of ALD deposited metal oxides to applications like sensors, actuators, microfluidic, bioimplants and wearable devices. Since the cytocompatibility test was conducted for a short time period, longer term in vitro and in vivo studies are required in future to confirm the use of ALD materials for aforementioned applications.

In chapter 7, the chemical stability of ALD metal oxides in different chemical environments has been tested. The ALD metal oxides tested includes Al_2O_3, HfO_2, TiO_2 and ZrO_2, which were deposited at 100°C. The stability tests were conducted in 3.5% NaCl, sea water, HCl (pH4) and H_2SO_4 (pH4) solutions. These solutions provided a variety of ionic species for testing the chemical stability of ALD materials. Using EIS, ALD Al_2O_3 was found to the most unstable material as it tends to dissolve completely in the tested

solutions. PL study also confirmed the findings from the EIS test for ALD Al_2O_3 that it dissolves completely in to the solutions. EIS for ALD HFO_2 has shown increased chemical stability with some localized degradations resulting due to the presence of defects in 3.5% NaCl solution and sea water. PL study revealed that ALD HfO_2 was able to protect the coated ZnO layer. This shows that the defects created in the ALD HfO_2 layer were confined within its thickness and it did not grow across the layer thickness. For HCl (pH4) and H_2SO_4 (pH4) solutions, using EIS, it was found that ALD HfO_2 was completely stable in these solutions. However, when PL study was conducted in these solutions, it was found that the underneath layer of ZnO got dissolved into the solution after few days of exposure to the acidic solutions. This indicated that, although ALD HfO_2 is chemically stable, it is not a reliable barrier material. ALD TiO_2 and ZrO_2, however, showed excellent chemical stability in all the four solutions during EIS testing, whereas PL tests revealed that both these materials were able to protect the coated ZnO layer. This demonstrates that ALD TiO_2 and ZrO_2 are suitable to be used as barrier in various ionic solutions.

In chapter 8, the integration of barrier films with the PSCs has been discussed. It is well known that PSCs are extremely vulnerable to any external influence. But, for any kind of commercial application, PSCs need to have a long lifetime under the operating conditions of open atmospheric surroundings. For the protection of PSCs from atmospheric species, barrier encapsulations are required to be applied. However, the high sensitivity of PSCs with the fabrication processes limits the use of any of the encapsulation methods, whether it is direct or indirect encapsulation. In case of indirect encapsulation, the direct contact between the adhesive material and PSCs leads to chemical interaction between them while degrading the devices extremely rapidly. To prevent this kind of direct

interaction, the concept of using PECVD SiNx as a buffer layer was introduced. It was shown that PECVD SiNx can be deposited on top of PSCs before using indirect encapsulation method for applying the barrier coating. PECVD SiNx deposited on the surface of PSCs prevents any kind of direct interaction of PSCs with the adhesive material, thereby, making the use of indirect encapsulation feasible. The devices encapsulated with ALD barrier films using PECVD SiNx as the buffer layer lasted for several months with not much reduction in their initial efficiency. This shows the effectiveness of PECVD SiNx as the buffer layer and it opens up the possibility for application of barriers using indirect encapsulation method.

9.2 Future work

9.2.1 Chemical stability of ALD materials

In this work, the four ALD materials, including Al_2O_3, HfO_2, TiO_2 and ZrO_2, were tested for chemical stability in different ionic and biological solutions. It was found that ALD TiO_2 and ALD ZrO_2 are the most stable amongst the tested materials. However, ever these two materials were found to be unstable in solutions like saliva and sweat. Therefore, as a further step to determine the most stable ALD material, a nanolaminate of ALD TiO_2 and ALD ZrO_2 can be tested in different solutions. Also, the domain of harsh environments can be increased to other solutions like mercury, boiling water, acidic solutions with pH lower than 4 and alkaline solutions with pH higher than 10.

In this study, the equivalent circuits were used to describe the nature of degradation of ALD materials in different solutions. A detailed study can be conducted to correlate the different components of equivalent circuits to the physical phenomenon taking place in the electrochemical system when the ALD films are exposed to the solutions. This may help in having larger control over the rate of degradation of ALD materials.

9.2.2 Biocompatibility of ALD materials

In this work, Using MTT test, it has been demonstrated that all the four ALD materials, including Al_2O_3, HfO_2, TiO_2 and ZrO_2, are cytocompatible in nature. The MTT test was conducted by placing the ALD coated samples in cell culture for 18 hours. This time of exposure of ALD films to the cell culture is limited because if the cells are allowed to grow further with time, it would result in killing of the cells just because of overcrowding leading to false results. Also, it is possible that the ALD films are soluble in the cell culture in a longer duration. In that case, the cytocompatibility of the ALD material that has dissolved into the media and the ALD material that still remains on the surface of the substrates need to be determined. Under the current experimental arrangement, it was not possible to carry out such a test. A new way of testing methodology needs to be adopted or developed that can address this issue. Also, before using the ALD material coatings in implants, a detailed study of biocompatibility with the living subjects needs to be conducted.

The stability of ALD materials in different biological solutions was determined using EIS. The magnitude of potential applied during EIS was 10 mV. In case of implants

like pace makers and some neurological sensors, the applied voltage may be of significantly larger than 10 mV. This would create very high electric field across the barrier materials which may result in accumulation of charges near its surface thereby initiating redox reactions. It would, therefore, be interesting to monitor the performance of different ALD barrier materials in case of applied electric fields.

9.2.3 Encapsulation of perovskite solar cells

In this work, it has been shown that PECVD SiNx can be used as a buffer layer during the indirect encapsulation of PSCs consisting of methylammonium ($CH_3NH_3^+$ (MA)) lead triiodide as the active layer. Experiments were further conducted for two more kinds of PSCs consisting of formamidinium ($CH(NH_2)_2^+$ (FA)) lead triiodide, and a combination of FA^+, MA^+ and Cs^+, as well as both I^- and Br^- anions (FAMACs), as the active layers. The devices were obtained from Dr. Joseph Berry's group (NREL) and their manufacturing procedures have been described in the references.[167, 168]

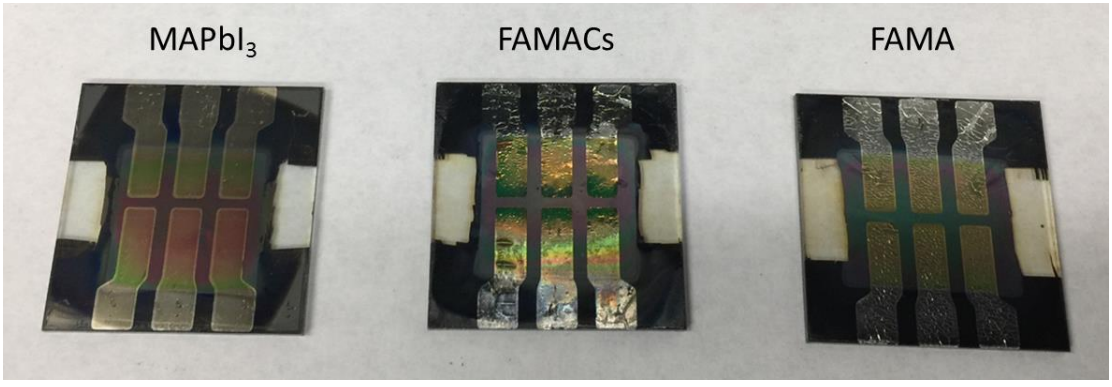

Figure 70 – Images of PSCs after the deposition of 500 nm of PECVD SiNx at 110°C.

The images of all the three devices after depositing 500 nm SiNx at 110°C are shown in Figure 70. There is no difference in the surface morphology of the PSC containing $MAPbI_3$. However, in case of PSCs consisting of FAMACs and FAMA cations, the devices appeared to have wrinkles and fractures on their surfaces. On taking the PCE measurements of the PSCs, it was observed that $MAPbI_3$ and FAMA devices were active whereas FAMACs devices were found to be dead. This shows contrasting nature in the response of PSCs after the deposition of PECVD SiNx layer on them. Even after the formation of wrinkles and cracks, FAMA devices were still active. However, the same was not true in case of FAMACs devices. It would, therefore, be interesting to determine the interaction between different perovskite active layers and PECVD SiNx. This will ascertain the suitability of the PECVD process for a particular kind of devices or the modifications needed in the devices to achieve compatibility.

REFERENCES

1. Logothetidis, S., *Flexible organic electronic devices: Materials, process and applications.* Materials Science and Engineering: B, 2008. **152**(1–3): p. 96-104.

2. Berggren, M., D. Nilsson, and N.D. Robinson, *Organic materials for printed electronics.* Nat Mater, 2007. **6**(1): p. 3-5.

3. Nakada, H., *The Status of development of Organic Light Emitting Diodes / Organic Thin-film Transistors.* Journal of Photopolymer Science and Technology, 2007. **20**(1): p. 35-38.

4. Kelley, T.W., et al., *Recent Progress in Organic Electronics: Materials, Devices, and Processes.* Chemistry of Materials, 2004. **16**(23): p. 4413-4422.

5. Cao, W. and J. Xue, *Recent progress in organic photovoltaics: device architecture and optical design.* Energy & Environmental Science, 2014. **7**(7): p. 2123-2144.

6. Rychly, J. and B. Nebe, *Interface Biology of Implants.* Cell Adhesion & Migration, 2009. **3**(4): p. 390-394.

7. Kim, L.H., et al., *Al2O3/TiO2 nanolaminate thin film encapsulation for organic thin film transistors via plasma-enhanced atomic layer deposition.* ACS Appl Mater Interfaces, 2014. **6**(9): p. 6731-8.

8. Kim, S.H., et al., *Damage-free hybrid encapsulation of organic field-effect transistors to reduce environmental instability.* Journal of Materials Chemistry, 2012. **22**(16): p. 7731-7738.

9. Jørgensen, M., K. Norrman, and F.C. Krebs, *Stability/degradation of polymer solar cells.* Solar Energy Materials and Solar Cells, 2008. **92**(7): p. 686-714.

10. Lewis, J.S. and M.S. Weaver, *Thin-film permeation-barrier technology for flexible organic light-emitting devices.* Selected Topics in Quantum Electronics, IEEE Journal of, 2004. **10**(1): p. 45-57.

11. Fang, H., et al., *Ultrathin, transferred layers of thermally grown silicon dioxide as biofluid barriers for biointegrated flexible electronic systems.* Proceedings of the National Academy of Sciences, 2016. **113**(42): p. 11682-11687.

12. Burrows, P.E., et al. *Gas permeation and lifetime tests on polymer-based barrier coatings*. 2001.

13. Nisato, G., et al., *P-88: Thin Film Encapsulation for OLEDs: Evaluation of Multi-layer Barriers using the Ca Test.* SID Symposium Digest of Technical Papers, 2003. **34**(1): p. 550-553.

14. Park, M.-H., et al. *Flexible organic light-emitting diodes for solid-state lighting*. 2015. SPIE.

15. Carcia, P.F., et al., *Ca test of Al[sub 2]O[sub 3] gas diffusion barriers grown by atomic layer deposition on polymers.* Applied Physics Letters, 2006. **89**(3): p. 031915.

16. Perrotta, A., et al., *On the role of nanoporosity in controlling the performance of moisture permeation barrier layers.* Microporous and Mesoporous Materials, 2014. **188**: p. 163-171.

17. Andringa, A.M., et al., *Low-Temperature Plasma-Assisted Atomic Layer Deposition of Silicon Nitride Moisture Permeation Barrier Layers.* ACS Appl Mater Interfaces, 2015. **7**(40): p. 22525-32.

18. Carcia, P.F., et al., *Permeability and corrosion in ZrO2/Al2O3 nanolaminate and Al2O3 thin films grown by atomic layer deposition on polymers.* Journal of Vacuum Science & Technology A: Vacuum, Surfaces, and Films, 2012. **30**(4): p. 041515.

19. Meyer, J., et al., *Al2O3/ZrO2Nanolaminates as Ultrahigh Gas-Diffusion Barriers-A Strategy for Reliable Encapsulation of Organic Electronics.* Advanced Materials, 2009. **21**(18): p. 1845-1849.

20. Bulusu, A., et al., *Engineering the mechanical properties of ultrabarrier films grown by atomic layer deposition for the encapsulation of printed electronics.* Journal of Applied Physics, 2015. **118**(8): p. 085501.

21. Groner, M.D., et al., *Gas diffusion barriers on polymers using Al[sub 2]O[sub 3] atomic layer deposition.* Applied Physics Letters, 2006. **88**(5): p. 051907.

22. Seo, S.-W., et al., *Water permeation through organic–inorganic multilayer thin films.* Thin Solid Films, 2012. **520**(21): p. 6690-6694.

23. Kojima, A., et al., *Organometal Halide Perovskites as Visible-Light Sensitizers for Photovoltaic Cells.* Journal of the American Chemical Society, 2009. **131**(17): p. 6050-6051.

24. Green, M.A., A. Ho-Baillie, and H.J. Snaith, *The emergence of perovskite solar cells.* Nature Photonics, 2014. **8**(7): p. 506-514.

25. Jeon, N.J., et al., *Compositional engineering of perovskite materials for high-performance solar cells.* Nature, 2015. **517**(7535): p. 476-80.

26. Liu, M., M.B. Johnston, and H.J. Snaith, *Efficient planar heterojunction perovskite solar cells by vapour deposition.* Nature, 2013. **501**(7467): p. 395-8.

27. Chen, Q., et al., *Planar heterojunction perovskite solar cells via vapor-assisted solution process.* J Am Chem Soc, 2014. **136**(2): p. 622-5.

28. Yella, A., et al., *Nanocrystalline rutile electron extraction layer enables low-temperature solution processed perovskite photovoltaics with 13.7% efficiency.* Nano Lett, 2014. **14**(5): p. 2591-6.

29. Zardetto, V., et al., *Atomic layer deposition for perovskite solar cells: research status, opportunities and challenges.* Sustainable Energy Fuels, 2017. **1**(1): p. 30-55.

30. Han, Y., et al., *Degradation observations of encapsulated planar CH3NH3PbI3perovskite solar cells at high temperatures and humidity.* J. Mater. Chem. A, 2015. **3**(15): p. 8139-8147.

31. Weerasinghe, H.C., et al., *Encapsulation for improving the lifetime of flexible perovskite solar cells.* Nano Energy, 2015. **18**: p. 118-125.

32. Ramos, F.J., et al. *Fabrication and encapsulation of perovskites sensitized solid state solar cells*. in *2014 IEEE 40th Photovoltaic Specialist Conference (PVSC)*. 2014.

33. George, S.M., *Atomic layer deposition: an overview*. Chem Rev, 2010. **110**(1): p. 111-31.

34. Puurunen, R.L., *Surface chemistry of atomic layer deposition: A case study for the trimethylaluminum/water process.* Journal of Applied Physics, 2005. **97**(12): p. 121301.

35. Profijt, H.B., et al., *Plasma-Assisted Atomic Layer Deposition: Basics, Opportunities, and Challenges.* Journal of Vacuum Science & Technology A: Vacuum, Surfaces, and Films, 2011. **29**(5).

36. Ritala, M., et al., *Perfectly Conformal TiN and Al2O3 Films Deposited by Atomic Layer Deposition.* Chemical Vapor Deposition, 1999. **5**(1): p. 7-9.

37. van Delft, J.A., D. Garcia-Alonso, and W.M.M. Kessels, *Atomic layer deposition for photovoltaics: applications and prospects for solar cell manufacturing.* Semiconductor Science and Technology, 2012. **27**(7): p. 074002.

38. Ahmad, J., et al., *Materials and methods for encapsulation of OPV: A review.* Renewable and Sustainable Energy Reviews, 2013. **27**: p. 104-117.

39. Abdulagatov, A.I., et al., *Al_2O_3 and TiO_2 atomic layer deposition on copper for water corrosion resistance.* ACS applied materials & interfaces, 2011. **3**(12): p. 4593-601.

40. Johnson, R.W., A. Hultqvist, and S.F. Bent, *A brief review of atomic layer deposition: from fundamentals to applications.* Materials Today, 2014. **17**(5): p. 236-246.

41. Suntola, T., *Atomic Layer Epitaxy. In Handbook of Crystal Growth, Vol. 3, Part B: Growth Mechanisms and Dynamics;* . Hurle, D. T. J., Ed.; Elsevier: Amsterdam, 1994; Chapter 14 ed.

42. Wang, C.Y., et al., *Organic Field-Effect Transistors with a Bilayer Gate Dielectric Comprising an Oxide Nanolaminate Grown by Atomic Layer Deposition.* ACS Appl Mater Interfaces, 2016. **8**(44): p. 29872-29876.

43. Ghosh, A.P., et al., *Thin-film encapsulation of organic light-emitting devices.* Applied Physics Letters, 2005. **86**(22): p. 223503.

44. Mackus, A.J.M., et al., *Room-Temperature Atomic Layer Deposition of Platinum.* Chemistry of Materials, 2013. **25**(9): p. 1769-1774.

45. Klaus, J.W. and S.M. George, *Atomic layer deposition of SiO2 at room temperature using NH3-catalyzed sequential surface reactions.* Surface Science, 2000. **447**(1–3): p. 81-90.

46. Kanomata, K., et al., *Room-temperature atomic layer deposition of ZrO 2 using tetrakis(ethylmethylamino)zirconium and plasma-excited humidified argon.* Applied Surface Science, 2016. **387**: p. 497-502.

47. Kessels, W.M.M. and M. Putkonen, *Advanced process technologies: Plasma, direct-write, atmospheric pressure, and roll-to-roll ALD.* MRS Bulletin, 2011. **36**(11): p. 907-913.

48. Poodt, P., et al., *Spatial atomic layer deposition: A route towards further industrialization of atomic layer deposition.* Journal of Vacuum Science & Technology A, 2012. **30**(1).

49. Poodt, P., et al., *High-speed spatial atomic-layer deposition of aluminum oxide layers for solar cell passivation.* Adv Mater, 2010. **22**(32): p. 3564-7.

50. Poodt, P., et al., *Low temperature and roll-to-roll spatial atomic layer deposition for flexible electronics.* Journal of Vacuum Science & Technology A, 2012. **30**(1).

51. Hoye, R.L.Z., et al., *Research Update: Atmospheric pressure spatial atomic layer deposition of ZnO thin films: Reactors, doping, and devices.* APL Materials, 2015. **3**(4).

52. George, S.M., *Atomic Layer Deposition: An Overview.* Chemical Reviews, 2009. **110**(1): p. 111-131.

53. Roberts, A.P., et al., *Gas permeation in silicon-oxide/polymer (SiOx/PET) barrier films: role of the oxide lattice, nano-defects and macro-defects.* Journal of Membrane Science, 2002. **208**(1–2): p. 75-88.

54. Dennler, G., et al., *Flexible, conjugated polymer-fullerene-based bulk-heterojunction solar cells: Basics, encapsulation, and integration.* Journal of Materials Research, 2011. **20**(12): p. 3224-3233.

55. Carcia, P.F., et al., *Gas diffusion ultrabarriers on polymer substrates using Al[sub 2]O[sub 3] atomic layer deposition and SiN plasma-enhanced chemical vapor deposition.* Journal of Applied Physics, 2009. **106**(2): p. 023533.

56. Carcia, P.F., R.S. McLean, and M.H. Reilly, *Permeation measurements and modeling of highly defective Al2O3 thin films grown by atomic layer deposition on polymers.* Applied Physics Letters, 2010. **97**(22): p. 221901.

57. Kim, K., et al., *Environmentally Assisted Cracking in Silicon Nitride Barrier Films on Poly(ethylene terephthalate) Substrates.* ACS Appl Mater Interfaces, 2016.

58. Greener, J., et al., *Moisture permeability through multilayered barrier films as applied to flexible OLED display.* Journal of Applied Polymer Science, 2007. **106**(5): p. 3534-3542.

59. Yu, D., et al., *Recent progress on thin-film encapsulation technologies for organic electronic devices.* Optics Communications, 2016. **362**: p. 43-49.

60. Jarvis, K.L. and P.J. Evans, *Growth of thin barrier films on flexible polymer substrates by atomic layer deposition.* Thin Solid Films, 2017. **624**: p. 111-135.

61. Keuning, W., et al., *Cathode encapsulation of organic light emitting diodes by atomic layer deposited Al2O3 films and Al2O3/a-SiNx:H stacks.* Journal of Vacuum Science & Technology A: Vacuum, Surfaces, and Films, 2012. **30**(1): p. 01A131.

62. da Silva Sobrinho, A.S., et al., *Defect-permeation correlation for ultrathin transparent barrier coatings on polymers.* Journal of Vacuum Science & Technology A: Vacuum, Surfaces, and Films, 2000. **18**(1): p. 149.

63. Purkl, F., et al., *Measurement of Young's modulus and residual stress of atomic layer deposited Al2O3 and Pt thin films.* Journal of Micromechanics and Microengineering, 2017. **27**(8).

64. Zhu, Z., E. Salmi, and S. Virtanen. *Residual stress study of thin films deposited by atomic layer deposition*. in *2017 IEEE 12th International Conference on ASIC (ASICON)*. 2017.

65. Ylivaara, O.M.E., et al., *Aluminum oxide from trimethylaluminum and water by atomic layer deposition: The temperature dependence of residual stress, elastic modulus, hardness and adhesion.* Thin Solid Films, 2014. **552**: p. 124-135.

66. Chen, T.N., et al., *High-Performance Transparent Barrier Films of SiO[sub x]/SiN[sub x] Stacks on Flexible Polymer Substrates.* Journal of The Electrochemical Society, 2006. **153**(10): p. F244.

67. Bulusu, A., et al., *Improving the stability of atomic layer deposited alumina films in aqueous environments with metal oxide capping layers.* Journal of Physics D: Applied Physics, 2013. **46**(8): p. 084014.

68. Dameron, A.A., et al., *Gas Diffusion Barriers on Polymers Using Multilayers Fabricated by Al2O3 and Rapid SiO2 Atomic Layer Deposition.* The Journal of Physical Chemistry C, 2008. **112**(12): p. 4573-4580.

69. Potts, S.E., et al., *Ultra-Thin Aluminium Oxide Films Deposited by Plasma-Enhanced Atomic Layer Deposition for Corrosion Protection.* Journal of The Electrochemical Society, 2011. **158**(5): p. C132-C138.

70. Marin, E., et al., *Corrosion protection of AISI 316 stainless steel by ALD alumina/titania nanometric coatings.* Journal of Coatings Technology and Research, 2011. **8**(5): p. 655-659.

71. Shan, C.X., X. Hou, and K.-L. Choy, *Corrosion resistance of TiO2 films grown on stainless steel by atomic layer deposition.* Surface and Coatings Technology, 2008. **202**(11): p. 2399-2402.

72. Shan, C.X., et al., *Improvement in corrosion resistance of CrN coated stainless steel by conformal TiO2 deposition.* Surface and Coatings Technology, 2008. **202**(10): p. 2147-2151.

73. Greatbatch, W. and C.F. Holmes, *History of implantable devices.* IEEE Engineering in Medicine and Biology Magazine, 1991. **10**(3): p. 38-41.

74. Hassarati, R.T., et al., *Improving cochlear implant properties through conductive hydrogel coatings.* IEEE Trans Neural Syst Rehabil Eng, 2014. **22**(2): p. 411-8.

75. Alves, P., et al., *Surface modification of polyurethane films by plasma and ultraviolet light to improve haemocompatibility for artificial heart valves.* Colloids Surf B Biointerfaces, 2014. **113**: p. 25-32.

76. Ma, X., et al., *Drug-eluting stents.* International Journal of Clinical and Experimental Medicine, 2010. **3**(3): p. 192-201.

77. Hwang, G.-T., et al., *Self-Powered Cardiac Pacemaker Enabled by Flexible Single Crystalline PMN-PT Piezoelectric Energy Harvester.* Advanced Materials, 2014. **26**(28): p. 4880-4887.

78. Zhong, J., et al., *Fiber-Based Generator for Wearable Electronics and Mobile Medication.* ACS Nano, 2014. **8**(6): p. 6273-6280.

79. Paital, S.R. and N.B. Dahotre, *Calcium phosphate coatings for bio-implant applications: Materials, performance factors, and methodologies.* Materials Science and Engineering: R: Reports, 2009. **66**(1-3): p. 1-70.

80. Bazaka, K. and M. Jacob, *Implantable Devices: Issues and Challenges.* Electronics, 2012. **2**(1): p. 1-34.

81. Lago, N., et al., *Long term assessment of axonal regeneration through polyimide regenerative electrodes to interface the peripheral nerve.* Biomaterials, 2005. **26**(14): p. 2021-31.

82. Roy, R.K. and K.R. Lee, *Biomedical applications of diamond-like carbon coatings: A review.* Journal of Biomedical Materials Research Part B-Applied Biomaterials, 2007. **83B**(1): p. 72-84.

83. Cogan, S.F., et al., *Plasma-enhanced chemical vapor deposited silicon carbide as an implantable dielectric coating.* Journal of Biomedical Materials Research - Part A, 2003. **67**(3): p. 856-867.

84. Hsu, J.M., et al., *Characterization of a-SiCx : H thin films as an encapsulation material for integrated silicon based neural interface devices.* Thin Solid Films, 2007. **516**(1): p. 34-41.

85. Wu, J.L., et al., *Evaluation and characterization of reliable non-hermetic conformal coatings for microelectromechanical system (MEMS) device encapsulation.* IEEE Transactions on Advanced Packaging, 2000. **23**(4): p. 721-728.

86. Iguchi, N., et al., *Contact Sensitivity to Polychloroparaxylene-Coated Cardiac Pacemaker.* Pacing and Clinical Electrophysiology, 1997. **20**(2): p. 372-373.

87. Loeb, G.E., et al., *Parylene as a Chronically Stable, Reproducible Microelectrode Insulator.* IEEE Transactions on Biomedical Engineering, 1977. **BME-24**(2): p. 121-128.

88. Schmidt, E.M., J.S. Mcintosh, and M.J. Bak, *Long-term implants of Parylene-C coated microelectrodes.* Medical and Biological Engineering and Computing, 1988. **26**(1): p. 96-101.

89. deCharms, R.C., D.T. Blake, and M.M. Merzenich, *A multielectrode implant device for the cerebral cortex.* Journal of Neuroscience Methods, 1999. **93**(1): p. 27-35.

90. Hsu, J.M., et al., *Encapsulation of an integrated neural interface device with Parylene C.* IEEE Trans Biomed Eng, 2009. **56**(1): p. 23-9.

91. Chun, W., et al., *Evaluation of sub-micrometer parylene C films as an insulation layer using electrochemical impedance spectroscopy.* Progress in Organic Coatings, 2014. **77**(2): p. 537-547.

92. Donaldson, P., *Encapsulating microelectronic implants in one-part silicone rubbers.* Medical and Biological Engineering and Computing, 1989. **27**(1): p. 93-94.

93. Rodger, D.C. and T. Yu-Chong, *Microelectronic packaging for retinal prostheses.* Engineering in Medicine and Biology Magazine, IEEE, 2005. **24**(5): p. 52-57.

94. Wasikiewicz, J.M., et al., *Polymeric barrier membranes for device packaging, diffusive control and biocompatibility.* Applied Surface Science, 2008. **255**(2): p. 340-343.

95. Im, H., et al., *Atomic layer deposition (ALD): A versatile technique for plasmonics and nanobiotechnology.* J Mater Res, 2012. **27**(4): p. 663-671.

96. Xie, X., et al., *Plasma-assisted atomic layer deposition of Al<inf>2</inf>O<inf>3</inf> and parylene C bi-layer encapsulation for chronic implantable electronics.* Applied Physics Letters, 2012. **101**(9): p. 093702-093702-5.

97. Carlisle, J., et al., *Hermetic bio-inert coatings for bio-implants fabricated using atomic layer deposition*. 2006, Google Patents.

98. Finch, D.S., et al., *Biocompatibility of atomic layer-deposited alumina thin films.* J Biomed Mater Res A, 2008. **87**(1): p. 100-6.

99. Hyde, G.K., et al., *Atomic layer deposition and biocompatibility of titanium nitride nano-coatings on cellulose fiber substrates.* Biomed Mater, 2009. **4**(2): p. 025001.

100. Hyde, G.K., et al., *Atomic layer deposition and abrupt wetting transitions on nonwoven polypropylene and woven cotton fabrics.* Langmuir, 2010. **26**(4): p. 2550-8.

101. Seo, J., J.H. Noh, and S.I. Seok, *Rational Strategies for Efficient Perovskite Solar Cells.* Acc Chem Res, 2016. **49**(3): p. 562-72.

102. Gratzel, M., *The light and shade of perovskite solar cells.* Nat Mater, 2014. **13**(9): p. 838-42.

103. Kim, H.S., et al., *Lead iodide perovskite sensitized all-solid-state submicron thin film mesoscopic solar cell with efficiency exceeding 9%.* Sci Rep, 2012. **2**: p. 591.

104. Lee, M.M., et al., *Efficient Hybrid Solar Cells Based on Meso-Superstructured Organometal Halide Perovskites.* Science, 2012. **338**(6107): p. 643-647.

105. Li, D.-l., et al., *Stress control of silicon nitride films deposited by plasma enhanced chemical vapor deposition.* Optoelectronics Letters, 2016. **12**(4): p. 285-289.

106. Yang, J., et al., *Investigation of CH3NH3PbI3 Degradation Rates and Mechanisms in Controlled Humidity Environments Using in Situ Techniques.* ACS Nano, 2015. **9**(2): p. 1955-1963.

107. Zhao, J., et al., *Investigation of the Hydrolysis of Perovskite Organometallic Halide CH3NH3PbI3 in Humidity Environment.* Sci Rep, 2016. **6**: p. 21976.

108. Matteocci, F., et al., *Encapsulation for long-term stability enhancement of perovskite solar cells.* Nano Energy, 2016. **30**: p. 162-172.

109. Divitini, G., et al., *In situ observation of heat-induced degradation of perovskite solar cells.* Nature Energy, 2016. **1**(2).

110. Conings, B., et al., *Intrinsic Thermal Instability of Methylammonium Lead Trihalide Perovskite.* Advanced Energy Materials, 2015. **5**(15).

111. Leijtens, T., et al., *Overcoming ultraviolet light instability of sensitized TiO(2) with meso-superstructured organometal tri-halide perovskite solar cells.* Nat Commun, 2013. **4**: p. 2885.

112. Leijtens, T., et al., *Stability of Metal Halide Perovskite Solar Cells.* Advanced Energy Materials, 2015. **5**(20).

113. Law, C., et al., *Performance and stability of lead perovskite/TiO2, polymer/PCBM, and dye sensitized solar cells at light intensities up to 70 suns.* Adv Mater, 2014. **26**(36): p. 6268-73.

114. Wei, D., et al., *Photo-induced degradation of lead halide perovskite solar cells caused by the hole transport layer/metal electrode interface.* Journal of Materials Chemistry A, 2016. **4**(5): p. 1991-1998.

115. Sanchez, R.S. and E. Mas-Marza, *Light-induced effects on Spiro-OMeTAD films and hybrid lead halide perovskite solar cells.* Solar Energy Materials and Solar Cells, 2016. **158**: p. 189-194.

116. O'Mahony, F.T.F., et al., *Improved environmental stability of organic lead trihalide perovskite-based photoactive-layers in the presence of mesoporous TiO2.* Journal of Materials Chemistry A, 2015. **3**(14): p. 7219-7223.

117. Noh, J.H., et al., *Chemical management for colorful, efficient, and stable inorganic-organic hybrid nanostructured solar cells.* Nano Lett, 2013. **13**(4): p. 1764-9.

118. Shirayama, M., et al., *Degradation mechanism of CH3NH3PbI3 perovskite materials upon exposure to humid air.* Journal of Applied Physics, 2016. **119**(11).

119. Leguy, A.M.A., et al., *Reversible Hydration of CH3NH3PbI3 in Films, Single Crystals, and Solar Cells.* Chemistry of Materials, 2015. **27**(9): p. 3397-3407.

120. Christians, J.A., P.A. Miranda Herrera, and P.V. Kamat, *Transformation of the excited state and photovoltaic efficiency of CH3NH3PbI3 perovskite upon controlled exposure to humidified air*. J Am Chem Soc, 2015. **137**(4): p. 1530-8.

121. Poodt, P., et al., *Spatial atomic layer deposition: A route towards further industrialization of atomic layer deposition.* Journal of Vacuum Science & Technology A: Vacuum, Surfaces, and Films, 2012. **30**(1): p. 010802.

122. Dameron, A., et al. *Methods for Measuring Moisture Ingress*. in *Photovoltaic Module Reliability Workshop*. 2010. Denver, Colorado, USA.

123. ASTM Standard F1249, *Standard Test Method for Water Vapor Transmission Rate Through Plastic Film and Sheeting Using a Modulated Infrared Sensor*. ASTM International, West Conshohoken, PA.

124. MOCON Inc. *Instruments: Permeation and Barrier Measurement*. 2014; Available from: http://www.mocon.com/permeation.php.

125. ASTM Standard E96, *Standard Test Methods for Water Vapor Transmission of Materials*. ASTM International, West Conshohoken, PA.

126. Ranade, A., et al., *High sensitivity gas permeability measurement system for thin plastic films.* Review of Scientific Instruments, 2005. **76**(1): p. 013902.

127. Zhang, X.D., et al., *High sensitivity permeation measurement system for "ultrabarrier" thin films.* Journal of Vacuum Science & Technology A: Vacuum, Surfaces, and Films, 2007. **25**(6): p. 1587.

128. Dunkel, R., et al., *A new method for measuring ultra-low water-vapor permeation for OLED displays.* Journal of the Society for Information Display, 2005. **13**(7): p. 569-573.

129. Nisato, G., et al. *Evaluating High Performance Diffusion Barriers: The Calcium Test*. in *Proceedings Asia Display/IDW'01*. 2001.

130. Paetzold, R., et al., *Permeation rate measurements by electrical analysis of calcium corrosion.* Review of Scientific Instruments, 2003. **74**(12): p. 5147.

131. Kim, H., et al., *Experimental investigation of defect-assisted and intrinsic water vapor permeation through ultrabarrier films*. Rev Sci Instrum, 2016. **87**(3): p. 033902.

132. Schmidt-Mende, L. and J.L. MacManus-Driscoll, *ZnO – nanostructures, defects, and devices.* Materials Today, 2007. **10**(5): p. 40-48.

133. Mansfeld, F., *Electrochemical impedance spectroscopy (EIS) as a new tool for investigating methods of corrosion protection.* Electrochimica Acta, 1990. **35**(10): p. 1533-1544.

134. Esfahani, S.L., Z. Ranjbar, and S. Rastegar, *Comparison of corrosion protection of normal and galvanised steel coated by cathodic electrocoatings using EIS and salt spray tests.* Corrosion Engineering, Science and Technology, 2016. **51**(2): p. 82-89.

135. Mansfeld, F., et al., *Evaluation of corrosion protection by polymer coatings using electrochemical impedance spectroscopy and noise analysis.* Electrochimica Acta, 1998. **43**(19): p. 2933-2945.

136. Park, S.-M. and J.-S. Yoo, *Peer Reviewed: Electrochemical Impedance Spectroscopy for Better Electrochemical Measurements.* Analytical Chemistry, 2003. **75**(21): p. 455 A-461 A.

137. Ishizaki, T., Y. Masuda, and M. Sakamoto, *Corrosion resistance and durability of superhydrophobic surface formed on magnesium alloy coated with nanostructured cerium oxide film and fluoroalkylsilane molecules in corrosive NaCl aqueous solution.* Langmuir, 2011. **27**(8): p. 4780-8.

138. Mirhashemihaghighi, S., et al., *Electrochemical and Surface Analysis of the Corrosion Protection of Copper by Nanometer-Thick Alumina Coatings Prepared by Atomic Layer Deposition.* Journal of the Electrochemical Society, 2015. **162**(8): p. C377-C384.

139. Härkönen, E., et al., *Corrosion Protection of Steel with Oxide Nanolaminates Grown by Atomic Layer Deposition.* Journal of The Electrochemical Society, 2011. **158**(11): p. C369.

140. Perrotta, A., et al., *Analysis of Nanoporosity in Moisture Permeation Barrier Layers by Electrochemical Impedance Spectroscopy.* ACS Appl Mater Interfaces, 2015. **7**(29): p. 15968-77.

141. Tripp, M.K., et al., *The mechanical properties of atomic layer deposited alumina for use in micro- and nano-electromechanical systems.* Sensors and Actuators A: Physical, 2006. **130-131**: p. 419-429.

142. Cianci, E. and V. Foglietti, *Residual Stress in Silicon Nitride Thin Films Deposited by ECR-PECVD.* MRS Proceedings, 2011. **795**.

143. Iliescu, C., et al., *Residual stress in thin films PECVD depositions.* Journal of Optoelectronics and Advanced Materials, 2011. **13**(4): p. 387-394.

144. Shestaeva, S., et al., *Mechanical, structural, and optical properties of PEALD metallic oxides for optical applications.* Appl Opt, 2017. **56**(4): p. C47-C59.

145. Behrendt, A., et al., *Stress Management in Thin-Film Gas-Permeation Barriers.* ACS Appl Mater Interfaces, 2016. **8**(6): p. 4056-61.

146. Stoney, G.G., *The Tension of Metallic Films Deposited by Electrolysis.* Proceedings of the Royal Society of London. Series A, Containing Papers of a Mathematical and Physical Character, 1909. **82**(553): p. 172-175.

147. Bieder, A., et al., *Mechanical properties of carbon-modified silicon oxide barrier films deposited by plasma enhanced chemical vapor deposition on polymer substrates.* Thin Solid Films, 2007. **515**(13): p. 5430-5438.

148. Freund, L.B., J.A. Floro, and E. Chason, *Extensions of the Stoney formula for substrate curvature to configurations with thin substrates or large deformations.* Applied Physics Letters, 1999. **74**(14): p. 1987-1989.

149. da Silva Sobrinho, A.S., et al., *A study of defects in ultra-thin transparent coatings on polymers.* Surface and Coatings Technology, 1999. **116-119**: p. 1204-1210.

150. Favache, A., et al., *Fracture toughness measurement of ultra-thin hard films deposited on a polymer interlayer.* Thin Solid Films, 2014. **550**: p. 464-471.

151. Kim, K., S. Graham, and O.N. Pierron, *Note: A single specimen channel crack growth technique applied to brittle thin films on polymer substrates.* Rev Sci Instrum, 2017. **88**(3): p. 036102.

152. Nakamura, T. and S.M. Kamath, *Three-dimensional effects in thin film fracture mechanics.* Mechanics of Materials, 1992. **13**(1): p. 67-77.

153. Hutchinson, J.W. and Z. Suo, *Mixed Mode Cracking in Layered Materials*, in *Advances in Applied Mechanics*, J.W. Hutchinson and T.Y. Wu, Editors. 1991, Elsevier. p. 63-191.

154. Beuth, J.L., *Cracking of thin bonded films in residual tension.* International Journal of Solids and Structures, 1992. **29**(13): p. 1657-1675.

155. Vlassak, J.J., *Channel cracking in thin films on substrates of finite thickness.* International Journal of Fracture, 2003. **119**(4): p. 299-323.

156. Huang, R., et al., *Channel-cracking of thin films with the extended finite element method.* Engineering Fracture Mechanics, 2003. **70**(18): p. 2513-2526.

157. Anderson, T.L., *Fracture mechanics: fundamentals and applications*, ed. C. Press. 1995: Boca Raton.

158. Rice, J.R., *A Path Independent Integral and the Approximate Analysis of Strain Concentration by Notches and Cracks.* Journal of Applied Mechanics, 1968. **35**(2): p. 379-386.

159. Duan, Y., et al., *High-performance barrier using a dual-layer inorganic/organic hybrid thin-film encapsulation for organic light-emitting diodes.* Organic Electronics, 2014. **15**(9): p. 1936-1941.

160. Kempe, M., *Modeling of rates of moisture ingress into photovoltaic modules.* Solar Energy Materials and Solar Cells, 2006. **90**(16): p. 2720-2738.

161. Yang, L.-J., T.-J. Yao, and Y.-C. Tai, *The marching velocity of the capillary meniscus in a microchannel.* Journal of Micromechanics and Microengineering, 2004. **14**(2): p. 220-225.

162. Graff, G.L., R.E. Williford, and P.E. Burrows, *Mechanisms of vapor permeation through multilayer barrier films: Lag time versus equilibrium permeation.* Journal of Applied Physics, 2004. **96**(4): p. 1840.

163. Kempe, M., et al. *Evaluation and modeling of edge-seal materials for photovoltaic applications*. in *Photovoltaic Specialists Conference (PVSC), 2010 35th IEEE*. 2010. IEEE.

164. Pallas, N.R. and Y. Harrison, *An automated drop shape apparatus and the surface tension of pure water.* Colloids and Surfaces, 1990. **43**(2): p. 169-194.

165. Guziewicz, E., et al., *Extremely low temperature growth of ZnO by atomic layer deposition.* Journal of Applied Physics, 2008. **103**(3).

166. Zhou, J., N.S. Xu, and Z.L. Wang, *Dissolving Behavior and Stability of ZnO Wires in Biofluids: A Study on Biodegradability and Biocompatibility of ZnO Nanostructures.* Advanced Materials, 2006. **18**(18): p. 2432-2435.

167. Ahn, N., et al., *Highly Reproducible Perovskite Solar Cells with Average Efficiency of 18.3% and Best Efficiency of 19.7% Fabricated via Lewis Base Adduct of Lead(II) Iodide.* J Am Chem Soc, 2015. **137**(27): p. 8696-9.

168. Christians, J.A., et al., *Tailored interfaces of unencapsulated perovskite solar cells for >1,000 hour operational stability.* Nature Energy, 2018. **3**(1): p. 68-74.